DISSERTATION

THE ROLE OF INNER-CORE AND BOUNDARY LAYER DYNAMICS ON TROPICAL CYCLONE STRUCTURE AND INTENSIFICATION

Submitted by

Christopher J. Slocum

Department of Atmospheric Science

In partial fulfillment of the requirements

For the Degree of Doctor of Philosophy

Colorado State University

Fort Collins, Colorado

Spring 2018

Doctoral Committee:

Advisor: Wayne H. Schubert
Co-Advisor: Mark DeMaria

Russ S. Schumacher
David A. Randall
Michael Kirby
Michael Fiorino

ABSTRACT

THE ROLE OF INNER-CORE AND BOUNDARY LAYER DYNAMICS ON TROPICAL CYCLONE STRUCTURE AND INTENSIFICATION

Inner-core and boundary layer dynamics play a vital role in the tropical cyclone life cycle. This study makes use of analytical solutions and numerical models to gain insight into the role of dynamical processes involved with the incipient, rapidly intensifying, and eyewall replacement stages. A simplified, axisymmetric, one-layer, analytical model of tropical cyclone intensification is developed. Rather than formulating the model with the gradient balance approximation, the model uses the wave–vortex approximation, an assumption to the kinetic energy of the system, which limits its use to flows with small Froude numbers. Through filtering the inertia-gravity waves and adding a mass sink so that potential vorticity is not conserved in the system, the model is solved and provides analytical, time-evolving solutions that provide insight into long incubation periods prior to rapid intensification, potential vorticity tower development without frictional effects, and storm evolution in time through the maximum tangential velocity, total energy phase space. To understand the applicability of the forced, balance model for tropical cyclone intensification, the model is compared to a model using gradient balance. The comparison shows that the model based on the wave–vortex approximation is appropriate for fluids with flow speeds indicative of the external vertical normal mode in which case the deviation to the fluid depth is small.

To understand another aspect of the inner-core dynamics that influence the radial location of the mass sink associated with the eyewall convection in the tropical cyclone, boundary-layer dynamics are considered. Motivated by abrupt jumps in the horizontal wind fields observed in flight-level aircraft reconnaissance data collected in Hurricanes Allen (1980) and Hugo (1989), an axisymmetric, f-plane slab boundary layer numerical model with a prescribed pressure forcing is developed. From this model, two simple analytic models are formulated in addition to two local, steady-state models. These models allow for the role of shock dynamics in the tropical cyclone boundary layer to be assessed. Two local models are also developed to evaluate the role of the nonlinear terms in the full numerical slab model. The local models adequately describe the boundary layer winds outside of the eyewall region. If a storm is weak or broad, the local models can explain a portion of the structure that develops in the eyewall region. This result shows that, to capture the hyperbolic nature of the eyewall region, the nonlinear terms are needed. The nonlinear response allows for the boundary-layer Ekman pumping

to shift radially inward into the region of high inertial stability. The results from the local models and full numerical model also show that as the vortex wind field broadens, the convergence associated with the primary eyewall decays and that a secondary maximum displaced radially outward forms, a feature indicative of the formation of a secondary eyewall.

ACKNOWLEDGMENTS

I would like to convey my appreciation and gratitude to my advisors, Drs. Wayne H. Schubert and Mark DeMaria. Through their guidance, mentorship, and inspiration, this work has been possible. I would also like to extend my thanks to my committee members Drs. Russ S. Schumacher, David A. Randall, Michael J. Kirby, and Michael Fiorino for their comments and suggestions regarding this work.

I would also like to thank Alex Gonzalex, John Knaff, Kate Musgrave, Rick Taft, Paul Ciesielski, and Jon Martinez for answering questions, providing data, and supporting me during this research.

This research has been supported by the Hurricane Forecast Improvement Project (HFIP) through the Department of Commerce National Oceanic and Atmospheric Administration and the National Science Foundation under Grants AGS-1546610 and AGS-1601623. Workstation computing resources were provided through a gift from the Hewlett-Packard Corporation.

DEDICATION

This work is dedicated to
my mother, father, aunt, and friends.
Without their continued love and support,
none of this work would have been possible.

TABLE OF CONTENTS

LIST OF TABLES

LIST OF FIGURES

CHAPTER 1

INTRODUCTION

Inner-core and boundary-layer dynamics shape the incubation, deepening, and mature stages of the tropical cyclone. The three-layer, axisymmetric numerical model developed by Ooyama (1969a) is the first study to simulate these vortex life cycle stages. Initially, a three-layer model may seem overly simplistic or even inadequate to capture the vital processes at work in a tropical cyclone. However, this is not the case. The numerical simulations point to two critical processes within the storm: the time evolution of the dynamical response to diabatic heating in the eyewall and the Ekman pumping that results from the frictional convergence that develops in the boundary layer in response to the vortex in the overlying fluid. Despite this model resolving these features, we are still working towards developing an understanding of the mechanisms behind each process and the interplay between the boundary layer and the overlying, free atmosphere.

The Eliassen (1951) balanced vortex model offers insight into the balanced response of the vortex to diabatic heating. The studies of Shapiro and Willoughby (1982), Schubert and Hack (1982), and the many related derivatives offer insight into the mechanisms involved in intensity change and rapid intensification. Vigh and Schubert (2009) and Musgrave et al. (2012) present a series of experiments that illustrate the sensitivity of the tangential wind response due to the placement of the diabatic heating in relation to the inner-core, high inertial stability region. The location is key to understanding whether a vortex will rapidly increase the maximum tangential velocity or will expand the wind field and increase the kinetic energy. Unfortunately, time-dependent, analytic solutions to the Eliassen (1951) balanced vortex model have not been found and the location of the diabatic heating must be prescribed in order to solve for each balanced state. Naturally, we ask what processes are involved in determining the location of the diabatic heating.

To understand the radial distribution of the diabatic heating, work as early as Haurwitz (1935, 1936) points to the boundary layer for an explanation. However, the complexity and nonlinear nature of the tropical cyclone boundary layer complicate the progress towards developing a complete conceptual explanation regardless of the myriad of literature on the topic. Returning to the simulations in Ooyama (1969a), we see a simplification to the boundary layer equations in which gradient balance is assumed

for the azimuthal momentum equation and the nonlinear term is zero in the radial momentum equation. Ooyama (1969b) relaxed these assumptions resulting in the Ekman pumping shifting radially inward. Several studies have shown that the location of the Ekman pumping determines the location of the eyewall convection (e.g., Ooyama 1982; Kepert and Nolan 2014; Frisius and Lee 2016). In addition to the location of the Ekman pumping, flight-level observations show abrupt jumps in the horizontal velocity fields, indicating that shock dynamics may play a role in the eyewall region of tropical cyclones (Williams et al. 2013; Slocum et al. 2014; Schubert et al. 2017). This means that understanding the location of this pumping and abrupt jumps in the horizontal velocity fields can help determine trends in the intensity of the tropical cyclone. Intensity is also influenced by eyewall replacement cycles. During eyewall replacement, the storm intensification often pauses or the storm weakens as a secondary eyewall develops and eventually supersedes the original primary eyewall as the inner eyewall decays. Recent work suggests that the boundary layer is critical to this process in that as a secondary maximum in the radial inflow develops, the inflow and Ekman pumping that are coupled to the primary eyewall are shut off. Aspects of the boundary layer mechanism involved in eyewall replacement are still being discussed through observational, theoretical, and modeling work (e.g., Sitkowski et al. 2011; Rozoff et al. 2012; Kepert 2013; Abarca and Montgomery 2013; Kepert and Nolan 2014; Slocum et al. 2014).

With the goal of contributing to a more complete conceptual model of the life cycle of the tropical cyclone, this work seeks to address some of the gaps in our current understanding. In chapter 2, we explore the utility of a forced, balanced model for tropical cyclone intensification that is based on a balance relation that arises from an approximation to the system's kinetic energy. In this work, we develop time-evolving, analytic solutions that provide insight into tropical cyclone incubation, hollow potential vorticity structures, and energetics within the forced, balanced model. In chapter 3, we return to the boundary layer to understand the development of the Ekman pumping associated with the frictionally induced convergence. First, we develop a series of "metaphor" or "toy" models that contain a portion of the entire system's dynamics to understand the formation of triangular waves and N-waves in the context of primary and secondary eyewalls. Then, we develop two local, steady-state models that we use in conjunction with an axisymmetric slab boundary layer model to understand shock formation in tropical cyclones. Lastly, we present concluding remarks and discuss the connections between the boundary layer and vortex in the overlying fluid.

CHAPTER 2

A FORCED, BALANCED MODEL OF TROPICAL CYCLONE INTENSIFICATION[1]

Tropical cyclone intensity and intensification rate garner interest from both the research and operational community. The problem is often framed as how strong could the tropical cyclone become (e.g., potential intensity) and how does the storm realize that strength (e.g., intensification and rapid intensification) based on the environmental conditions around the storm. Essentially, potential intensity represents what the "mature" stage (e.g., quasi-steady state) of the "life cycle" could be based on given a set of boundary layer characteristics and air–sea interaction parameterizations (e.g., Kleinschmidt 1951; Miller 1958; Emanuel 1986; DeMaria and Kaplan 1994; Holland 1997). While a captivating research problem, potential intensity is not the focus of chapter 2. Instead, we explore some aspects of the inner-core dynamics that result in intensification and rapid intensification of the vortex. In addition to potential intensity via sea surface temperature and ocean heat content ideas playing a role in intensification, other environmental conditions such as shear (e.g., Jones 1995; DeMaria 1996; Frank and Ritchie 2001) and tropospheric moisture (e.g., Gray 1968; DeMaria et al. 2005; Hill and Lackmann 2009) do impact the intensification rate. Ignoring factors leading to unfavorable environmental influences, the inner-core dynamics dominate, causing the storm to intensify. The classic inner-core dynamics understanding for intensification is the tangential wind response to forcing, such as diabatic heating (Eliassen 1951).

The Eliassen (1951) balanced vortex equations are a filtered model for an evolving, axisymmetric vortex in both hydrostatic and gradient balance. The model as well as the transverse circulation and geopotential tendency equations that can be derived from it, provide insights into eyewall tilt (e.g., Emanuel 1997; Schubert and McNoldy 2010), and eye features, such as hub clouds, clear air moats, and warm-ring thermal structures (e.g., Schubert et al. 2007; Sitkowski et al. 2012; Stern and Nolan 2012; Stern and Zhang 2013), and intensification. Shapiro and Willoughby (1982), Schubert and Hack (1982), and others use the Eliassen (1951) balanced vortex model to provide an understanding of the role of diabatic heating and inertial stability in tropical cyclone intensification. In a series of experiments in which the radial location of an area-averaged region of diabatic heating is changed, Vigh and Schubert (2009) and Musgrave et al. (2012) show that the sensitivity of the tangential wind tendency results in either rapid intensification or expansion of the vortex wind field. When the diabatic heating

[1]This chapter contains model derivation and motivating results included in Schubert et al. (2016).

is within the region of high inertial stability, the tangential wind tendency is large. However, if the heating is outside of the radius of maximum wind in the region with lower inertial stability, the tangential wind tendency is small and only contributes to the integrated kinetic energy of the vortex. In addition to the theoretical work extending the Eliassen (1951) balanced vortex model, the inertial stability framework is applied to airborne Doppler radar updraft observations to provide context for intensifying and quasi-steady state systems (Rogers et al. 2013, 2015). These inertial stability ideas represent one of the intensification mechanisms contained within the literature. The other main mechanisms can be loosely classified as boundary layer control (e.g., Ooyama 1969a; Smith and Vogl 2008; Kepert 2010a; Williams et al. 2013) and "vorticity dynamics" (for a broader view, see the review articles by Montgomery and Smith 2014, 2017).

While our understanding of inner-core tropical cyclone dynamics has been advanced through the insights offered by work based on the Eliassen (1951) balanced vortex model, analytic solutions for the time evolution of a balanced vortex have not been found. The purpose of this chapter is to present analytic, time-dependent solutions of an axisymmetric, one-layer, balanced vortex model using the wave–vortex approximation recently introduced by Salmon (2014). Through evaluating the results from the model outlined in the next few sections, our goal is to provide insight into the long "incubation" period, a term introduced by Ooyama (1969a) based on results from his three-layer model in which the simulations took a long period of time before undergoing rapid intensification as shown in Fig. 2.1. Yamasaki (1983) ran a series of simulations using an axisymmetric, nonhydrostatic, cloud permitting model to simulate the early stages of the "life cycle" of the tropical cyclone (i.e., incipient and deepening). Figure 2.2 shows results from his numerical simulation in which the vortex remains relatively weak before intensifying and contracting. Figure 2.3 offers insight into this process in terms of rainfall rate and distribution. As the mass sink or the diabatic heating is concentrated in the eyewall region during contraction, the vortex responds by deepening (i.e., spinning up, rapid intensification). As will be shown, the radial distribution of the mass sink is critical to this process. In addition to the long incubation period, we will examine how the size of the vortex evolves through time by analyzing the change in total energy in the forced, balanced model.

Section 2.1 presents a review of the shallow water primitive equations for an axisymmetric vortex on an f plane. In section 2.2, the wave–vortex approximation, an approximation made to the kinetic energy, is introduced. Section 2.3 adds two additional approximations resulting in a forced, balanced vortex model. Analytic solutions for two- (section 2.3) and three-region (section 2.4) idealizations are

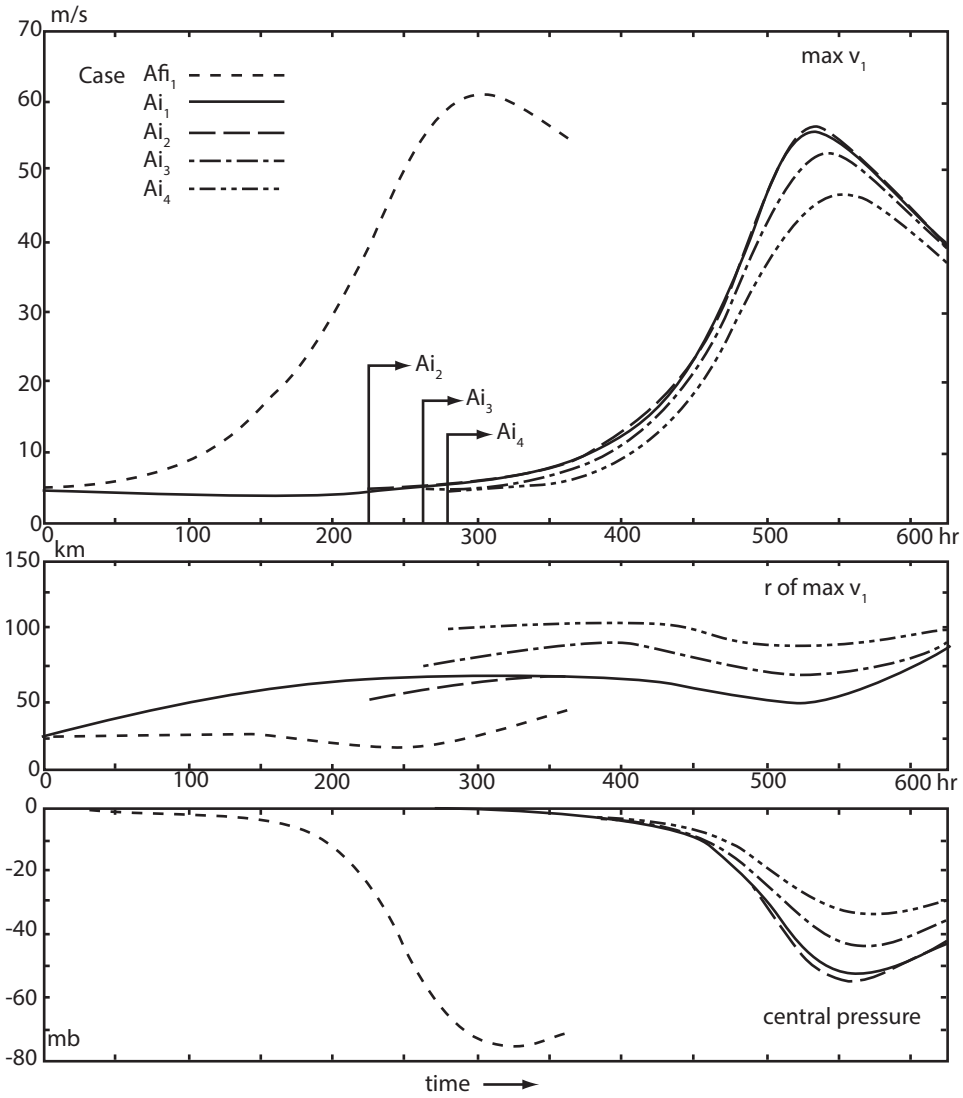

FIG. 2.1. Tangential velocity (top), radius of maximum tangential velocity (middle), and central pressure (bottom) from a series of simulations by Ooyama (1969a) using an axisymmetric, three-layer model. The simulations start with initially weak vortices (5 m s^{-1}) that have radii of maximum tangential velocity of 25, 50, 75, and 100 km for cases Ai_1, Ai_2, Ai_3, and Ai_4 respectively. The time origin of the integration in the last three cases is shifted to ease comparison and Afi_1 is the same as Ai_1, except that the eddy viscosity has a smaller value. Reproduced from Fig. 17 of Ooyama (1969a).

presented to explore the "incubation" time of a vortex and the formation of hollow potential vorticity structures. Section 2.5 generalizes the analytic solutions to a multi-region model in R space with which the energetics of the forced, balanced model are examined. Section 2.6 uses an iterative procedure in r space to compare a multi-region model of the Eliassen (1951) balanced vortex model (balanced vortex 1) to the multi-region model with the balance relation arising from the wave–vortex approximation (balanced vortex 2) to understand the limits of the theory. Concluding remarks on the forced, balanced

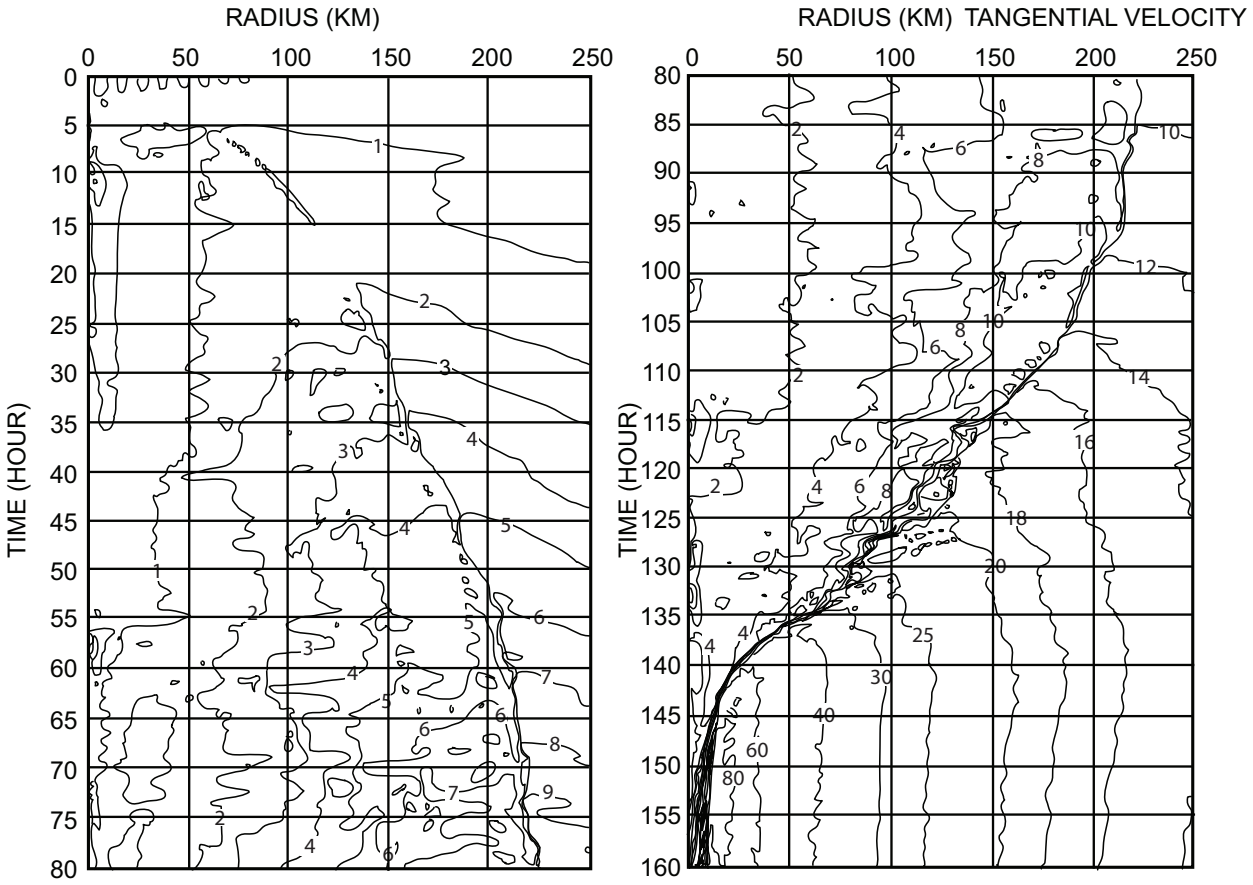

FIG. 2.2. Time–radius Hovmöller diagram of the tangential velocity (m s^{-1}) at $z = 0.9$ km for a numerical experiment by Yamasaki (1983) using the axisymmetric, nonhydrostatic, cloud permitting model (Yamasaki 1977) run at 500 m resolution. After roughly a 24-h period of contraction, hurricane force winds (> 33 m s^{-1}) develop around hour 134. This point marks the start of vortex rapid intensification before the vortex reaches a quasi-steady state with $v_{\max} \sim 80$ m s^{-1}. Reproduced from Fig. 2 of Yamasaki (1983).

model developed using the wave–vortex approximation and the work presented here are given in section 2.7.

2.1 SHALLOW WATER PRIMITIVE EQUATIONS

The axisymmetric shallow water primitive equations on an f plane are

$$\frac{\partial u}{\partial t} - (f+\zeta)v + \frac{\partial}{\partial r}\left[gh + \tfrac{1}{2}(u^2+v^2)\right] = 0, \tag{2.1}$$

$$\frac{\partial v}{\partial t} + (f+\zeta)u = 0, \tag{2.2}$$

$$\frac{\partial h}{\partial t} + \frac{\partial (ruh)}{r\partial r} = 0, \tag{2.3}$$

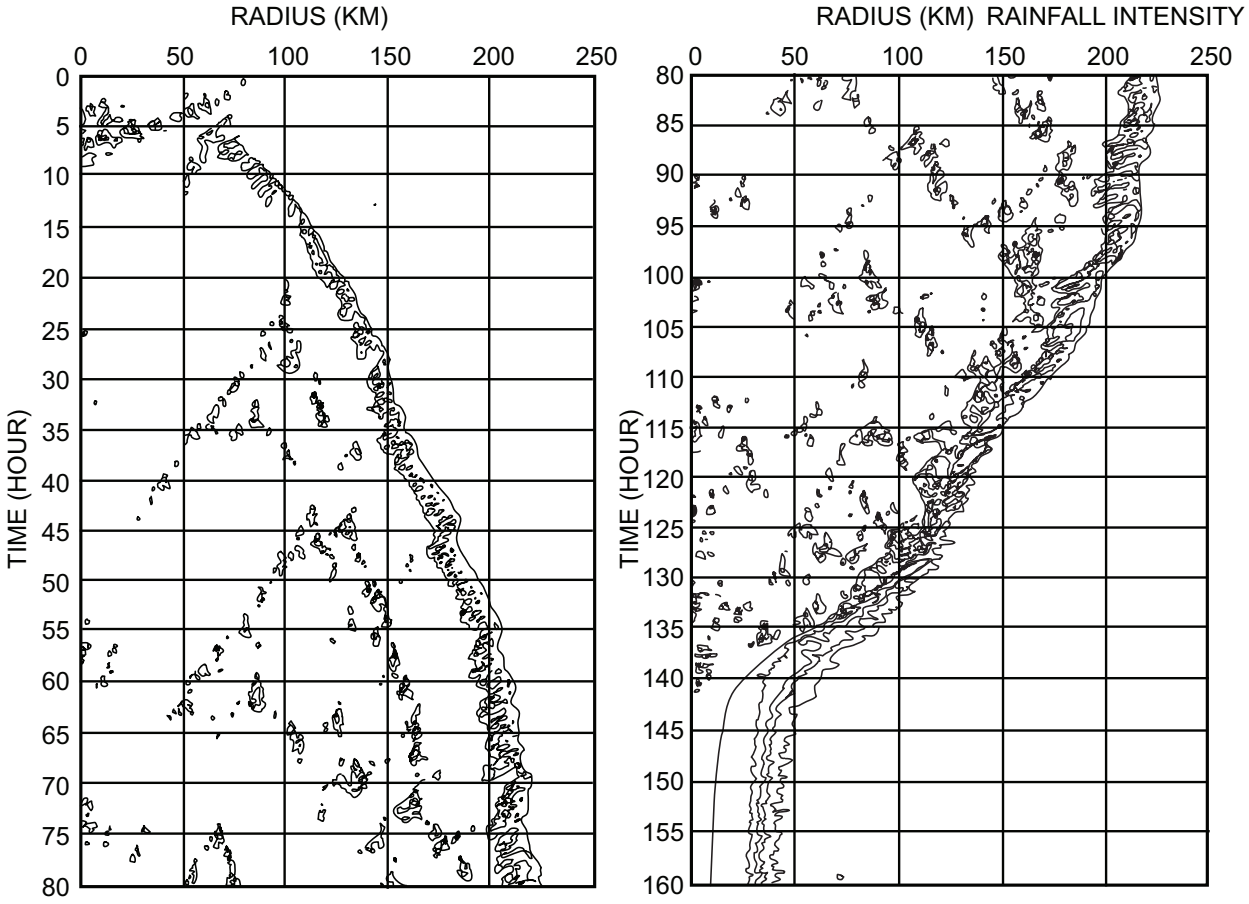

FIG. 2.3. Time–radius Hovmöller diagram of rainfall rates (isolines of 1, 5, 10, and 20 mm (10 min)$^{-1}$) for a numerical experiment by Yamasaki (1983) using an axisymmetric, nonhydrostatic, cloud permitting model (Yamasaki 1977) run at 500 m resolution. By hour 140, the eyewall has developed in response to the contraction and intensification seen in the tangential velocity in Fig. 2.2. Reproduced from Fig. 1 of Yamasaki (1983).

where u is the radial wind, v is the tangential wind, h is the fluid depth, g is the acceleration due to gravity, f is the constant Coriolis parameter, and $\zeta = \partial(rv)/r\partial r$ is the relative vorticity. The absolute angular momentum principle, obtained from (2.2), is

$$\frac{D}{Dt}\left(rv + \tfrac{1}{2}fr^2\right) = 0, \tag{2.4}$$

where

$$\frac{D}{Dt} = \frac{\partial}{\partial t} + u\frac{\partial}{\partial r} \tag{2.5}$$

is the material derivative. The vorticity equation, also obtained from (2.2), can be written in the form

$$\frac{D(f+\zeta)}{Dt} + (f+\zeta)\frac{\partial(ru)}{r\partial r} = 0, \tag{2.6}$$

while the continuity equation (2.3) can be written in the form

$$\frac{Dh}{Dt} + h\frac{\partial(ru)}{r\partial r} = 0. \tag{2.7}$$

Eliminating the divergence between (2.6) with (2.7), we obtain the potential vorticity conservation principle

$$\frac{DP}{Dt} = 0, \tag{2.8}$$

where

$$P = \frac{\bar{h}}{h}\left(f + \frac{\partial(rv)}{r\partial r}\right) \tag{2.9}$$

is the potential vorticity, with the constant $\bar{h}$ denoting the fluid depth to which $h(r,t)$ asymptotes as $r \to \infty$.

2.2 The wave–vortex approximation

Taking cues from Maxwell's equations in classical electrodynamics, Salmon (2014) proposed a wave–vortex approximation of (2.1)–(2.3). In the 2014 work, he derived this approximation by first expressing the exact shallow water dynamics in the equivalent Hamiltonian form (i.e., classical mechanics), which, as discussed in the appendix, involves the Poisson bracket and the exact Hamiltonian (total energy). In the expression for the exact Hamiltonian, the kinetic energy in the fluid column is given by $\frac{1}{2}(u^2+v^2)h$. In the context of the equivalent Hamiltonian form, the only approximation in the wave–vortex model is to replace the exact Hamiltonian with an approximate Hamiltonian in which the kinetic energy in the fluid column is approximated by $\frac{1}{2}(u^2+v^2)\bar{h}$ (i.e., it is assumed that the deviations in the depth of the fluid h are small in comparison to $\bar{h}$). Then, for the axisymmetric, shallow water dynamics considered here, the wave–vortex approximation takes the form

$$\frac{\partial u}{\partial t} - Pv + g\frac{\partial h}{\partial r} = 0, \tag{2.10}$$

$$\frac{\partial v}{\partial t} + Pu = 0, \tag{2.11}$$

$$\frac{\partial h}{\partial t} + \bar{h}\frac{\partial(ru)}{r\partial r} = 0, \tag{2.12}$$

where P is defined by (2.9). A detailed derivation of (2.10)–(2.12) using Hamiltonian fluid mechanics is given in the appendix.

Whenever we replace one set of equations, such as (2.1)–(2.3), with another approximate set, such as (2.10)–(2.12), there arises the question of identifying variables in the approximate set with variables

in the original set. If we identify the variables u, v, h in the approximate dynamics (2.10)–(2.12) with the variables u, v, h in the parent dynamics (2.1)–(2.3), we conclude that all three equations (2.1)–(2.3) have been approximated. However, this is not the only interpretation, as noted by Salmon (2014) and Schubert et al. (2016). The identity of variables in the approximate dynamics with variables in the parent dynamics (2.1)–(2.3) is "unavoidably ambiguous" and represents an "identification error." For example, suppose we write (2.10)–(2.12) in terms of the variable $\hat{u} = (\bar{h}/h)u$ and make the simple notational change $\hat{u} \to u$, so that (2.10)–(2.12) become

$$\frac{\partial}{\partial t}\left(\frac{h}{\bar{h}}u\right) - Pv + g\frac{\partial h}{\partial r} = 0, \tag{2.13}$$

$$\frac{\partial v}{\partial t} + (f+\zeta)u = 0, \tag{2.14}$$

$$\frac{\partial h}{\partial t} + \frac{\partial (r\,u\,h)}{r\,\partial r} = 0. \tag{2.15}$$

Now, if we identify the variables u, v, h in (2.13)–(2.15) with the variables u, v, h in the parent dynamics (2.1)–(2.3), we conclude that (2.14) and (2.15) are exact, but (2.13) is an approximated form of (2.1). Equations (2.10)–(2.12) and (2.13)–(2.15) are equally valid forms of the wave–vortex approximation with somewhat different interpretations attached to the associated u fields. In the next section, we shall proceed from equations (2.13)–(2.15) because of the similarity to (2.1)–(2.3), but the analysis could equally well proceed from (2.10)–(2.12).

Because the notational change $\hat{u} \to u$ has made (2.14) and (2.15) formally identical to (2.2) and (2.3), the absolute angular momentum and potential vorticity equations derived from (2.14) and (2.15) are formally identical to (2.4) and (2.8), with the material derivative given by (2.5). Alternatively, if we proceed from (2.10)–(2.12), we find that the absolute angular momentum and potential vorticity equations are also given by (2.4) and (2.8) with a slightly modified definition of D/Dt, i.e., with a definition in which the radial advecting velocity is given by $(\bar{h}/h)u$. As we shall see in section 2.3, the absolute angular momentum and potential vorticity equations play a crucial role in the analysis.

It is also interesting to note that the linear geostrophic adjustment dynamics of (2.10)–(2.12) or (2.13)–(2.15) are identical to those of (2.1)–(2.3). This can be seen by simply linearizing each set about a resting basic state with constant depth $\bar{h}$ and then noting that the linearized equations from each set are identical. A discussion of these linearized dynamics can be found in Schubert et al. (1980). Concerning the nonlinear transient adjustment dynamics of (2.10)–(2.12) or (2.13)–(2.15), they do differ from those described by (2.1)–(2.3). As can be inferred from the results of Kuo and Polvani (1997), the

nonlinear transient adjustment dynamics of (2.1)–(2.3) involve the formation and decay of shocks, a fluid dynamics phenomena arising from Burgers' equation (Bateman 1915; Burgers 1948; Whitham 1974). As noted by Salmon (2014), the approximate wave–vortex dynamics do not allow inertia–gravity waves to steepen and form shocks. This is consistent with the notion that the approximate wave–vortex dynamics is limited to flows with a small Froude number, i.e., to flows in which typical flow speeds are much less than $c = (g\bar{h})^{1/2}$.

2.3 Forced, balanced model

We now make two changes to the wave–vortex system (2.13)–(2.15). The first change is to include a mass sink term on the right-hand side of (2.15). The second change is to introduce an approximation that filters inertia–gravity waves by neglecting the local time derivative term in (2.13). Thus, our forced, balanced model takes the form

$$P v = g \frac{\partial h}{\partial r}, \tag{2.16}$$

$$\frac{\partial v}{\partial t} + (f + \zeta) u = 0, \tag{2.17}$$

$$\frac{\partial h}{\partial t} - + \frac{\partial (r u h)}{r \partial r} = -hS. \tag{2.18}$$

Because of the addition of a mass sink term in the continuity equation (2.18), the potential vorticity equation now becomes

$$\frac{DP}{Dt} = SP \tag{2.19}$$

and the total energy principle becomes

$$\mathcal{G} = \frac{d}{dt} \int_0^\infty \tfrac{1}{2} \left[v^2 \bar{h} + g(h - \bar{h})^2 \right] r \, dr = \int_0^\infty g(\bar{h} - h) h S \, r \, dr. \tag{2.20}$$

In the remainder of this chapter, we will present analytical solutions of the forced, balanced model (2.16)–(2.18). Because of the approximation made to the kinetic energy, it should be noted that the balanced vortex model (2.16)–(2.18) is different than the balanced vortex model of Eliassen (1951), since the latter is based on gradient wind balance rather than the balance relation (2.16). The Eliassen (1951) balanced vortex model has been used in many tropical cyclone studies, such as those of Ooyama (1969a), Shapiro and Willoughby (1982), and Schubert and Hack (1982), and should be regarded as the more general of the two models because it does not have a small Froude number restriction on its

applicability. However, an advantage of the system (2.16)–(2.18) is the ease with which analytic, time-dependent solutions can be obtained. A comparison of the two models using numerical methods to find solutions in r-space will be presented towards the end of this chapter.

To evaluate solutions of (2.16)–(2.18), we use the mass sink $S(r,t)$ to simulate the effect of diabatic heating in a continuously stratified, compressible fluid. This use of a mass sink has been discussed by Ooyama (1969a) in the context of an axisymmetric tropical cyclone model having three incompressible fluid layers and by DeMaria and Pickle (1988) in the context of an axisymmetric tropical cyclone model having three isentropic fluid layers. The use of S as a proxy for diabatic heating has also been discussed in the context of a one-layer model by Bouchut et al. (2009) and a two-layer model by Lambaerts et al. (2011). Fulton and Schubert (1985) provide another interpretation of S in terms of tropical diabatic heating by performing a vertical normal mode analysis of observed vertical profiles of tropical diabatic heating. Typical vertical profiles of diabatic heating project onto the external mode ($c \approx 250$–300 m s^{-1}) and the first two internal modes ($c \approx 50$–77 m s^{-1} and 29–47 m s^{-1}), with the exact values of c depending on the boundary conditions and static stability used in the eigenvalue calculation. Since the wave–vortex approximation has a small Froude number restriction, we have experimented with values of c between 250 and 300 m s^{-1}, with the conclusion that the results changed little as c is varied in this range. When we compare the balance relation based on wave–vortex dynamics to the gradient balance dynamics in section 2.6, we will explore the validity of assuming values of c consistent with the external mode. For the results shown here, we have used $c = 250$ m s^{-1}. As a useful guide to interpretation, the idealized analytical solutions presented here can be considered most applicable to the vertical mean structure (i.e., the external mode) of tropical cyclones.

Now, we assume that the mass sink $S(r,t)$ is a positive constant S_1 in the core region and vanishes in the region outside the core. The core region is bounded by an absolute angular momentum surface that moves inward with the inward radial flow. The position of this absolute angular momentum surface is denoted by $r_1(t)$. The function $r_1(t)$ is as yet undetermined but will later be determined as part of the solution of the potential vorticity prediction/inversion problem. With these assumptions, the mass sink $S(r,t)$ can be written in the form

$$S(r,t) = S_1 H[r_1(t) - r] = \begin{cases} S_1 & \text{if } r < r_1(t) \\ \frac{1}{2} S_1 & \text{if } r = r_1(t) \\ 0 & \text{if } r > r_1(t), \end{cases} \tag{2.21}$$

where $H[x]$ is the Heaviside step function (not to be confused with the Hamiltonian functional used in the appendix), defined as zero for $x<0$, as unity for $x>0$, and as $\frac{1}{2}$ for $x=0$. Because of the form of the mass sink (2.21), an initial piecewise uniform potential vorticity remains piecewise uniform. The piecewise uniform initial condition on P is

$$P(r,0)=P_1H[r_{10}-r]+fH[r-r_{10}]=\begin{cases}P_1 & \text{if } r<r_{10}\\ \frac{1}{2}(P_1+f) & \text{if } r=r_{10}\\ f & \text{if } r>r_{10},\end{cases} \tag{2.22}$$

where the constant P_1 is the initial potential vorticity in the core and the constant r_{10} is the initial value of $r_1(t)$.

Given the forcing (2.21) and the initial condition (2.22), we now seek a solution of the potential vorticity equation (2.19) having the piecewise constant form

$$P(r,t)=\alpha_1(t)H[r_1(t)-r]+\alpha_2(t)H[r-r_1(t)]\begin{cases}\alpha_1(t) & \text{if } r<r_1(t)\\ \frac{1}{2}[\alpha_1(t)+\alpha_2(t)] & \text{if } r=r_1(t)\\ \alpha_2(t) & \text{if } r>r_1(t),\end{cases} \tag{2.23}$$

where $\alpha_1(t)$ and $\alpha_2(t)$ are as yet undetermined functions of time. Substituting (2.23) into (2.19), we obtain

$$\begin{aligned}0&=\frac{\partial P}{\partial t}+u\frac{\partial P}{\partial r}-SP\\ &=\left(\frac{d\alpha_1}{dt}-S_1\alpha_1H[r_1(t)-r]\right)H[r_1(t)-r]+\alpha_1\left(\frac{dr_1}{dt}-u\right)\delta[r_1(t)-r]\\ &\quad+\left(\frac{d\alpha_2}{dt}-S_1\alpha_2H[r_1(t)-r]\right)H[r-r_1(t)]-\alpha_2\left(\frac{dr_1}{dt}-u\right)\delta[r-r_1(t)]\\ &=\left(\frac{d\alpha_1}{dt}-S_1\alpha_1\right)H[r_1(t)-r]+\frac{d\alpha_2}{dt}H[r-r_1(t)]\\ &=\begin{cases}\dfrac{d\alpha_1}{dt}-S_1\alpha_1 & \text{if } r<r_1(t)\\ +\dfrac{d\alpha_2}{dt} & \text{if } r>r_1(t)\end{cases}\end{aligned} \tag{2.24}$$

for $r\neq r_1(t)$, where $\delta(x)=dH[x]/dx$ is the Dirac delta function. We are able to obtain (2.24) by using the fact that $dr_1/dt=u(r_1,t)$ and $H[r_1(t)-r]H[r-r_1(t)]=0$ for $r\neq r_1(t)$. When $r<r_1(t)$, the step functions take on the values $H[r_1(t)-r]=1$ and $H[r-r_1(t)]=0$. The result is the first line of the case

statement at the end of (2.24). When $r > r_1(t)$, the step functions take on the values $H[r_1(t)-r]=0$ and $H[r-r_1(t)]=1$. The result is the last line of the case statement at the end of (2.24). Using the initial uniform condition on P shown in (2.22), the solutions for the coefficients α_1 and α_2 are

$$\alpha_1(t)=fe^{\tau_1} \quad \text{and} \quad \alpha_2(t)=f, \tag{2.25}$$

where $\tau_1 = S_1(t+t_1)$ is a dimensionless time and the constant t_1 is defined by $e^{S_1 t_1} = P_1/f$, i.e., t_1 is the time that would be required for the vortex to exponentially spin up from a state of rest. Through using (2.25), the solution (2.23) becomes

$$P(r,t)=fe^{\tau_1}H[r_1(t)-r]+fH[r-r_1(t)]=\begin{cases} e^{\tau_1} & \text{if } r<r_1(t) \\ \dfrac{1}{2}(e^{\tau_1}+1) & \text{if } r=r_1(t) \\ 1 & \text{if } r>r_1(t). \end{cases} \tag{2.26}$$

To diagnose the wind and mass fields from the potential vorticity field (2.26), we require the solution of the invertibility principle. The invertibility principle for h can be derived from the combination of P with the balance condition (2.16), which gives us

$$\frac{1}{r}\frac{\partial}{\partial r}\left(\frac{r}{P}\frac{\partial h}{\partial r}\right)-\frac{P}{g\bar{h}}=-\frac{f}{g}. \tag{2.27}$$

With (2.26), (2.27) becomes

$$\begin{cases} \dfrac{\partial^2 h}{\partial r^2}+\dfrac{1}{r}\dfrac{\partial h}{\partial r}-\mu_1^2 h=-\mu_1^2\bar{h}e^{-\tau_1} & \text{if } r<r_1(t) \\ \dfrac{\partial^2 h}{\partial r^2}+\dfrac{1}{r}\dfrac{\partial h}{\partial r}-\mu_1^2 h=-\mu_1^2\bar{h} & \text{if } r>r_1(t), \end{cases} \tag{2.28}$$

where

$$\mu_1(t)=\mu e^{\tau_1} \quad \text{and} \quad \mu=\frac{f}{c} \tag{2.29}$$

are the inverse Rossby lengths in the two regions. The value of the Rossby length $\mu^{-1}=(c/f)$ in the "far-field" region is fixed and the value in the core $(c/f)e^{-\tau_1}$ decreases exponentially with time. The result of the decrease in the Rossby length is to increase the dynamical eye size. As discussed by Schubert and McNoldy (2010), large dynamical eyes provide "room" for subsiding air and the formation of eye features such as moats, hub clouds, a warm-ring thermal structure, and upper-level cloud overhang (Schubert et al. 2007).

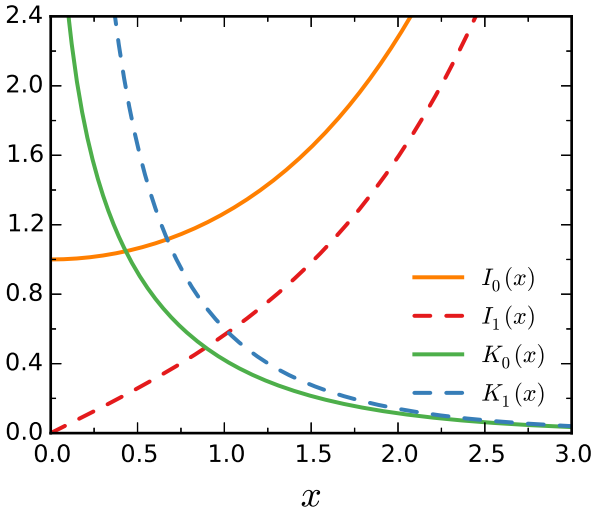

FIG. 2.4. The zero ($n=0$) and first ($n=1$) order modified Bessel functions of the first I_n and second K_n kind.

Following the approach outlined in Schubert and Hack (1982), we will express the solution of (2.28) in terms of the zero order modified Bessel function of the first kind $I_0(x)$ and second kind $K_0(x)$, which satisfy the following zero order modified Bessel equation, i.e.,

$$\frac{d^2 I_0(x)}{d\,x^2} + \frac{d\,I_0(x)}{x\,d\,x} - I_0(x) = 0, \tag{2.30}$$

$$\frac{d^2 K_0(x)}{d\,x^2} + \frac{d\,K_0(x)}{x\,d\,x} - K_0(x) = 0. \tag{2.31}$$

We will also make use of the derivative relations

$$\frac{d\,I_0(x)}{d\,x} = I_1(x), \tag{2.32}$$

$$\frac{d\,K_0(x)}{d\,x} = -K_1(x), \tag{2.33}$$

$$\frac{d[x\,I_1(x)]}{x\,d\,x} = I_0(x), \tag{2.34}$$

$$\frac{d[x\,K_1(x)]}{x\,d\,x} = -K_0(x), \tag{2.35}$$

and the Wronskian

$$I_0(x)\,K_1(x) + K_0(x) I_1(x) = \frac{1}{x}, \tag{2.36}$$

where $I_1(x)$ and $K_1(x)$ are the first order modified Bessel functions of the first and second kind respectively. For reference, the functions $I_0(x)$, $K_0(x)$, $I_1(x)$ and $K_1(x)$ are shown in Fig. 2.4.

Returning to the goal of solving the invertibility problem (2.28) for the entire domain, we first solve it in each of the subregions between the prescribed absolute angular momentum surfaces and enforce the boundary conditions for $r = 0$ and $r \to \infty$. After this step, we match the h and v at $r = r_1(t)$. For example, in the region $r < r_1(t)$, the solution for h consists of the sum of the particular solution $\bar{h}e^{-\tau_1}$ and the homogeneous solution proportional to $I_0(\mu_1 r)$, with the other homogeneous solution $K_0(\mu_1 r)$ discarded because it is unbounded at $r = 0$ as shown by Fig. 2.4. For the region $r > r_1(t)$, the solution for h consists of the sum of the particular solution $\bar{h}$ and the homogeneous solution proportional to $K_0(\mu_1 r)$, with the other homogeneous solution $I_0(\mu_1 r)$ discarded because it is unbounded as $r \to \infty$. The solution for the fluid depth in the two-region model can be written in the form

$$h(r,t) = \bar{h} \begin{cases} e^{-\tau_1} + \dfrac{v_1(t)}{c} \dfrac{I_0(e^{\tau_1}\mu r)}{I_1(e^{\tau_1}\mu r_1)} & \text{if } 0 \le r \le r_1(t) \\ 1 - \dfrac{v_1(t)}{c} \dfrac{K_0(\mu r)}{K_1(\mu r_1)} & \text{if } r_1(t) \le r < \infty, \end{cases} \tag{2.37}$$

where the function $v_1(t)$ is as yet undetermined. In (2.37) and the following two equations, the first line on the right-hand side, $0 \le r \le r_1(t)$, represents the "inner-core" region, while the second line, $r_1(t) \le r < \infty$, represents the "far-field" region. From the balance relation (2.16) and the modified Bessel function derived relations (2.32)–(2.33), the solution for the tangential wind is

$$v(r,t) = v_1(t) \begin{cases} \dfrac{I_1(e^{\tau_1}\mu r)}{I_1(e^{\tau_1}\mu r_1)} & \text{if } 0 \le r \le r_1(t) \\ \dfrac{K_1(\mu r)}{K_1(\mu r_1)} & \text{if } r_1(t) \le r < \infty. \end{cases} \tag{2.38}$$

From (2.38), we note that $v(r,t)$ is guaranteed to be continuous at $r = r_1(t)$, which validates the choice of coefficients for $I_0(\mu_1 r)$ and $K_0(\mu r)$ in (2.37). From (2.38) and the derivative relations (2.34)–(2.35), the relative vorticity for the two-region model is given by

$$\frac{\zeta(r,t)}{f} = \frac{v_1(t)}{c} \begin{cases} e^{\tau_1} \dfrac{I_0(e^{\tau_1}\mu r)}{I_1(e^{\tau_1}\mu r_1)} & \text{if } 0 \le r \le r_1(t) \\ -\dfrac{K_0(\mu r)}{K_1(\mu r_1)} & \text{if } r_1(t) \le r < \infty. \end{cases} \tag{2.39}$$

From (2.39), we note that both ζ and P are discontinuous at $r = r_1(t)$.

We still need to determine $v_1(t)$ and $r_1(t)$. From (2.37), the continuity of $h(r,t)$ at $r = r_1(t)$ requires that

$$\frac{v_1(t)}{c} = \frac{(1 - e^{-\tau_1})\, I_1(e^{\tau_1}\mu r_1) K_1(\mu r_1)}{I_0(e^{\tau_1}\mu r_1) K_1(\mu r_1) + K_0(\mu r_1) I_1(e^{\tau_1}\mu r_1)}. \tag{2.40}$$

Because of the absolute angular momentum principle (2.4), the edge of the mass sink $r_1(t)$ is related to the maximum tangential wind denoted as $v_1(t)$ for the two-region model by $r_1(t)v_1(t)+\frac{1}{2}f\,r_1^2(t)=\frac{1}{2}f\,R_1^2(t)$, where the constant R_1 is the potential radius of the absolute angular momentum surface. We rewrite the absolute angular momentum principle in the form

$$\frac{v_1(t)}{c}=\frac{(\mu R_1)^2-(\mu r_1)^2}{2\mu r_1}. \tag{2.41}$$

Now, we eliminate $v_1(t)/c$ between (2.40) and (2.41) to obtain

$$\frac{(1-e^{-\tau_1})\,I_1(e^{\tau_1}\mu r_1)K_1(\mu r_1)}{I_0(e^{\tau_1}\mu r_1)K_1(\mu r_1)+K_0(\mu r_1)I_1(e^{\tau_1}\mu r_1)}=\frac{(\mu R_1)^2-(\mu r_1)^2}{2\mu r_1}. \tag{2.42}$$

For a given value of τ_1 and μR_1, (2.42) is a transcendental equation of μr_1, the solution of which allows for the determination of $v_1(t)$ from (2.41). Table 2.1 and Fig. 2.5 have been constructed through using the transcendental equation (2.42) to find values for $v_1(t)$ and $r_1(t)$ for the special case of an initial condition at rest, i.e., $P_1=f$, $t_1=0$, $v_{10}=0$, and $R_1=r_{10}$. Table 2.1 and Fig. 2.5 contain four separate cases in which r_{10} is set to 100, 200, 300, and 400 km respectively. In Fig. 2.5, the five thin black lines correspond to constant dimensionless time $S_1 t=1,2,3,4,5$. The values next to the white circles indicate the physical time t. The time values t come from the value we select for the S_1. If the value for S_1 is constant for each case, then the time values associated with the dimensionless time $S_1 t=1,2,3,4,5$ would be the same regardless of the value selected for r_{10}. Another way to select values for S_1 is to mandate that the initial area-averaged mass sink is the same for each choice of r_{10}. This is a relatively realistic assumption if you look at composites of area-averaged rainfall rates in Atlantic and Pacific Ocean basin disturbances and tropical cyclones as shown in Table 2.2. These data suggest that the area-averaged rainfall rates remain constant during the "life cycle" of the tropical cyclone. To make sure that $S_1 r_{10}^2$ is a constant for each case, we choose $S_1=(3\text{ h})^{-1},(12\text{ h})^{-1},(27\text{ h})^{-1},(48\text{ h})^{-1}$ for the four cases $r_{10}=100,200,300,400$ km.

Returning to Fig. 2.5, the 200 km case (blue curve) can be thought of as a small vortex with intense forcing. This case reaches hurricane force winds in 48 h. Contrasting this case with the 400 km case (orange curve), we see that the large vortex with weak forcing has a much longer incubation time. To illustrate this point further, the top panel of Fig. 2.6 shows the intensity as a function of time for each case with the same area-averaged mass sink. Interestingly, during the start of the incubation period, the change in intensity is close to linear. The rate begins to increase only after $S_1 t>1$ or $\mathcal{F}>0.632$. Unlike Fig. 2.1, the intensification rates between each case highly depend on the radial extent of the

mass sink. While these cases start at an initial state of rest, the 400 km case (orange curve) resembles the rapid intensification period from hour 400 to 500 in Ooyama (1969a). While the intensification rate of the 100 km case (red curve) is not representative of cases in observations, the range of cases presented here highlights the importance of the radial extent of the initial area-averaged mass sink distribution in the development of vortices (see Schubert et al. 2016 for a discussion of the potential relevance in other geophysical vortices). Rather than only evalute the intensity, we can also consider the volume of fluid removed from the column between the initial time and time t by taking the integral of (2.37) over the area $\bar{h}-h(r,t)$, which will involve $r\,I_0(\mu_1 r)$ and $r\,K_0(\mu r)$. Through using (2.34) and (2.35), we obtain

$$2\pi\int_0^\infty \left[\bar{h}-h(r,t)\right] r\,dr = \pi r_{10}^2 \bar{h}\mathcal{F}, \tag{2.43}$$

where $\mathcal{F}=1-e^{-S_1 t}$. The left-hand side of (2.43) is the total volume of fluid that has been removed between the initial time $t=0$ and time t. $\pi r_{10}^2\bar{h}$ represents the volume of fluid at the initial time $t=0$. This means that $\mathcal{F}$ can be interpreted as the fraction of volume removed from the fluid from the initial time until time t. Next to the white circles in Fig. 2.5 are the values of t associated with the dimensionless time $S_1 t$ and $\mathcal{F}$. The values $S_1 t$ and $\mathcal{F}$ provide insight into the incubation time for tropical cyclone intensification. The values of $\mathcal{F}$ in Fig. 2.5 indicate that a large fraction of the fluid must be removed before the vortices begin to spin up, e.g., when $S_1 t=2$, $\mathcal{F}=0.865$ and all four of the vortices are sub-23 m s^{-1} in strength. It is important to note that a large fraction $\mathcal{F}$ does not imply that $h\ll\bar{h}$ at the center of the vortex $r=0$. The special case of (2.37) for the center of the vortex $r=0$ is

$$h(0,t)=\bar{h}\left[e^{-\tau_1}+\frac{v_1(t)}{c}\frac{1}{I_1(e^{\tau_1}\mu r_1)}\right]. \tag{2.44}$$

The lower panel of Fig. 2.6 shows the value of $\bar{h}-h(0,t)$ for the four cases $r_{10}=100,200,300,400$ km. From the departures from $\bar{h}$ in Fig. 2.6, we see the fluid depth is only reduced by a small fraction at the center of the vortex for reasonable values of $v_1(t)$. For a comparison to $\bar{h}$, the left panel of Fig. 2.7 shows $\bar{h}-h(r,t)$ for the 200 km case that shows that the largest deviations in height are confined within the region $0\le r\le r_1$. The reason why we do not violate our small Froude number restriction for reasonable values of t is that the absolute angular momentum surfaces contract replacing the removed fluid as mass is removed from the vortex.

In this set of experiments, we terminate the results at 70 m s^{-1} in Figs. 2.5 and 2.6 and the values in Table 2.1 at $S_1 t=5$. This choice is arbitrary, but has been done to keep the examples within a physically

reasonable range and present results acceptable in regards to our small Froude number restriction. It is possible to obtain solutions at $S_1 t \to \infty$. As $S_1 t \to \infty$, $v_1(t) \to c$. Because of the absolute angular momentum principle, $r_1(t)$ for the four cases goes to 1, 4, 9, and 16 km. $r_1(t)$ is prevented from collapsing to a point vortex because $h(0,t) \to 0$ as $S_1 t \to \infty$.

Figures 2.7 and 2.8 show the results for only the 200 km case starting from an initial state of rest. In the plots, $h(r,t)$, $v(r,t)$, and potential vorticity P/f are shown. From the figures, we see that between $t = 0$ and $t = 60$ h, the depth of the fluid falls 300 m from 6371 m to 6071 m. Initially, the drop in the depth of the fluid is small and h does not start to depart from $\bar{h}$ until the rate at which $r_1(t)$ contracts slows. As the radius of maximum velocity collapses from 200 km to 16.7 km, the intensity increases to 59.5 m s^{-1}. As the inset figure in Fig. 2.8 shows, the potential vorticity in the core exponentially increases to 148.4 f by $t = 60$ h.

The results from Figs. 2.5–2.8 display some characteristics similar to those observed in tropical cyclones and in modeling studies. In comparing the analytic results shown here to Ooyama (1969a), we see similar properties such as a change in the incubation time based on the initial size of the vortex and hence the concentration and location of the mass sink. We also note that the work here and Ooyama (1969a) show that initial size plays a role in the final size of the mature vortex. The results presented here also appear to offer insight into rapid intensification in convective aggregation studies with a nonzero, constant Coriolis parameter that use full-physics numerical models (Davis 2015; Wing et al. 2016). The 200 and 300 km cases (blue and green curves in Fig. 2.5) show a qualitatively similar long-incubation time to the vortices presented in these studies.

2.4 Formation and thinning of potential vorticity rings

In order to better understand the effects of eyewall formation, we generalize the two-region model into a three-region model. We assume that the mass sink is piecewise constant in the three regions: an inner region $0 \le r < r_1(t)$ that we define as the "core," an annular region $r_1(t) < r < r_2(t)$ that we define as the "eyewall" region, and a region $r_2(t) < r < \infty$ that we define as the "far-field" region. The mass sink is given by

$$S(r,t) = \begin{cases} S_1 & \text{if } 0 \le r < r_1(t) \\ S_2 & \text{if } r_1(t) < r < r_2(t) \\ 0 & \text{if } r_2(t) < r < \infty, \end{cases} \tag{2.45}$$

TABLE 2.1. Solutions of the transcendental equation (2.42) for the choices $c = 250$ m s^{-1}, $f = 5 \times 10^{-5}$ s^{-1}, $\tau_1 = S_1 t$, and $R_1 = r_{10}$ (initial state of rest), with four different choices for r_{10}.

		$r_{10} = 100$ km		$r_{10} = 200$ km		$r_{10} = 300$ km		$r_{10} = 400$ km	
$S_1 t$	P/f (core)	$r_1(t)$ (km)	$v_1(t)$ (m s^{-1})	$r_1(t)$ (km)	$v_1(t)$ (m s^{-1})	$r_1(t)$ (km)	$v_1(t)$ (m s^{-1})	$r_1(t)$ (km)	$v_1(t)$ (m s^{-1})
0.0	1.0	100.0	0.0	200.0	0.0	300.0	0.0	400.0	0.0
0.5	1.6	77.9	1.3	155.9	2.5	233.9	3.8	312.2	5.0
1.0	2.7	60.7	2.6	121.4	5.2	182.4	7.8	243.6	10.3
1.5	4.5	47.3	4.1	94.6	8.2	142.2	12.3	190.0	16.3
2.0	7.4	36.8	5.9	73.7	11.7	110.9	17.5	148.3	23.3
2.5	12.2	28.7	8.0	57.5	16.0	86.5	23.9	115.8	31.7
3.0	20.1	22.3	10.6	44.8	21.2	67.5	31.7	90.5	41.9
3.5	33.1	17.4	13.9	34.9	27.8	52.7	41.4	70.9	54.6
4.0	54.6	13.6	18.1	27.3	36.0	41.3	53.5	55.7	70.4
4.5	90.0	10.6	23.4	21.3	46.4	32.4	68.6	44.1	89.7
5.0	148.4	8.2	30.1	16.7	59.5	25.6	87.3	35.2	112.8

TABLE 2.2. Composite data of the radial distribution of rainfall rates (cm day^{-1}) in tropical systems in the Atlantic (denoted as hurricane) and Pacific (denoted as typhoon) basins. The data is in 2 degree bins (~ 200 km). Reproduced from Schubert and Hack (1982), which is based on data from Gray (1981).

	0–2°	2–4°	4–6°	6–8°	8–10°	Area-average
Pre-hurricane	1.9	1.5	0.9	0.5	0.5	0.76
Hurricane	6.3	2.0	0.7	0.3	0.5	0.86
Pre-typhoon	3.4	2.6	1.5	0.7	0.7	1.20
Typhoon	8.3	2.3	0.1	0.8	0.7	1.10

where S_1 and S_2 are constants. With the forcing (2.45) and the piecewise constant initial condition

$$P(r,0) = \begin{cases} P_1 & \text{if } 0 \le r < r_{10} \\ P_2 & \text{if } r_{10} < r < r_{20} \\ f & \text{if } r_{20} < r < \infty, \end{cases} \tag{2.46}$$

an analysis similar to that given in the last section shows that the solution of (2.19) is

$$P(r,t) = f \begin{cases} e^{\tau_1} & \text{if } 0 \le r < r_1(t) \\ e^{\tau_2} & \text{if } r_1(t) < r < r_2(t) \\ 1 & \text{if } r_2(t) < r < \infty, \end{cases} \tag{2.47}$$

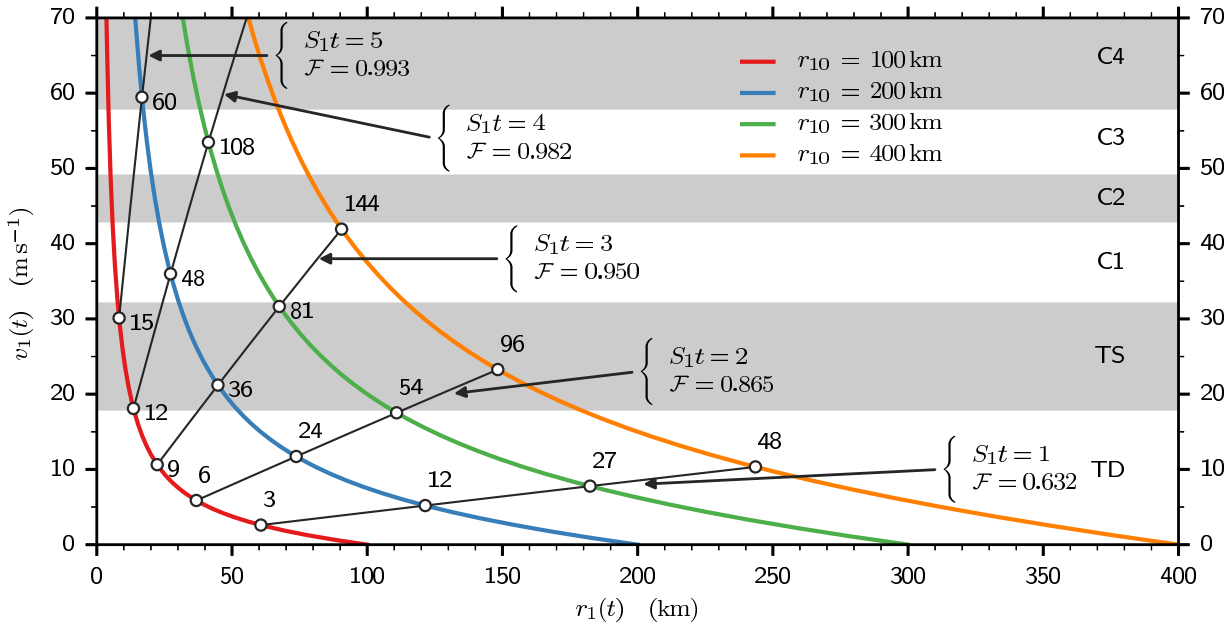

FIG. 2.5. $v_1(t)$ versus $r_1(t)$ for four vortices that evolve from resting initial states with r_{10} =100, 200, 300, 400 km. Labels on the right stand for tropical depression (TD), tropical storm (TS), and Category 1–4 hurricanes. Along the five thin black lines, the dimensionless time takes on the respective values $S_1 t = 1, 2, 3, 4, 5$, while the fractional volume removed takes on the respective values $\mathcal{F} = 0.632, 0.865, 0.950, 0.982, 0.993$. The numbers along each curve denote the time (in hours) under the assumption that the respective values of S_1 are $(3\,\text{h})^{-1}$, $(12\,\text{h})^{-1}$, $(27\,\text{h})^{-1}$, and $(48\,\text{h})^{-1}$, which means that $S_1 r_{10}^2$ is the same on each colored curve.

where $\tau_1 = S_1(t+t_1)$, $\tau_2 = S_2(t+t_2)$, and t_1 and t_2 are defined by $e^{S_1 t_1} = P_1/f$ and $e^{S_2 t_2} = P_2/f$. With the solution (2.47) for $P(r,t)$, the invertibility principle (2.27) takes the form

$$\begin{cases} \dfrac{\partial^2 h}{\partial r^2} + \dfrac{\partial h}{r\,\partial r} - \mu_1^2 h = -\mu_1^2 \bar{h} e^{-\tau_1} & \text{if } 0 \le r < r_1(t) \\ \dfrac{\partial^2 h}{\partial r^2} + \dfrac{\partial h}{r\,\partial r} - \mu_2^2 h = -\mu_2^2 \bar{h} e^{-\tau_2} & \text{if } r_1(t) < r < r_2(t) \\ \dfrac{\partial^2 h}{\partial r^2} + \dfrac{\partial h}{r\,\partial r} - \mu^2 h = -\mu^2 \bar{h} & \text{if } r_2(t) < r < \infty, \end{cases} \tag{2.48}$$

where

$$\mu_1(t) = \mu e^{\tau_1}, \quad \mu_2(t) = \mu e^{\tau_2}, \quad \text{and} \quad \mu = \frac{f}{c},$$

are the inverse Rossby lengths in each of the three regions. Note that the Rossby length $\mu^{-1} = (c/f)$ in the far-field region is fixed, while the Rossby length $(c/f)e^{-\tau_1}$ in the core region and the Rossby length $(c/f)e^{-\tau_2}$ in the eyewall region both decrease exponentially with time.

We can now solve the invertibility problem (2.48) in the entire domain by first solving it in each of the subregions, enforcing the boundary conditions $r = 0$ and $r \to \infty$, and matching the solutions for h

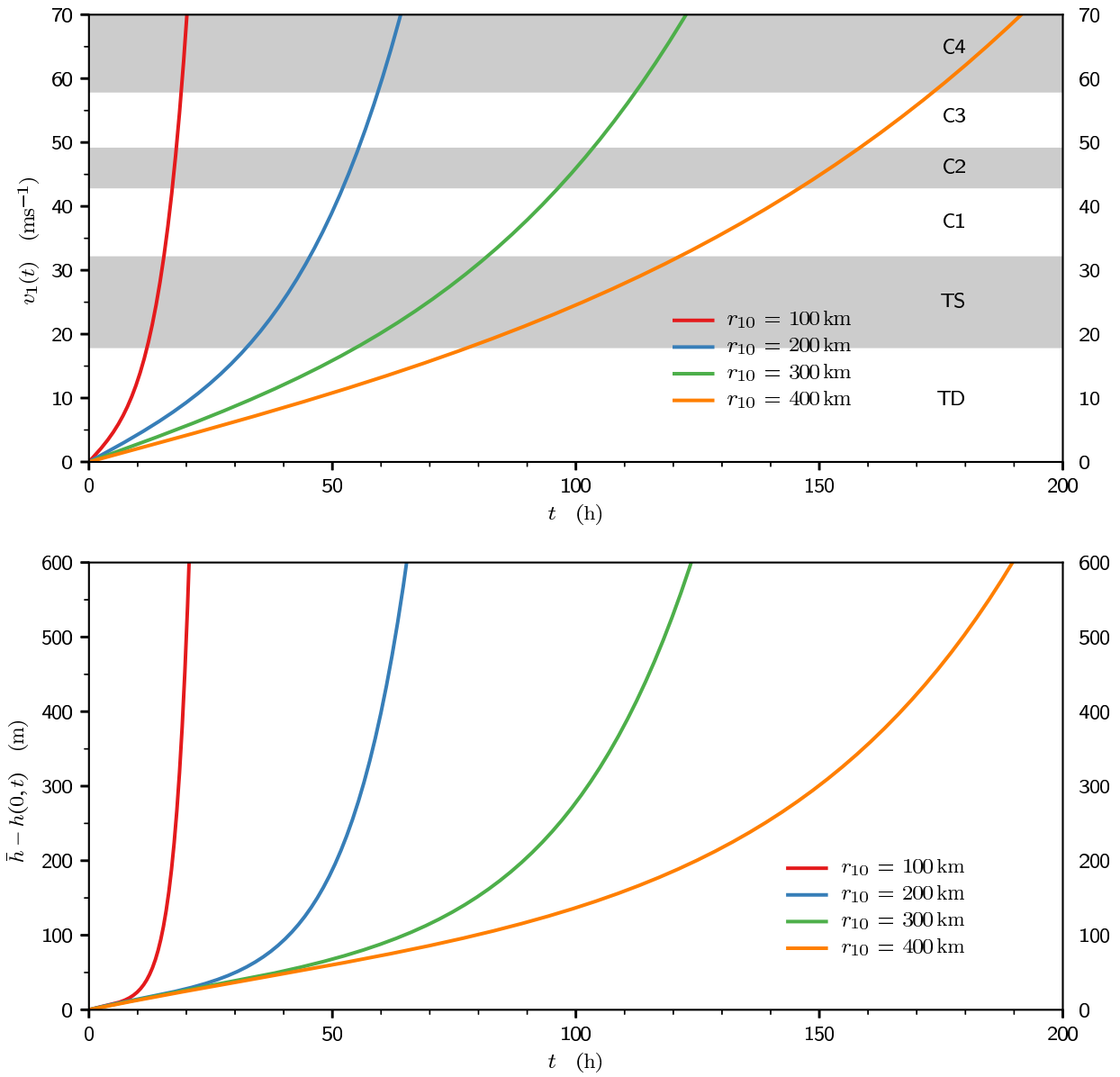

FIG. 2.6. $v_1(t)$ (top) and $\bar{h}-h(0,t)$ (bottom) two-region model results for four vortices that evolve from resting initial states with $r_{10} = 100$, 200, 300, 400 km as shown in Fig. 2.5. Labels on the right of the top panel stand for tropical depression (TD), tropical storm (TS), and Category 1–4 hurricanes. The values of S_1 for the four vortices are $(3\,\mathrm{h})^{-1}$, $(12\,\mathrm{h})^{-1}$, $(27\,\mathrm{h})^{-1}$, and $(48\,\mathrm{h})^{-1}$, which means that $S_1 r_{10}^2$ is the same on each colored curve. The bottom panel is calculated using (2.44).

and v at $r = r_1(t)$ and $r = r_2(t)$. For example, in the core region, the solution for h consists of the sum of the particular solution $\bar{h}e^{-\tau_1}$ and the homogeneous solution proportional to the zero order modified Bessel function of the first kind $I_0(\mu_1 r)$, with the other homogeneous solution the zero order modified Bessel function of the second kind $K_0(\mu_1 r)$ discarded because it is unbounded at $r = 0$ as shown in Fig. 2.4. In the far-field region, the solution for h consists of the sum of the particular solution $\bar{h}$ and the

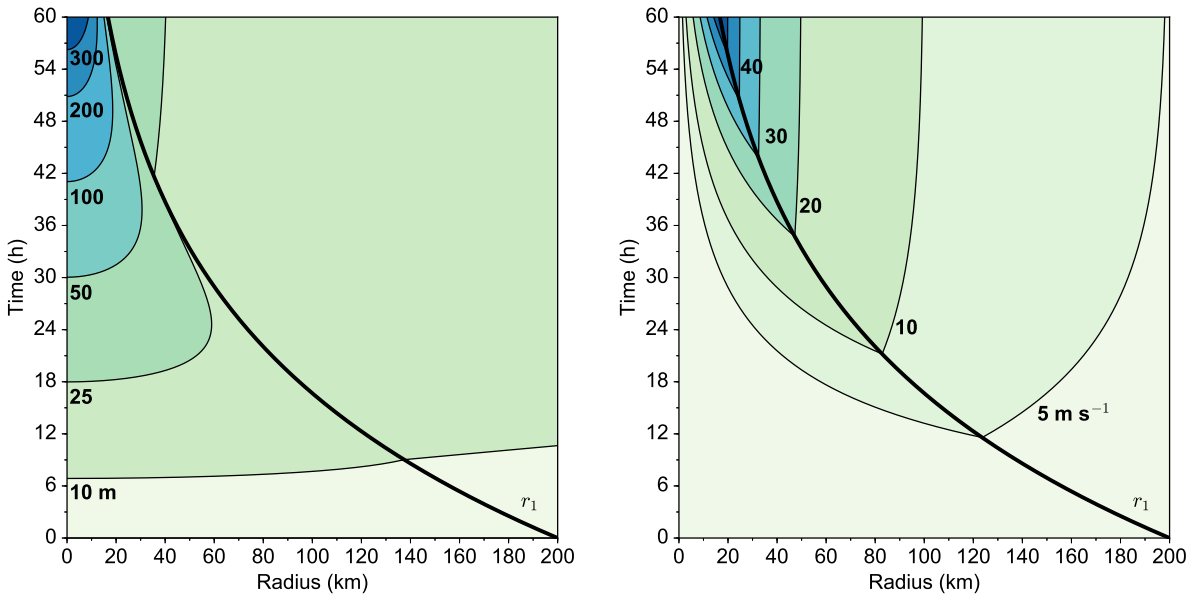

FIG. 2.7. Isolines of the depth anomaly $\bar{h} - h(r,t)$ (left) and of the tangential wind $v(r,t)$ (right), with the 50 m s^{-1} contour unlabeled. These results are for a two-region vortex that evolves from a resting initial state with $r_{10} = 200$ km and $S_1 = (12\,\text{h})^{-1}$. The angular momentum surface $r_1(t)$ indicated by the thick black line moves inward with time. The value of $\bar{h}$ is 6371 m, which means that the contour for the 300 m depth anomaly corresponds to a fluid depth of 6071 m.

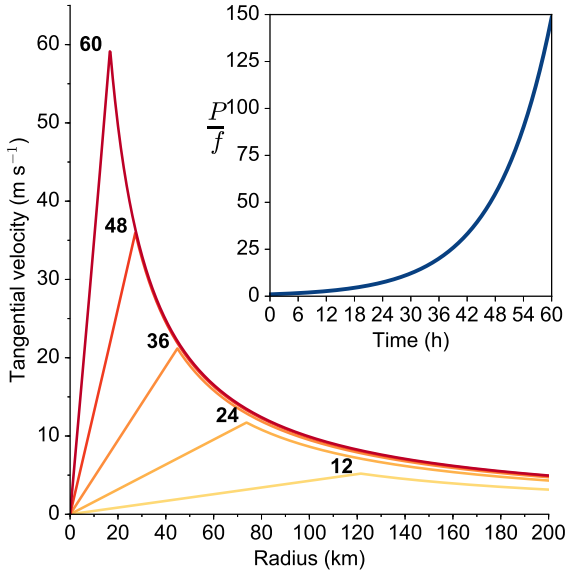

FIG. 2.8. Tangential velocity $v(r,t)$ versus r for a vortex that evolves from a resting state with $r_{10} = 200$ km and $S_1 = (12\text{ h})^{-1}$. The five radial profiles of $v(r,t)$ correspond to $t = 12, 24, 36, 48, 60$ h, with the kinks occurring at the absolute angular momentum surface $r = r_1(t)$. The inset figure shows $P(t)/f$ in the core region $0 \le r < r_1(t)$.

homogeneous solution proportional to $K_0(\mu r)$, with the other homogeneous solution $I_0(\mu r)$ discarded because it is unbounded at $r \to \infty$. In the eyewall region, the solution for h is the sum of the particular solution $\bar{h}e^{-\tau_2}$ and the homogeneous solution, which consists of a linear combination of $I_0(\mu_2 r)$ and $K_0(\mu_2 r)$. The solution for the fluid depth takes the form

$$h(r,t) = \bar{h} \begin{cases} e^{-\tau_1} + \dfrac{\upsilon_1(t)}{c} \dfrac{I_0(e^{\tau_1}\mu r)}{I_1(e^{\tau_1}\mu_1 r)} & \text{if } 0 \le r \le r_1(t) \\ e^{-\tau_2} + \dfrac{\upsilon_1(t)}{c} \dfrac{F(e^{\tau_2}\mu r, e^{\tau_2}\mu r_2)}{G(e^{\tau_2}\mu r_1, e^{\tau_2}\mu r_2)} - \dfrac{\upsilon_2(t)}{c} \dfrac{F(e^{\tau_2}\mu r, e^{\tau_2}\mu r_1)}{G(e^{\tau_2}\mu r_1, e^{\tau_2}\mu r_2)} & \text{if } r_1(t) \le r \le r_2(t) \\ 1 - \dfrac{\upsilon_2(t)}{c} \dfrac{K_0(\mu r)}{K_1(\mu r_2)} & \text{if } r_2(t) \le r \le \infty, \end{cases} \tag{2.49}$$

where $\upsilon_1(t)$ and $\upsilon_2(t)$ are as yet undetermined functions and

$$F(x,y) = I_0(x)K_1(y) + K_0(x)I_1(y), \tag{2.50}$$

$$G(x,y) = I_1(x)K_1(y) - K_1(x)I_1(y). \tag{2.51}$$

Note that the special case of (2.49) for the center of the vortex $r = 0$ is (2.44), the same as the two-region model. The corresponding solution for the azimuthal wind can be found from the balance relation (2.16) and the modified Bessel function derivative relations (2.32) and (2.33), from which it follows that

$$\frac{\partial F(e^{\tau_2}\mu r, e^{\tau_2}\mu r_2)}{\partial r} = e^{\tau_2}\mu G(e^{\tau_2}\mu r, e^{\tau_2}\mu r_2), \tag{2.52}$$

$$\frac{\partial F(e^{\tau_2}\mu r, e^{\tau_2}\mu r_1)}{\partial r} = -e^{\tau_2}\mu G(e^{\tau_2}\mu_1 r, e^{\tau_2}\mu r). \tag{2.53}$$

The solution for $\upsilon(r,t)$ is

$$\upsilon(r,t) = \begin{cases} \upsilon_1(t) \dfrac{I_1(e^{\tau_1}\mu r)}{I_1(e^{\tau_1}\mu r_1)} & \text{if } 0 \le r \le r_1(t) \\ \upsilon_1(t) \dfrac{G(e^{\tau_2}\mu r, e^{\tau_2}\mu r_2)}{G(e^{\tau_2}\mu r_1, e^{\tau_2}\mu r_2)} + \upsilon_2(t) \dfrac{G(e^{\tau_2}\mu r_1, e^{\tau_2}\mu r)}{G(e^{\tau_2}\mu r_1, e^{\tau_2}\mu r_2)} & \text{if } r_1(t) \le r \le r_2(t) \\ \upsilon_2(t) \dfrac{K_1(\mu r)}{K_1(\mu r_2)} & \text{if } r_2(t) \le r \le \infty. \end{cases} \tag{2.54}$$

Note that the continuity of $\upsilon(r,t)$ at $r = r_1(t)$ and $r = r_2(t)$ follows directly from the fact that $G(x,x) = 0$. The continuity of $h(r,t)$ at $r = r_1(t)$ and $r = r_2(t)$ leads to the relations

$$\frac{\upsilon_1(t)}{c}\left(\frac{I_0(e^{\tau_1}\mu r_1)}{I_1(e^{\tau_1}\mu r_1)} - \frac{F(e^{\tau_2}\mu r_1, e^{\tau_2}\mu r_2)}{G(e^{\tau_2}\mu r_1, e^{\tau_2}\mu r_2)}\right) + \frac{\upsilon_2(t)}{c}\left(\frac{1}{e^{\tau_2}\mu r_1 G(e^{\tau_2}\mu r_1, e^{\tau_2}\mu r_2)}\right) = e^{-\tau_2} - e^{-\tau_1}, \tag{2.55}$$

and

$$\frac{v_1(t)}{c}\left(\frac{1}{e^{\tau_2}\mu r_1 G(e^{\tau_2}\mu r_1, e^{\tau_2}\mu r_2)}\right)+\frac{v_2(t)}{c}\left(\frac{K_0(\mu r_2)}{K_1(\mu r_2)}-\frac{F(e^{\tau_2}\mu r_2, e^{\tau_2}\mu r_1)}{G(e^{\tau_2}\mu r_1, e^{\tau_2}\mu r_2)}\right)=1-e^{-\tau_2}, \tag{2.56}$$

where we have made use of the Wronskian (2.36) to write $F(x,x)=1/x$.

Because of the absolute angular momentum principle, the radius $r_1(t)$ is related to the azimuthal wind $v_1(t)$ by $r_1 v_1+\frac{1}{2}f r_1^2=\frac{1}{2}f R_1^2$, where the constant R_1 is the potential radius surface of the interface between the core and the eyewall region. Similarly, the radius $r_2(t)$ is related to the azimuthal wind $v_2(t)$ by $r_2 v_2+\frac{1}{2}f r_2^2=\frac{1}{2}f R_2^2$, where the constant R_2 is the potential radius surface of the interface between the eyewall region and the far-field region. These absolute angular momentum principles can be written in the forms

$$\frac{v_1(t)}{c}=\frac{(\mu R_1)^2-(\mu r_1)^2}{2\mu r_1}, \tag{2.57}$$

$$\frac{v_2(t)}{c}=\frac{(\mu R_2)^2-(\mu r_2)^2}{2\mu r_2}. \tag{2.58}$$

For any given t, the four quantities r_1, r_2, v_1, and v_2 must satisfy (2.54)–(2.58). Equations (2.57) and (2.58) can be used to eliminate v_1 and v_2 from (2.54) and (2.55) resulting in a coupled pair of transcendental equations for μr_1 and μr_2 at the given t. Through using the transcendental equations, we have solutions of r_1, r_2, v_1, and v_2 as shown in Table 2.3 and Figs. 2.9 and 2.10. For this three-region model, we have chosen a configuration in which $c=250$ m s^{-1}, $f=5\times10^{-5}$ s^{-1}, $r_{10}=100$ km, $r_{20}=200$ km, $S_1=(16\,\mathrm{h})^{-1}$, $S_2=(9\,\mathrm{h})^{-1}$, $t_1=28$ h, and $t_2=0$. These choices result in a non-resting initial state with $P_1=5.75f$, $P_2=f$, $v_{10}=11.8$ m s^{-1}, and $v_{20}=5.9$ m s^{-1}, i.e., the radius of maximum wind is on the R_1 surface initially. As can be seen from Table 2.3, $r_2(t)$ moves inward faster than $r_1(t)$ so that v_2 grows faster than v_1. By $t=48$ h, $r_2-r_1\approx3$ km and $v_2-v_1\approx21.4$ m s^{-1}, i.e., a structure closely resembling a vortex sheet has developed as can be seen in Figs. 2.9 and 2.10. From the last two columns in Table 2.3 and the inset diagram in Fig. 2.10, the core potential vorticity exceeds the eyewall potential vorticity until $t=36$ h, after which, the potential vorticity within the eyewall region is larger. In other terms, the potential vorticity field has a monopole structure before 36 h, but as the potential vorticity between r_1 and r_2 grows, a thinning ring of potential vorticity evolves after 36 h. Another interesting aspect of this result is that $v_1>v_2$ for $t<19$ h, while $v_1<v_2$ for $t>19$ h. In other words, the radius of maximum tangential wind jumps from the R_1 absolute angular momentum surface to R_2 at $t\approx19$ h. In effect, the absolute angular momentum surfaces between

TABLE 2.3. Solutions of equations (2.55)–(2.58) for the choices $c = 250$ m s^{-1}, $f = 5 \times 10^{-5}$ s^{-1}, $r_{10} = 100$ km, $r_{20} = 200$ km, $S_1 = (16\,\text{h})^{-1}$, $S_2 = (9\,\text{h})^{-1}$, $t_1 = 28$ h, and $t_2 = 0$. The initial vortex has a maximum wind of 11.8 m s^{-1} at a radius of 100 km.

t (h)	$r_1(t)$ (km)	$r_2(t)$ (km)	$v_1(t)$ (m s^{-1})	$v_2(t)$ (m s^{-1})	P/f (core)	P/f (eyewall)
0	100.0	200.0	11.8	5.9	5.8	1.0
6	83.0	149.4	15.2	10.8	8.4	1.9
12	68.9	112.6	19.0	16.5	12.2	3.8
18	57.3	85.8	23.6	23.2	17.7	7.4
24	47.6	66.1	28.9	31.3	25.8	14.4
30	39.6	51.5	35.1	41.0	37.5	28.0
36	33.0	40.6	42.5	52.6	54.6	54.6
42	27.6	32.4	51.1	66.4	79.4	106.3
48	23.2	26.2	61.2	82.6	115.6	207.1

R_1 and R_2 moved inward across the radius of maximum wind. This scenario is consistent with the results shown by Stern et al. (2015), who argue that in real and model tropical cyclones, contraction of the radius of maximum wind often ceases before peak intensity is reached. This scenario is also consistent with the arguments of Smith and Montgomery (2015) that the movement of the absolute angular momentum surfaces is fundamental to understanding intensification. The authors argue that there is not a one-to-one relationship between these surfaces and the radius of maximum wind and even if the radius of maximum wind ceases to contract, an inward movement of the absolute angular momentum surfaces must accompany vortex intensification.

2.5 MULTI-REGION MODEL OF TROPICAL CYCLONE INTENSIFICATION

In this section, we generalize the two- and three-region forced, balanced model solutions to an arbitrary number of regions. Using this version of the model, we can improve our understanding of the relationship between intensity and the size of tropical cyclones. Again, we consider the case in which both the mass sink $S(r,t)$ and potential vorticity $P(r,t)$ are piecewise uniform in radius. The discontinuities in the two fields occur at the points $r_j(t)$, where $j = 1,2,\cdots,J$. The functions $r_j(t)$ have not yet been determined. Because of (2.4), each of these radii is an absolute angular momentum surface that moves inward as the vortex intensifies. This means that determining $r_j(t)$ is critical to understand the radial inflow. We shall refer to the region $0 \le r < r_1(t)$ as the "innermost region," the region $r_{j-1}(t) < r < r_j(t)$ as the "j$^{\text{th}}$ region," and the region $r_J(t) < r < \infty$ as the "far-field" region. In

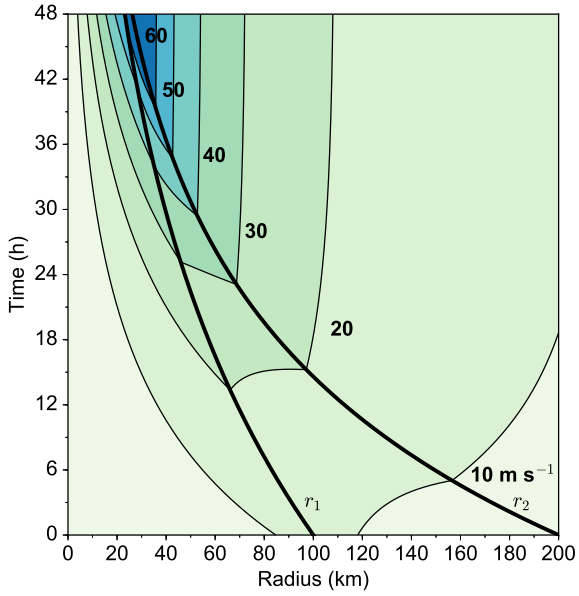

FIG. 2.9. Isolines of the tangential wind $\upsilon(r,t)$ for the three-region model. The two thick black lines show the inward movement of the absolute angular momentum surface $r_1(t)$ and $r_2(t)$. Note that $r_1(t)$ at $t=0$ is starting from a non-resting initial state.

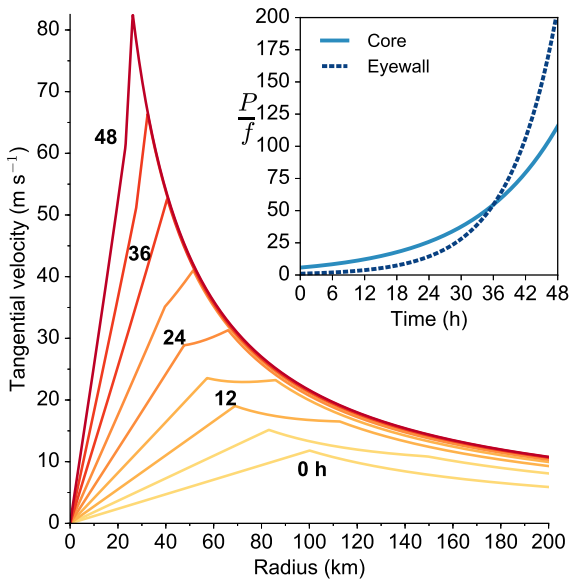

FIG. 2.10. Radial profiles of tangential wind $\upsilon(r,t)$ at 6-h intervals for the three-region model. The kinks in $\upsilon(r,t)$ occur at the absolute angular momentum surfaces $r_1(t)$ and $r_2(t)$. With regards to the kinks in the three-region model, the radius of maximum wind shifts from r_1 to r_2 at $t \approx 18$ h. As with Fig. 2.8, the inset shows the potential vorticity. In this case, potential vorticity is shown for the core and eyewall region. Note, the vortex initially has a monotonic potential vorticity structure that switches to a hollow potential vorticity structure at $t \approx 36$ h.

the far-field region, we assume that there is no mass sink and that the potential vorticity remains equal to f for all time. The mass sink is given by

$$S(r,t) = S_j(t) \quad \text{for } r_{j-1}(t) < r < r_j(t), \tag{2.59}$$

where the $S_j(t)$ are specified functions of time for the $j = 1, 2, \cdots, J$. Because of the form of the mass sink (2.59), an initial piecewise uniform potential vorticity remains piecewise uniform with (2.19) simplifying to

$$\frac{\partial P}{\partial t} = S_j P \quad \text{for } r_{j-1}(t) < r < r_j(t). \tag{2.60}$$

The piecewise uniform initial condition on P is

$$P(r,0) = P_j \quad \text{for } r_{j-1,0} < r < r_{j,0}, \tag{2.61}$$

where the constants P_j are the initial values of the potential vorticity and $r_{j,0}$ are the initial values of $r_j(t)$. With this initial condition, the solution of (2.60) is

$$P(r,t) = f e^{\tau_j(t)} \quad \text{for } r_{j-1}(t) < r < r_j(t), \quad \text{where } \tau_j(t) = \tau_{j,0} + \int_0^t S_j(t')\, dt', \tag{2.62}$$

is the dimensionless time for the j^{th} region, and where the constants $\tau_{j,0}$ are defined in terms of the initial conditions by $e^{\tau_{j,0}} = P_j / f$. A simple interpretation of (2.62) is that each region has its own clock by which it exponentially grows the potential vorticity.

The diagnosis of the mass and wind fields from the potential vorticity field (2.62) requires solving the invertibility principle. The invertibility principle for h can be derived by combining the definition of the potential vorticity P with the balance condition (2.16) to obtain

$$\frac{\partial}{r\,\partial r}\left(\frac{r}{P}\frac{\partial h}{\partial r}\right) - \frac{Ph}{g\bar{h}} = -\frac{f}{g}. \tag{2.63}$$

With the solutions (2.62) for $P(r,t)$, the invertibility principle (2.63) takes the form

$$\frac{\partial^2 h}{\partial r^2} + \frac{\partial h}{r\,\partial r} - \mu_j^2 h = -\mu_j^2 \bar{h} e^{-\tau_j(t)} \quad \text{for } r_{j-1}(t) < r < r_j(t), \tag{2.64}$$

where $\mu = f/c$ is the inverse Rossby length in the far-field region and

$$\mu_j(t) = \mu e^{\tau_j(t)} \quad \text{for } j = 1, 2, \cdots, J \tag{2.65}$$

are the inverse Rossby length in the other J regions. As with the two- and three-region models, the Rossby length (c/f) in the far-field region is fixed, while the Rossby lengths $(c/f)e^{-\tau_j(t)}$ in the other J regions decrease exponentially with time in regions where S_j and $\tau_{j,0}$ are nonzero.

We can solve the invertibility problem (2.64) in the entire domain by first solving for the invertibility problem within each subregion, then enforcing the boundary conditions for $r=0$ and $r\to\infty$, and finally matching the solutions for h and v at each $r_j(t)$. For example, in the innermost region $0\le r< r_1(t)$, the solution for h consists of the sum of the particular solution $\bar{h}e^{-\tau_1(t)}$ and the homogeneous solution proportional to $I_0(\mu_1 r)$, with the other homogeneous solution $K_0(\mu_1 r)$ discarded because it is unbounded at $r=0$. Similarly, in the far-field region, the solution for h consists of the sum of the particular solution $\bar{h}$ and the homogeneous solution proportional to $K_0(\mu r)$, with the other homogeneous solution $I_0(\mu r)$ discarded because it is unbounded as $r\to\infty$. In the j^{th} region $r_{j-1}<r<r_j(t)$, the solution for h is the sum of the particular solution $\bar{h}e^{-\tau_j(t)}$ and the homogeneous solution, which consists of a linear combination of $I_0(\mu_j r)$ and $K_0(\mu_j r)$, or alternatively, a linear combination of $F(\mu_j r,\mu_j r_j)$ and $F(\mu_j r,\mu_j r_{j-1})$, where F is defined in (2.67). Then, choosing the coefficients in such a way that anticipates the requirement of continuity of $v(r,t)$ at each $r_j(t)$, the solutions for the fluid depth can be written in the form

$$h(r,t)=\bar{h}\begin{cases} e^{-\tau_1(t)}+\dfrac{v_1(t)}{c}\dfrac{I_0(\mu_1 r)}{I_1(\mu_1 r_1)} & \text{if } 0\le r\le r_1(t)\\[2ex] e^{-\tau_j(t)}+\dfrac{1}{c}\dfrac{v_{j-1}(t)F(\mu_j r,\mu_j r_j)-v_j(t)F(\mu_j r,\mu_j r_{j-1})}{G(u_j r_{j-1},\mu_j r_j)} & \text{if } r_{j-1}(t)\le r\le r_j(t)\\[2ex] 1-\dfrac{v_J(t)}{c}\dfrac{K_0(\mu r)}{K_1(\mu r_J)} & \text{if } r_J(t)\le r<\infty, \end{cases} \tag{2.66}$$

where the values of $v_j(t)$ are as yet undetermined and where

$$F(x,y)=I_0(x)K_1(y)+K_0(y)I_1(y), \tag{2.67}$$

$$G(x,y)=I_1(x)K_1(y)-K_1(x)I_1(y). \tag{2.68}$$

The corresponding solution for the azimuthal wind can be found from the balance relation (2.16) and the Wronskian (2.36).

It follows that $F_x(x,y)=G(x,y)=-G(y,x)$. Thus, the solution for $v(r,t)$ is

$$v(r,t)=\begin{cases} v_1(t)\dfrac{I_1(\mu_1 r)}{I_1(\mu_1 r_1)} & \text{if } 0\le r\le r_1(t) \\ \dfrac{v_{j-1}G(\mu_j r,\mu_j r_j)+v_j(t)G(\mu_j r_{j-1},\mu_j r)}{G(\mu_j r_{j-1},\mu_j r_j)} & \text{if } r_{j-1}(t)\le r\le r_j(t) \\ v_J(t)\dfrac{K_1(\mu r)}{K_1(\mu r_J)} & \text{if } r_J(t)\le r<\infty. \end{cases} \tag{2.69}$$

Note that (2.69), along with the fact that $G(x,x)=0$, guarantees that $v(r,t)$ is continuous at $r=r_{j-1}(t)$ and $r=r_j(t)$, thus validating the choice of the coefficients in (2.66).

To summarize the development of the j^{th} region model so far, we have obtained the solution (2.62) for the potential vorticity field $P(r,t)$, the solution (2.66) for the height field $h(r,t)$, and the solution (2.69) for the tangential wind field $v(r,t)$. However, we have yet to determine the values of $r_j(t)$ and $v_j(t)$. For a given time t, the values of $r_j(t)$ and $v_j(t)$ will now be determined by requiring that $h(r,t)$ is continuous at $r_j(t)$ and that $r_j(t)$ and $v_j(t)$ are consistent with the angular momentum principle. The continuity of $h(r,t)$ at $r=r_1(t)$, $r=r_j(t)$ for $2\le j\le J-1$, and $r=r_J(t)$ leads to the relations

$$\frac{v_1^{(\nu+1)}(t)}{c}\left(\frac{I_0\left(\mu_1 r_1^{(\nu)}\right)}{I_1\left(\mu_1 r_1^{(\nu)}\right)}-\frac{F\left(\mu_2 r_1^{(\nu)},\mu_2 r_2^{(\nu)}\right)}{G\left(\mu_2 r_1^{(\nu)},\mu_2 r_2^{(\nu)}\right)}\right)+\frac{v_2^{(\nu+1)}(t)}{c}\left(\frac{1}{\mu_2 r_1^{(\nu)}G\left(\mu_2 r_1^{(\nu)},\mu_2 r_2^{(\nu)}\right)}\right)=e^{-\tau_2(t)}-e^{-\tau_1(t)}, \tag{2.70}$$

$$\begin{aligned}\frac{v_{j-1}^{(\nu+1)}(t)}{c}\left(\frac{1}{\mu_j r_j G\left(\mu_j r_{j-1}^{(\nu)},\mu_j r_j^{(\nu)}\right)}\right)-\frac{v_j^{(\nu+1)}(t)}{c}\left(\frac{F\left(\mu_j r_j^{(\nu)},\mu_j r_{j-1}^{(\nu)}\right)}{G\left(\mu_j r_{j-1}^{(\nu)},\mu_j r_j^{(\nu)}\right)}+\frac{F(\mu_{j+1} r_j^{(\nu)},\mu_{j+1} r_{j+1}^{(\nu)})}{G\left(\mu_{j+1} r_j^{(\nu)},\mu_{j+1} r_{j+1}^{(\nu)}\right)}\right)\\ +\frac{v_{j+1}^{(\nu+1)}(t)}{c}\left(\frac{1}{\mu_{j+1} r_j^{(\nu)}G\left(\mu_{j+1} r_j^{(\nu)},\mu_{j+1} r_{j+1}^{(\nu)}\right)}\right)=e^{-\tau_{j+1}(t)}-e^{-\tau_j(t)},\end{aligned} \tag{2.71}$$

$$\frac{v_{J-1}^{(\nu+1)}(t)}{c}\left(\frac{1}{\mu_J r_J G\left(\mu_J r_{J-1}^{(\nu)},\mu_J r_J^{(\nu)}\right)}\right)+\frac{v_J^{(\nu+1)}(t)}{c}\left(\frac{K_0\left(\mu r_J^{(\nu)}\right)}{K_1\left(\mu r_J^{(\nu)}\right)}-\frac{F\left(\mu_J r_J^{(\nu)},\mu_J r_{J-1}^{(\nu)}\right)}{G\left(\mu_J r_{J-1}^{(\nu)},\mu_J r_J^{(\nu)}\right)}\right)=1-e^{-\tau_J(t)}, \tag{2.72}$$

where we have made use of the Wronskian (2.36) to write $F(x,x)=1/x$. Because of the absolute angular momentum principle, the radius $r_j(t)$ is related to the azimuthal wind $v_j(t)$ by $r_j(t)v_j(t)+\frac{1}{2}f r_j^2(t)=\frac{1}{2}f R_j^2$, where R_j is the potential radius of the j^{th} interface. This angular momentum relation can be viewed as a quadratic equation for $r_j(t)$, with the solution expressed in the form

$$r_j^{(\nu+1)}(t)=\left(R_j^2+\frac{v_j^{2(\nu+1)}(t)}{f^2}\right)^{1/2}-\frac{v_j^{(\nu+1)}(t)}{f} \qquad \text{for} \quad j=1,2,\cdots,J, \tag{2.73}$$

where we have chosen the root that yields $r_j(t) > 0$. Thus, for a given t, the $2J$ quantities $r_j^{(\nu+1)}(t)$ and $v_j^{(\nu+1)}(t)$ for $j = 1, 2, \cdots, J$ must satisfy the $2J$ equations (2.70)–(2.73). The solution of these equations requires iteration. While there are several ways to proceed, we have chosen the following iterative procedure. From the current estimates of $r_j^{(\nu)}$, all the coefficients of $v_j^{(\nu+1)}$ in (2.70)–(2.72) are known, so that these equations form a tridiagonal linear algebraic system for the unknown $v_j^{(\nu+1)}$'s. After solving the tridiagonal system for the $v_j^{(\nu+1)}$'s, the $r_j^{(\nu+1)}$'s are updated through (2.73), after which this iterative cycle repeats until convergence is reached.

2.5.1 Examples from the multi-region model

The multi-region forced, balanced model of tropical cyclone intensification allows for complicated configurations of the radial distribution of the mass sink. In the two-region model, all the absolute angular momentum surfaces within r_1 act in unison. With more complicated distributions of the mass sink in the multi-region cases, the inward shift of outer absolute angular momentum surfaces is controlled by the inward shift of inner surfaces. Figure 2.11 shows a (r, v) space diagram with results from an example in which the number of regions have been expanded from three to six. In the figure, there are two example experiments in which the mass sink decreases linearly radially outward from the center of the vortex (orange case) and increases linearly radially outward from the center (blue case) in a manner that does not have a constant area-averaged mass sink between the two cases as shown by the inset bar plot where shorter bars represent a stronger mass sink. The black curves are absolute angular momentum surfaces $R_0 = 50, 150, 250, 350, 450$ and define the interfaces between the regions. While both vortices have similar intensities and structures at 24 h, the distribution of the mass sink in the blue case inhibits the rate of intensification in comparison to the orange case as the outer R surfaces cannot collapse with the same ease as the orange vortex. This is caused by the outer absolute angular momentum surfaces in the blue case being delayed until the inner surfaces contract despite having a larger area-averaged mass sink in the orange case. To explore this effect further, we design a series of cases with the same area-averaged mass sink but a different radial distribution.

In this set of experiments, the time-independent mass sink is given by

$$S_j = A \begin{cases} \alpha e^{-\bar{r}_j^2/a^2} + (1-\alpha)(\bar{r}/b)^2 e^{-\bar{r}_j^2/b^2} & \text{if } 1 \le j \le J \\ 0 & \text{if } j = J+1, \end{cases} \tag{2.74}$$

where $\bar{r} = \frac{1}{2}(r_{j-1} + r_j)$ and a, b, and α are constants. The constant A will be determined by a normalization procedure. Integrating (2.74) over the area inside $r = r_J$, we obtain

$$A = \frac{\bar{S} r_J^2}{\sum_{j=1}^{J} \left\{ \left[\alpha e^{-\bar{r}_j^2/a^2} + (1-\alpha)(\bar{r}/b)^2 e^{-\bar{r}_j^2/b^2} \right] \left(r_j^2 - r_{j-1}^2 \right) \right\}}, \tag{2.75}$$

where we have defined $\bar{S}$ by

$$\bar{S} r_J^2 = \sum_{j=1}^{J} S_j \left(r_j^2 - r_{j-1}^2 \right). \tag{2.76}$$

The values of a, b, α, and $\bar{S}$ for cases A–D are in Table 2.4. In these cases, the radial distribution of the mass sink is changed by altering $\alpha = 1, 0.8, 0.5, 0.2$. Plots of S_j are shown in Fig. 2.12 for the different values of α. From this figure, we can see that while the area-averaged mass sink is the same, the radial distributions are different. Figure 2.13 shows $v_{\max}(t)$ and $r_{\max}(t)$ for cases A–D from Table 2.4. While the initial $r_{\max}$ values between the four cases span 300 km, the intensification and contraction are similar during the first 24 h, features that are similar to the two- and three-region model results. Case A shows intensification that is unimpeded due to the largest mass sink value being located in the innermost regions. This case most resembles the output from the two-region model shown in Fig. 2.5. The other cases have more subdued intensification rates due to the mass sink being shifted radially outward as shown by the black curves that represent contours of equal physical time ($t = 24, 72, 120, 168, 216$ h) in Fig. 2.5. On the opposite end of the spectrum, case D shows a vortex with a large initial $r_{\max}$ and a long incubation time. The mass sink distribution associated with this case causes the vortex to struggle to contract and intensify. In some respects, case D is similar to the three-region model case shown in Fig. 2.10. From cases A→D, we see the formation of hollow potential vorticity towers resulting from the radial shift outward of the mass sink. At all times, case D has a larger eye than case A. However, this does not tell us anything about the overall structure or damage potential of the tropical cyclone.

2.5.2 $\mathcal{E} - V_{\max}$ *diagrams for the multi-region model*

Intensity is only one metric for characterizing the strength and damage potential of a tropical cyclone. Many of the impacts related to tropical cyclones stem from the size of the tropical cyclone. To communicate these hazards and understand the dynamical differences between small and large storms, size metrics for tropical cyclones are needed (e.g., the radii of 17 m s^{-1} wind in intercardinal quadrants). A number of climatological studies have attempted to develop other metrics for the size of the tropical cycle using wind, potential vorticity, brightness temperature from geostationary satellites,

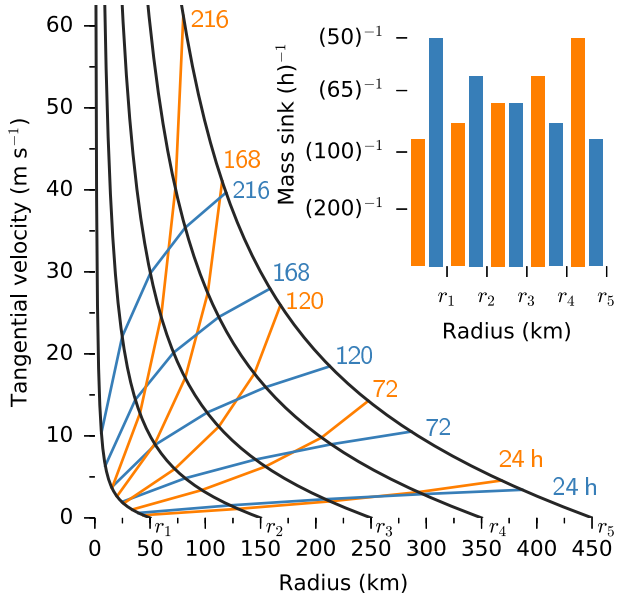

FIG. 2.11. A plot for a six-region example from the multi-region forced, balanced model. The black lines represent the absolute angular momentum surfaces on a (υ, r) plane bounding the regions. The orange and blue curves show $\upsilon(r)$ at $t = 24, 72, 120, 168, 216$ h for the constant mass sink displayed in the inset. The inset figure shows the radial distribution of the mass sink between the absolute angular momentum surfaces for the two vortices. Longer bars represent a weaker mass sink. Note that this is the inverse of the presentation used for the sink in Fig. 2.12.

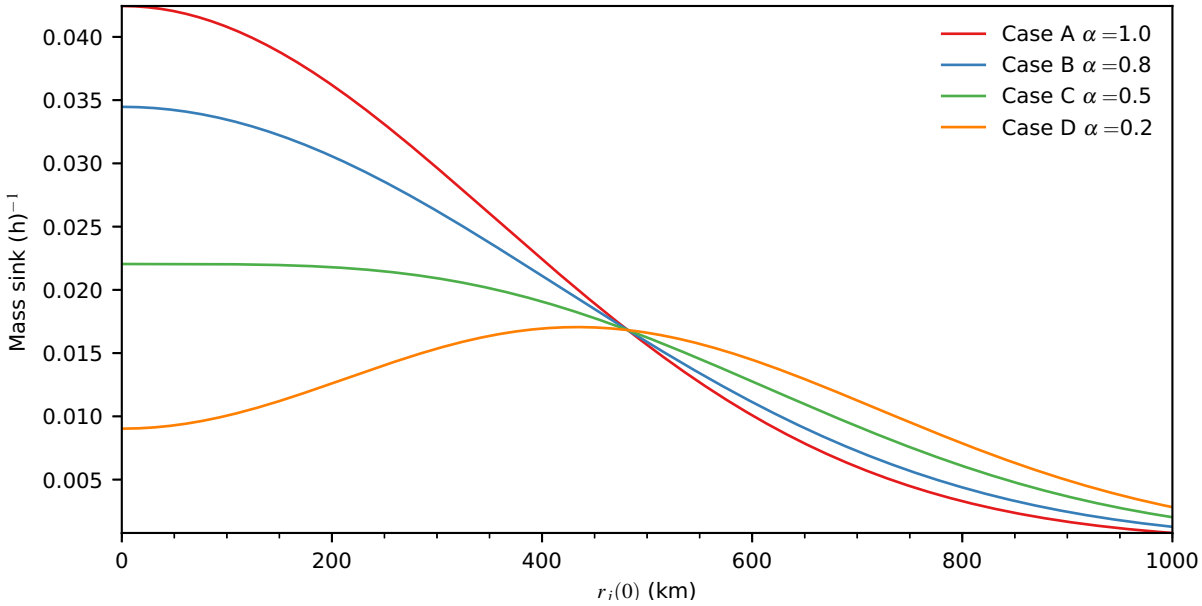

FIG. 2.12. S_j on the domain $j = 1, 2, \cdots, J$ for the values of $\alpha = 1, 0.8, 0.5, 0.2$ for cases A–D and constant values of a, b, and $\bar{S}$, which can be found in Table 2.4. The distribution of the mass sink shifts radially outward with decreasing α.

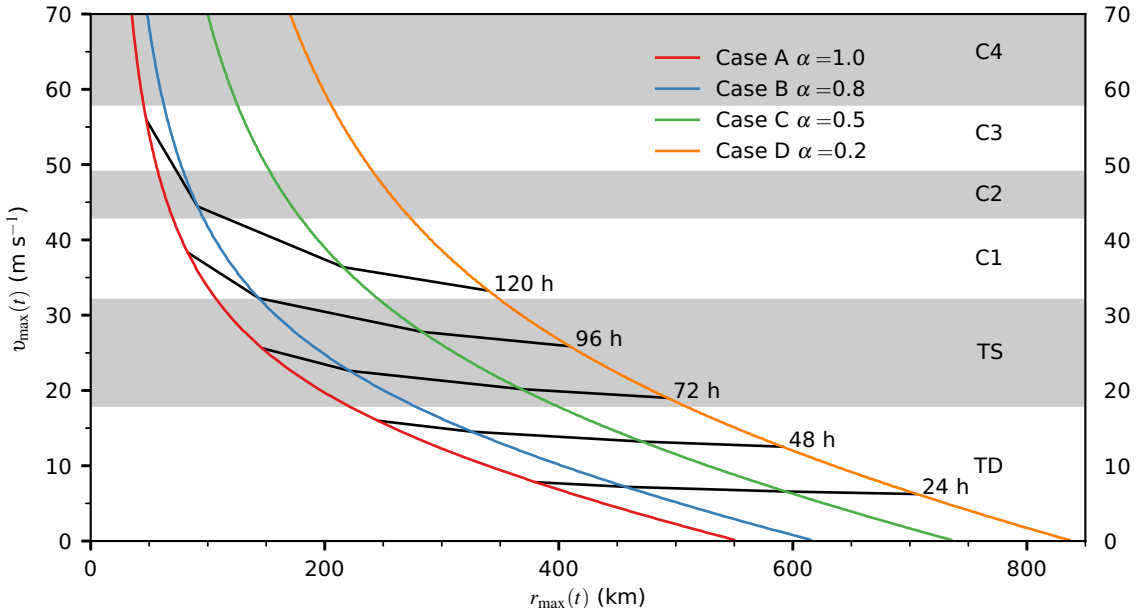

FIG. 2.13. $\upsilon_{\max}(t)$ and $r_{\max}(t)$ for cases A–D with values of a, b, α, and $\bar{S}$ that can be found in Table 2.4. Labels on the right stand for tropical depression (TD), tropical storm (TS), and Category 1–4 hurricanes. Along the five thin black lines, the physical time for $t = 24, 48, 72, 96, 120$ h.

TABLE 2.4. Cases A–D for the multi-region model. The values $a, b, \alpha, \bar{S}$ are specified constants that in conjunction with (2.111) control the radial distribution of the mass sink for each case. The maximum tangential wind $\upsilon_{\max}$, the deviation in fluid depth $\bar{h} - h(0,t)$, and total energy $\mathcal{E}$ are provided for $t = 120$ h.

Case	α	a (km)	b (km)	$\bar{S}$	$\upsilon_{\max}$ (m s^{-1})	$\bar{h} - h(0,t)$ (m)	$\mathcal{E}$ (10^{18} J)
A	1.0	500	500	(96 h)$^{-1}$	55.9	1265	1.78
B	0.8	500	500	(96 h)$^{-1}$	44.4	850	2.01
C	0.5	500	500	(96 h)$^{-1}$	36.4	562	2.32
D	0.2	500	500	(96 h)$^{-1}$	33.3	426	2.47

and area-integrated kinetic energy (Merrill 1984; Liu and Chan 1999; Kimball and Mulekar 2004; Knaff et al. 2007, 2014; Chan and Chan 2012, 2014, 2015). Viewing area-integrated kinetic energy as one of the better metrics to understand the destruction potential of a tropical cyclone, both Powell and Reinhold (2007) and Maclay et al. (2008) have proposed scales that involve two parameters — maximum wind speed and area-integrated kinetic energy calculated from aircraft reconnaissance data. In each of these works, the authors focus on the area-integrated kinetic energy only over the lower troposphere and only out to a limited radius (e.g., 200 km) due to the extent of radial penetrations from the observational dataset. While this is a practical limitation in their work, Ooyama (1969a) highlights the effect of limiting the radius to which the area-integrated kinetic energy is computed. From a model simulation

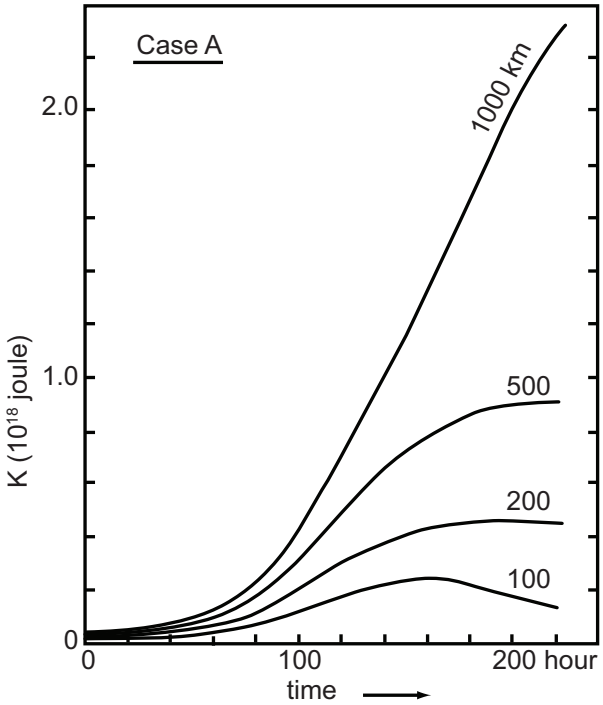

FIG. 2.14. Time evolution of the total kinetic energy for regions within radii of 100, 200, 500, and 1000 km. Reproduced from Fig. 10 of Ooyama (1969a). The figure shows that calculating the kinetic energy for radii ≤ 500 km missed the continued growth and expansion of the wind field even after the model reaches a quasi-steady state in the maximum tangential velocity.

by Ooyama (1969a), Fig. 2.14 shows that while the area-integrated kinetic energy will either level off or decrease when the calculation is done within an area of 500 km from the center of the vortex, the wind field in the far-field region continues to expand after the vortex reaches a quasi-steady state in its maximum intensity resulting in the continued increase of the integrated kinetic energy. Hill and Lackmann (2009) and Wang (2009) show that in the presence of adequate middle tropospheric moisture, the size of a tropical cyclone increases due to the diabatic heating associated with outer and spiral rainbands, an argument consistent with the inertial stability ideas that originate from work with the Eliassen (1951) balanced vortex model.

To understand more about the relationship between energy and the maximum tangential velocity and to see if the forced, balanced model based on the wave–vortex approximation adequately represents tropical cyclones in terms of $\mathcal{E}$, we will present results from our model in the $\mathcal{E} - V_{\max}$ diagram space. Our results will be presented as total energy (i.e., kinetic plus available potential) and will be

computed over the entire domain, which is akin to Ooyama (1969a). To compute the total energy, we begin with the invertibility principle (2.64) in the form

$$\frac{g^2\bar{h}}{P_j^2}\frac{\partial}{r\,\partial r}\left(r\frac{\partial h}{\partial r}\right)-g(h-\bar{h})=g\bar{h}\left(1-e^{-\tau_j}\right)\quad\text{for}\quad r_{j-1}(t)<r<r_j(t),\tag{2.77}$$

where $j=1,2,\cdots,J,J+1$. For the innermost region ($j=1$), the value of r_0 is taken to be zero. For the far-field region ($j=J+1$), the outer radius r_{J+1} is taken to be infinity, P_{J+1} is taken to be f, and τ_{J+1} is taken to be zero (i.e., no forcing in the far-field region). We now multiply (2.77) by $(h-\bar{h})$ and integrate to obtain

$$\int_{r_{j-1}(t)}^{r_j(t)}\tfrac{1}{2}\left[v^2\bar{h}+g(h-\bar{h})^2\right]r\,dr=\tfrac{1}{2}g\bar{h}\left\{\left[\frac{(h-\bar{h})rv}{P_j}\right]_{r_{j-1}}^{r_j}+\left(1-e^{-\tau_j}\right)\int_{r_{j-1}(t)}^{r_j(t)}(h-\bar{h})r\,dr\right\},\tag{2.78}$$

where the boundary terms have originated from an integration by parts and we have made use of the balance relation (2.16). Taking the sum of (2.78) from $j=1$ to $j=J+1$ yields

$$\mathcal{E}=\int_0^\infty\tfrac{1}{2}\left[v^2\bar{h}+g(h-\bar{h})^2\right]r\,dr=\tfrac{1}{2}g\bar{h}\sum_{j=1}^{J+1}\left\{\left[\frac{(h-\bar{h})rv}{P_j}\right]_{r_{j-1}}^{r_j}+\left(1-e^{-\tau_j}\right)\int_{r_{j-1}(t)}^{r_j(t)}(h-\bar{h})r\,dr\right\}.\tag{2.79}$$

The sum on the right-hand side of (2.79) can be written

$$\sum_{j=1}^{J+1}\left[\frac{(h-\bar{h})rv}{P_j}\right]_{r_{j-1}}^{r_j}=\sum_{j=1}^{J}\left(h_j-\bar{h}\right)r_jv_j\left(\frac{1}{P_j}-\frac{1}{P_{j+1}}\right)=\sum_{j=1}^{J}\left(h_j-\bar{h}\right)\left(e^{-\tau_j}-e^{-\tau_{j+1}}\right)\tfrac{1}{2}\left(R_j^2-r_j^2\right).\tag{2.80}$$

The volume deficit integral on the right-hand side of (2.79) can be evaluated using the solution (2.66). The result is

$$\int_{r_{j-1}(t)}^{r_j(t)}(h-\bar{h})r\,dr=\tfrac{1}{2}\bar{h}\left[r_j^2-r_{j-1}^2-(R_j^2-R_{j-1}^2)e^{-\tau_j}\right]\quad\text{for}\quad 1\le j\le J.\tag{2.81}$$

Using (2.80) and (2.81) in (2.79), we can write the total energy $\mathcal{E}$ as

$$\mathcal{E}=\tfrac{1}{4}g\bar{h}\sum_{j=1}^{J}\left\{\left(h_j-\bar{h}\right)\left(e^{-\tau_j}-e^{-\tau_{j+1}}\right)\left(R_j^2-r_j^2\right)+\bar{h}\left(1-e^{-\tau_j}\right)\left[r_j^2-r_{j-1}^2-\left(R_j^2-R_{j-1}^2\right)e^{-\tau_j}\right]\right\}.\tag{2.82}$$

Returning to the cases from Table 2.4, Fig. 2.15 shows the maximum tangential velocity $v_{\max}$, deviation in fluid depth at $r=0$, $\bar{h}-h(0,t)$, and total energy $\mathcal{E}$ during the first 120 h from a resting initial state. Panels a) and b) show that $v_{\max}$ and $\bar{h}-h(0,t)$ are largest for case A, the case with unimpeded intensification. However, panel c) shows that case D has a larger integrated total energy $\mathcal{E}$ than the

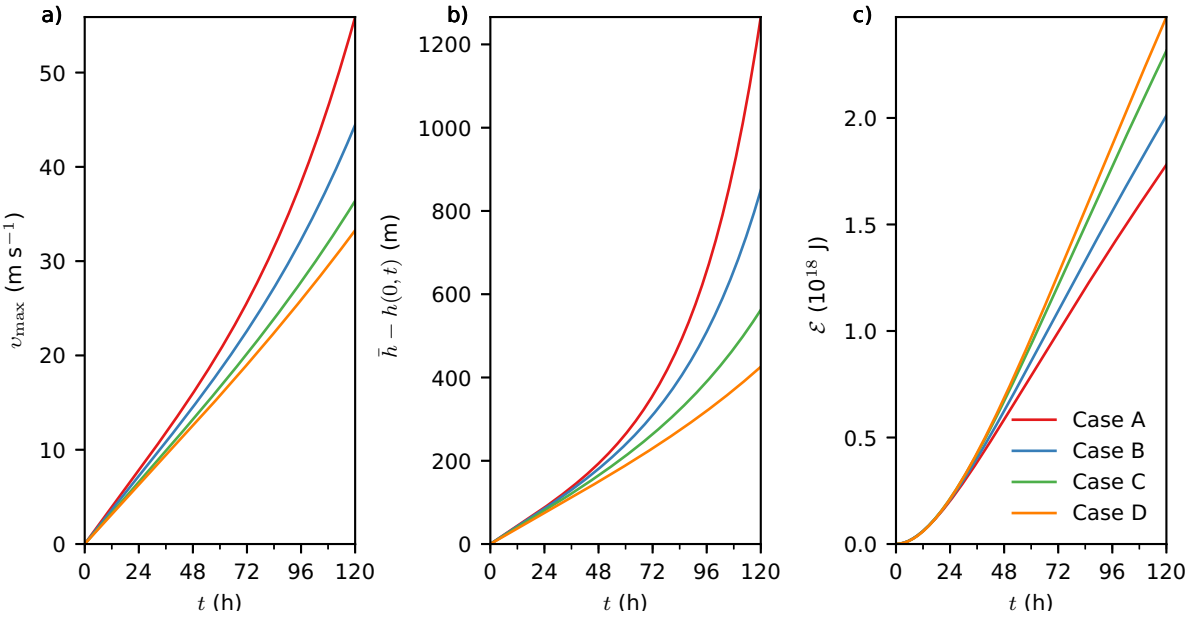

FIG. 2.15. a) maximum tangential wind $v_{max}(t)$ (m s^{-1}), b) deviation in fluid depth $\bar{h}-h(0,t)$ (m), and c) total energy $\mathcal{E}(t)$ (10^{18} J) in the region $0 \leq r \leq 1000$ km from $t = 0$ to 120 h for the cases A–D with values of a, b, α, and $\bar{S}$ that can be found in Table 2.4.

other three cases, i.e., a larger wind field in response to the mass sink at larger radii. In the $\mathcal{E} - V_{max}$ space, Fig. 2.16 shows that by the time the vortices reach category 1 strength on the Saffir-Simpson wind scale, the integrated total energy $\mathcal{E}$ for case D is already over twice the energy contained in case A. Also, Fig. 2.16 indicates that vortices with a mass sink displaced from the center will continue to expand as they intensify where cases saturate from an integrated total energy $\mathcal{E}$ standpoint, e.g., case A where the mass sink is concentrated in the center. This suggests that storms that struggle to intensify are still capable of becoming larger and are possibly capable of more damage than more intense storms if ample diabatic heating is present outside of the radius of maximum wind. This result is consistent with the inertial stability ideas presented by Vigh and Schubert (2009) and Musgrave et al. (2012) as well as the humidity arguments made by Hill and Lackmann (2009) and Wang (2009).

Eyewall replacement is a mechanism by which storms can change the distribution of the regions with the largest diabatic heating from close to the core to outside of the original radius of maximum wind. We can use the multi-region model to assess how much the total energy $\mathcal{E}$ changes during eyewall replacement. Observational work indicates that there should be a jump in kinetic energy (e.g., Maclay et al. 2008; Sitkowski et al. 2011). Through a modeling study of eyewall replacement, Rozoff et al. (2012) found a 79% increase in kinetic energy during the cycle. Figure 2.17 offers a schematic view of how intensity and integrated kinetic energy change before, during, and after eyewall replacement should

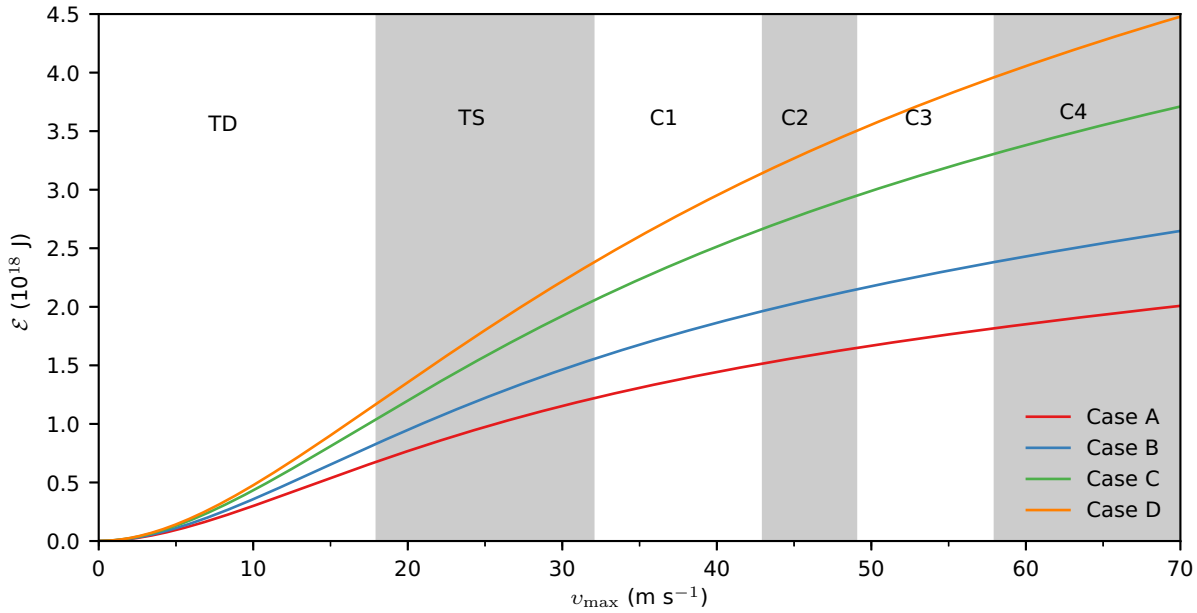

FIG. 2.16. Total energy $\mathcal{E}$ versus maximum tangential wind (v_{max}) for four cases in the multi-region model configured using the constants from Table 2.4.

appear in the $\mathcal{E} - V_{max}$ diagram phase space. In Figs. 2.9 and 2.10, we see a three-region model case in which the absolute angular momentum surface associated with the radius of maximum wind changes. Rather than starting with a vortex in a resting state, we start with $\tau_{j,0} = 3$ in (2.62) for the region $0 \leq R \leq 300$ km. This configuration is the $r_{10} = 300$ km case from the two-region model in section 2.3 . For the $r_{10} = 300$ km case, $v_{max} = 31.7$ m s^{-1} and $r_{max} = 67.5$ km when $\tau = S_1 t = 3$. Next, we select values for the constant parameters in the mass sink (2.74), $\alpha = 0.1$, $a = b = 500$ km, and $\bar{S} = (96 \text{ h})^{-1}$. Figure 2.18 shows the evolution of the vortex in the $\mathcal{E} - V_{max}$ space. The figure shows that development of the vortex is not smooth. The $r_{10} = 300$ km case from the two-region model produces a structure akin to a modified Rankine vortex that does not have a large amount of energy associated with it. Initially, we see that the inner eyewall continues to intensify because of the small, nonzero mass sink present in the inner core due to $\alpha = 0.1$. But, the outer eyewall quickly develops and switches the vortex from being energy growth dominated to intensity growth dominated. Once the outer eyewall dominates (e.g., replacing the inner) in the $\mathcal{E} - V_{max}$ space, the vortex exhibits the same progression as the resting cases in Fig. 2.16. After eyewall replacement, the new eyewall often gets "stuck," in that it does not contract to the radius of the original eyewall. The evolution seen in Figs. 2.16 and 2.18 may suggest that the eyewall can only contract radially inward as far as its mass sink will allow unless something, such as boundary layer processes, allow it to contract further.

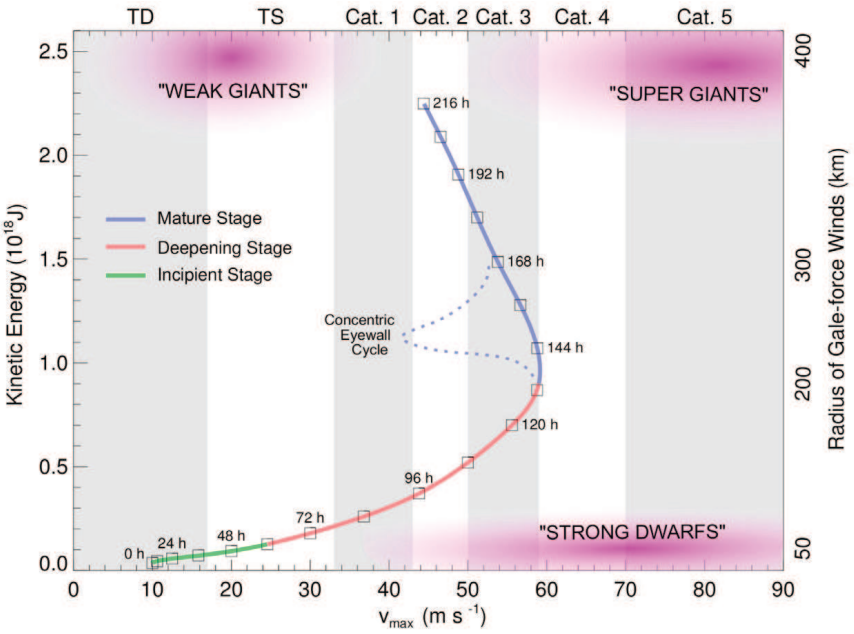

FIG. 2.17. A kinetic energy versus maximum wind speed ($V_{\max}$) schematic that shows the evolution of a vortex from the "incipient," "deepening," and "mature" stages of a tropical cyclone (e.g., "genesis," "rapid intensification," and "quasi-steady state" stages). The dashed portion in the mature stage is indicative of the behavior of a tropical storm undergoing eyewall replacement. Time is indicated in 12-h increments from 0 to 216 h along the multi-colored curve, Saffir–Simpson categories are indicated across the top of the diagram, and the labels "weak giants," "super giants," and "strong dwarfs" are offered to provide context for the phase space. Figure 3 from Musgrave et al. (2012).

In these experiments, we artificially constructed a jump through changing the radial distribution of the mass sink to a larger radius to see the total energy $\mathcal{E}$ response. In real tropical cyclones or in a model that includes boundary layer processes, the diabatic heating would evolve in unison with the rest of the vortex. In this case, the value of α controls the jump in total energy during our eyewall replacement simulation. Smaller values of α produce larger jumps in the total energy. In Fig. 2.18, we see that the jump is much larger than the one shown by Rozoff et al. (2012) due in part to our choice of initial vortex via $\tau_{j,0}$ and α. Because the multi-region model does not have a means by which to weaken the inner eyewall as the outer develops, the development in the $\mathcal{E}-V_{\max}$ space is not as clear as what is presented in the schematic shown in Fig. 2.17. However, Fig. 2.18 shows the energy jump is displacing the mass sink further from the center of the vortex. In reality, this change would be the result of boundary layer processes controlling the location of the frictionally induced convergence and Ekman pumping.

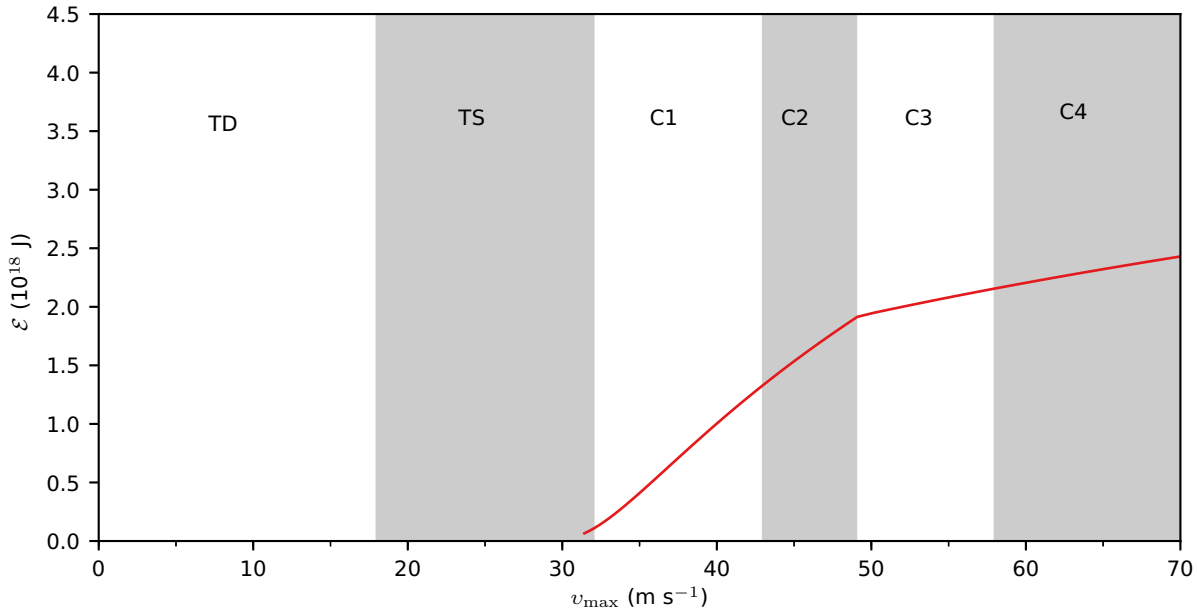

FIG. 2.18. Total energy $\mathcal{E}$ versus maximum tangential wind $V_{\max}$ for an eyewall replacement case in the multi-region model. This example starts from a nonresting state, $\tau_{j,0} = 3$ for $0 \le R \le 300$ km, and the mass sink constants for (2.74) are $\alpha = 0.1$, $a = b = 500$ km, and $\bar{S} = (96\text{ h})^{-1}$.

2.6 A COMPARISON OF TWO BALANCED VORTEX MODELS OF TROPICAL CYCLONE INTENSIFICATION

In the previous sections, we developed analytic, time-dependent solutions of an inviscid, axisymmetric, one-layer, balanced vortex model based on the wave–vortex approximation proposed by Salmon (2014). This model is similar to Eliassen (1951) except that we made a slight modification to the gradient balance approximation. These analytic solutions provide insight into the relationship between intensity and size, and the radial movement of the radius of maximum wind relative to contracting angular momentum surfaces. The consequence of making the wave–vortex approximation is that it is only valid when the Froude number is small. The Eliassen (1951) balanced vortex model should be regarded as the more general of the two models because it does not have the small Froude number restriction. In our two-, three-, and multi-region models, we assumed a forced, balanced model that is based on the wave–vortex approximation would be valid for vertical profiles of diabatic heating projected onto the external mode, i.e., $c \approx 250 - 300$ m s^{-1}. In this section, we will compare the model based on the wave–vortex approximation, BV2, to a model based on the gradient balanced approximation, BV1, to show how the wave–vortex approximation breaks down. To make this comparison, we will solve for both models in r space numerically through using an iterative procedure until the respective solutions converge.

2.6.1 *The gradient balanced vortex model (BV1)*

The governing equations for the inviscid, axisymmetric, one-layer, forced, gradient balanced vortex model are

$$\left(f+\frac{v}{r}\right)v=g\frac{\partial h}{\partial r}, \tag{2.83}$$

$$\frac{\partial v}{\partial t}+(f+\zeta)u=0, \tag{2.84}$$

$$\frac{\partial h}{\partial t}+\frac{\partial(ruh)}{r\,\partial r}=-hS, \tag{2.85}$$

where u is the radial wind, v is the tangential wind, h is the depth of the fluid, g is the acceleration of gravity, f is the constant Coriolis parameter, $\zeta=\partial(rv)/r\,\partial r$ is the relative vorticity, and S is the mass sink. The equations represented by (2.83)–(2.85) are referred to as BV1, which is the forced, shallow water version of the classic Eliassen (1951) balanced vortex model.

The energy principle for BV1 is obtained by taking the sum of $-hu$ times (2.83), hv times (2.84), and $g(h-\bar{h})$ times (2.85), where $\bar{h}$ is the depth of the fluid to which $h(r,t)$ asymptotes as $r\to\infty$. After integrating over the entire area, we obtain

$$\frac{d(\mathcal{K}+\mathcal{P})}{dt}=\mathcal{G}, \tag{2.86}$$

where

$$\mathcal{K}=\int_0^\infty \tfrac{1}{2}v^2hr\,dr,\quad \mathcal{P}=\int_0^\infty \tfrac{1}{2}g(h-\bar{h})^2r\,dr,\text{ and }\quad \mathcal{G}=\int_0^\infty g(\bar{h}-h)hSr\,dr, \tag{2.87}$$

are the kinetic energy $\mathcal{K}$, the available potential energy $\mathcal{P}$, and the total energy generation $\mathcal{G}$.

The absolute angular momentum principle, obtained from (2.84), is

$$\frac{D}{Dt}\left(rv+\tfrac{1}{2}fr^2\right)=0, \tag{2.88}$$

where the material derivative (D/Dt) is $(\partial/\partial t)+u(\partial/\partial r)$. Using (2.84), the vorticity equation is written as

$$\frac{D(f+\zeta)}{Dt}+(f+\zeta)\frac{\partial(ru)}{r\,\partial r}=0, \tag{2.89}$$

and the continuity equation (2.85) takes the form

$$\frac{Dh}{Dt}+h\frac{\partial(ru)}{r\,\partial r}=-hS. \tag{2.90}$$

Elimination of the divergence between (2.89) and (2.90) leads to the potential vorticity principle

$$\frac{DP}{Dt} = SP, \tag{2.91}$$

where $P = (f+\zeta)(\bar{h}/h)$ is the potential vorticity.

Returning to our definition of potential radius $\frac{1}{2}fR^2 = rv + \frac{1}{2}fr^2$, we rewrite the absolute angular momentum principle (2.88) as $\dot{R} = DR/Dt = 0$. As outlined by Schubert and Hack (1983), we now write the material derivative in (R,T) space as $(D/Dt) = (\partial/\partial T) + \dot{R}(\partial/\partial R) = (\partial/\partial T)$, where $T = t$, but $\partial/\partial T$ implies fixed R, while $\partial/\partial t$ implies fixed r. We now write (2.91) as

$$\frac{\partial P}{\partial T} = SP. \tag{2.92}$$

Equation (2.91) indicates that the evolution of potential vorticity involves both the radial advection and generation by a mass sink in the r coordinate. However, in the R coordinate, the evolution of potential vorticity only involves the mass sink as can be seen by inspecting (2.92). In (2.92), the radial advection has become implicit in the coordinate transformation. For a mass sink dependent on both R and T, the solution of (2.92) is

$$P(R,T) = f\,e^{\tau(R,T)} \quad \text{where} \quad \tau(R,T) = \tau_0(R) + \int_0^T S(R,T')\,dT', \tag{2.93}$$

where specification of $\tau_0(R)$ is equivalent to specification of the initial potential vorticity through the relation $P(R,0) = f\,e^{\tau_0(R)}$. The choice $\tau_0(R) = 0$ corresponds to the initial condition $P(R,0) = f$ (a resting initial state).

Now, we need to consider how to recover the mass and wind fields from the $P(R,T)$ solution given by (2.93). This involves solving a second order differential equation that we can formulate in terms of either $v(r)$ or $h(r)$. In this work, we will only discuss the v formulation. Next, we combine the gradient balance relation (2.83) with the radial derivative of the definition of potential vorticity to obtain the second order differential equation for v. From here, we can write the invertibility principle for $v(r)$, $R(r)$, and $h(r)$ as

$$r^2\frac{\partial^2 v}{\partial r^2} + r\frac{\partial v}{\partial r} - \left(1 + \frac{fP(r^2+R^2)}{2g\bar{h}}\right)v = r^2\frac{h}{\bar{h}}\frac{\partial P}{\partial r}, \tag{2.94}$$

with the boundary conditions

$$v = 0 \text{ at } r = 0 \quad \text{and} \quad v \sim K_1(\mu r) \text{ as } r \to \infty, \tag{2.95}$$

and with

$$R(r) = r\left(1 + \frac{2\upsilon}{fr}\right)^{1/2} \quad \text{and} \quad \frac{h(r)}{\bar{h}} = \frac{fR}{Pr}\frac{\partial R}{\partial r}, \tag{2.96}$$

where the inverse Rossby length in the far-field region is defined by $\mu = f/(g\bar{h})^{1/2}$. The outer boundary condition in (2.95) is obtained by noting that we assume $P \to f$, $(\partial P/\partial r) \to 0$, and $R \to r$ as $r \to \infty$, so that (2.94) reduces to the homogeneous, modified Bessel equation. The solution then consists of a linear combination of the growing, order one modified Bessel function of the first kind $I_1(\mu r)$ and the decaying, order one modified Bessel function of the second kind $K_1(\mu r)$ as shown in Fig. 2.4. Then, by requiring that the far-field region solution be proportional to the decaying solution $K_1(\mu r)$, we obtain the boundary condition given in (2.95). We obtain the two entries in (2.96) from the definitions of potential radius and potential vorticity.

At any given point in time t, (2.94)–(2.96) are a coupled, nonlinear system of equations with the unknowns $\upsilon(r)$, $R(r)$, and $h(r)$. An interesting aspect of this formulation of the nonlinear problem is that for any given t, we know the values of $P(R)$ from the analytic solution (2.93). However, we do not know the potential vorticity in physical space $P(r)$, which is required on both the left- and right-hand sides of the invertibility principle (2.94). To translate the known $P(R)$ into $P(r)$, we need to know the mapping $R(r)$, which is one of the unknowns in the system (2.94)–(2.96). In order to solve this system, we will envision the following iterative procedure. At a given point in time t, we assume we have some estimate for the values of mapping $R(r)$ and height in physical space $h(r)$, so that we also have an estimate for the current values of $P(r)$. Using these values, we solve (2.94)–(2.95) for $\upsilon(r)$. Next, we update our estimates for the values of $R(r)$ and $h(r)$. In repeating these steps until we reach convergence, we will know the mapping of $R(r)$ and therefore know the physical space potential vorticity distribution $P(r)$ in addition to the balanced mass and wind fields $h(r)$ and $\upsilon(r)$. Because of (2.93), we can perform this proposed procedure at any time t without knowledge of the solution at previous times. In other terms, the determination of the mapping $R(r)$ at time t is equivalent to finding the accumulated effects of radial advection on the potential vorticity distribution.

Taking the envisioned procedure proposed above, we consider the spatial discretization method and iterative solution procedure for the nonlinear system (2.94)–(2.96), which will be solved numerically on a uniform radial grid defined by $r_j = j\Delta r$ for $j = 0, 1, \cdots, J-1, J$. For the results presented here, we have chosen the grid spacing $\Delta r = 100$ m and $J = 10000$, corresponding to a computational domain

size of 1000 km. Using second order accurate, centered finite differences, (2.94)–(2.96) are discretized in the form

$$\left(1-\frac{\Delta r}{2r_j}\right)v_{j-1}^{(\nu+1)}-\left(2+\frac{(\Delta r)^2}{r_j^2}+\frac{fP_j^{(\nu)}(\Delta r)^2\left(r_j^2+R_j^{2(\nu)}\right)}{2g\bar{h}r_j^2}\right)v_j^{(\nu+1)}+\left(1+\frac{\Delta r}{2r_j}\right)v_{j+1}^{(\nu+1)}=\frac{h_j\left(P_{j+1}^{(\nu)}-P_{j-1}^{(\nu)}\right)\Delta r}{2\bar{h}}, \tag{2.97}$$

with the boundary conditions

$$v_0=0 \quad \text{and} \quad v_J^{(\nu+1)}=\left(\frac{K_1(\mu r_J)}{K_1(\mu r_{J-1})}\right)v_{J-1}^{(\nu+1)}, \tag{2.98}$$

and with the values of R_j and h_j updated by

$$R_j^{(\nu+1)}=r_j\left(1+\frac{2v_j^{(\nu+1)}}{fr_j}\right)^{1/2} \qquad \text{and} \qquad \frac{h_j}{\bar{h}}=\frac{fR_j^{(\nu+1)}\left(R_{j+1}^{(\nu+1)}-R_{j-1}^{(\nu+1)}\right)}{2r_jP_j^{(\nu+1)}(\Delta r)}, \tag{2.99}$$

where (2.97) applies for $j=1,2,\cdots,J-1$. The discrete outer boundary condition has been obtained by noting that, at the outer two grid points, the asymptotic behavior of v requires that $v_J/v_{J-1}=K_1(\mu r_J)/K_1(\mu r_{J-1})$, since the constant of proportionality cancels out. This boundary condition, listed as the second entry in (2.98), relates the last two values of v on the grid. At a given time t, knowing $P(R)$, we now regard (2.97)–(2.99) as a coupled system in v_j, R_j, and h_j. Equations (2.97) and (2.98) form a tridiagonal algebraic system. Assuming that we have current estimates of R_j and h_j as well as an estimate of P_j, we can regard this tridiagonal system as linear and solve for v. We then update our estimates of R_j and h_j using (2.99) to repeat the process. Only after convergence of this iterative process do we know the mapping R_j and physical space distribution of potential vorticity P_j.

2.6.2 The second balanced vortex model (BV2)

The second balanced vortex model is based on the wave–vortex approximation introduced by Salmon (2014), with two additional assumptions involving axisymmetry and the filtering of inertia-gravity waves (Schubert et al. 2016). The governing equations for the BV2 system are

$$Pv=g\frac{\partial h}{\partial r}, \tag{2.100}$$

$$\frac{\partial v}{\partial t}+(f+\zeta)u=0, \tag{2.101}$$

$$\frac{\partial h}{\partial t}+\frac{\partial(ruh)}{r\,\partial r}=-hS. \tag{2.102}$$

Because of how we have chosen to identify the variables (see Schubert et al. 2016), the difference between BV1 and BV2 lies in the balance relations (2.83) and (2.100). Since (2.101) is identical to (2.84)

and (2.102) is identical to (2.85), the analysis done between (2.88) and (2.93) remains the same. The difference lies in the invertibility principle.

As with BV1, we will write the energy principle for BV2 by taking the sum of $-h\,u$ times (2.100), $\bar{h}\,v$ times (2.101), and $g(h-\bar{h})$ times (2.102), and integrate over the entire area. The result for BV2 is

$$\frac{d(\mathcal{K}+\mathcal{P})}{d\,t}=\mathcal{G}, \tag{2.103}$$

where

$$\mathcal{K}=\int_0^\infty \tfrac{1}{2}v^2\bar{h}\,r\,d\,r,\quad \mathcal{P}=\int_0^\infty \tfrac{1}{2}g(h-\bar{h})^2\,r\,d\,r, \text{ and } \quad \mathcal{G}=\int_0^\infty g(\bar{h}-h)hSr\,d\,r, \tag{2.104}$$

are the kinetic energy $\mathcal{K}$, the available potential energy $\mathcal{P}$, and the total energy generation $\mathcal{G}$ in BV2. Note that the energy principles for BV1 and BV2 are identical except for the definition of $\mathcal{K}$. In BV2, the kinetic energy of the fluid column is $\frac{1}{2}v^2\bar{h}$, which is a good approximation of $\frac{1}{2}v^2h$ for situations in which the deviations in the depth of the fluid are small compared to $\bar{h}$.

For BV2, the problem of recovering the wind and mass fields from the $P(R,T)$ solution given by (2.93) is nearly identical to BV1. The second order differential equation for v is now obtained by combining the balance relation (2.100) with the radial derivative of the definition of potential vorticity. Then, the BV2 invertibility principle for $v(r)$, $R(r)$, and $h(r)$ can be written as

$$r^2\frac{\partial^2 v}{\partial r^2}+r\frac{\partial v}{\partial r}-\left(1+\frac{P^2}{g\bar{h}}r^2\right)v=r^2\frac{h}{\bar{h}}\frac{\partial P}{\partial r}, \tag{2.105}$$

with the boundary conditions

$$v=0 \text{ at } r=0 \quad \text{and} \quad v\sim K_1(\mu r) \text{ as } r\to\infty, \tag{2.106}$$

and with

$$R(r)=r\left(1+\frac{2v}{fr}\right)^{1/2} \quad \text{and} \quad \frac{h(r)}{\bar{h}}=\frac{fR}{Pr}\frac{\partial R}{\partial r}. \tag{2.107}$$

Again, as with BV1, knowing $P(R)$ at any given time t, we regard (2.105)–(2.107) as a coupled system in $v(r)$, $R(r)$, and $h(r)$. The BV2 invertibility (2.105)–(2.107) is identical to the BV1 invertibility (2.94)–(2.96) except for the coefficients in the v terms in (2.105) and (2.94). The result of the discretization of BV2 yields

$$\left(1-\frac{\Delta r}{2r_j}\right)v_{j-1}^{(\nu+1)}-\left(2+\frac{(\Delta r)^2}{r_j^2}+\frac{P_j^{2(\nu)}(\Delta r)^2}{g\bar{h}}\right)v_j^{(\nu+1)}+\left(1+\frac{\Delta r}{2r_j}\right)v_{j+1}^{(\nu+1)}=\frac{h_j\left(P_{j+1}^{(\nu)}-P_{j-1}^{(\nu)}\right)\Delta r}{2\bar{h}}, \tag{2.108}$$

with the boundary conditions

$$\upsilon_0 = 0 \quad \text{and} \quad \upsilon_J^{(\nu+1)} = \left(\frac{K_1(\mu r_J)}{K_1(\mu r_{J-1})} \right) \upsilon_{J-1}^{(\nu+1)}, \tag{2.109}$$

and with the values of R_j and h_j updated by

$$R_j^{(\nu+1)} = r_j \left(1 + \frac{2\upsilon_j^{(\nu+1)}}{f r_j} \right)^{1/2} \qquad \text{and} \qquad \frac{h_j}{\bar{h}} = \frac{f R_j^{(\nu+1)} \left(R_{j+1}^{(\nu+1)} - R_{j-1}^{(\nu+1)} \right)}{2 r_j P_j^{(\nu+1)} (\Delta r)}, \tag{2.110}$$

where (2.108) applies for $j = 1, 2, \cdots, J-1$. The discrete form of BV2 (2.108)–(2.110) is nearly identical to the discrete form of BV1 (2.97)–(2.99) except along the diagonal elements of the tridiagonal systems (2.97) and (2.108).

2.6.3 Solutions of the forced, balanced models

The last two sections show that the balanced models BV1 and BV2 are nearly identical with the only difference being in the diagonal elements of the tridiagonal systems (2.97) and (2.108). In the remainder of this section, we present solutions of the forced, balanced models BV1 and BV2 for the purpose of comparing the two balance approximations. To make these comparisons, we will set $P(R, T)$ to be the same in both models. It should be noted that the two models will produce different $\upsilon(t)$, $h(r)$, and $R(r)$ fields because of the differences between the invertibility principle for each system. The implication of this difference is that the potential vorticity in physical space $P(r)$ between BV1 and BV2 will differ.

In this set of experiments, we specify the following radial distribution of the mass sink

$$S(R) = \frac{2\mathcal{M}}{\alpha a^2 + (1-\alpha) b^2} \left\{ \alpha \exp\left(-\frac{R^2}{a^2} \right) + (1-\alpha) \left(\frac{R^2}{b^2} \right) \exp\left(-\frac{R^2}{b^2} \right) \right\}, \tag{2.111}$$

where a, b, α, and $\mathcal{M}$ are specified constants. Taking (2.111) and multiplying by R, we can integrate by using $\int_0^\infty x e^{-x^2}\, dx = \frac{1}{2}$ and $\int_0^\infty x^3 e^{-x^2}\, dx = \frac{1}{2}$ to obtain

$$\mathcal{M} = \int_0^\infty S R\, dR = \int_0^\infty \left(1 + \frac{\zeta}{f} \right) S r\, dr. \tag{2.112}$$

If $\zeta = 0$ initially, the specified $\mathcal{M}$ can be interpreted as the area integrated initial mass sink. At later times, the area integrated mass sink $\int_0^\infty S r\, dr$ is smaller than $\mathcal{M}$ since $(\zeta/f) > 0$. In all the simulations presented here, the value of the integrated initial mass sink is chosen to be $\mathcal{M} = 3$ km^2 s^{-1}. Next, we specify the configurations for the experiments as shown in Table 2.5. In experiments A–D, $c = (g\bar{h})^{1/2} =$

TABLE 2.5. Parameters and output for BV1 and BV2 for cases A–D where mode is the typical vertical profile of diabatic heating projected onto the external mode (mode 0) and the first three internal modes (modes 1–3), c is the phase speed for the mode, $\bar{h}$ is the fluid depth and c/f is the Rossby length. The values of the maximum tangential wind $\upsilon_{\max,\mathrm{BV1}}$ and $\upsilon_{\max,\mathrm{BV2}}$ and the total energy $\mathcal{E}_{\mathrm{BV1}}$, and $\mathcal{E}_{\mathrm{BV2}}$ are computed from the model simulations at $t = 24$ h using the constant parameters $\alpha = 0.9$, $a = b = 300$ km, and $\mathcal{M} = 3$ km^2 s^{-1} used in (2.111) and $f = 5 \times 10^{-5}$ s^{-1}.

Case	Mode	$\bar{h}$ (m)	c (m s^{-1})	c/f (km)	$\upsilon_{\max,\mathrm{BV1}}$ (m s^{-1})	$\upsilon_{\max,\mathrm{BV2}}$ (m s^{-1})	$\mathcal{E}_{\mathrm{BV1}}$ (J)	$\mathcal{E}_{\mathrm{BV2}}$ (J)
A	0	6371	250	5000	38.4	38.2	1.85×10^{17}	1.86×10^{17}
B	1	367	60	1200	23.9	26.0	8.73×10^{15}	9.59×10^{15}
C	2	92	30	600	11.1	14.8	1.35×10^{15}	1.55×10^{15}
D	3	41	20	400	6.5	9.6	3.77×10^{14}	4.22×10^{14}

$250, 60, 30, 20$ m s^{-1}, which corresponds to the depth of the fluid as $\bar{h} = 6371, 367, 92, 41$ m. The choices for c are meant to represent typical vertical profiles of diabatic heating projected onto the external mode and the first three internal modes (Fulton and Schubert 1985) and will assist in testing when the two models diverge. The small Froude number restriction for the model based on the wave–vortex approximation is limited to flow speed $\upsilon \ll c$. Figure 2.19 shows the ratio of BV2 over BV1 for the maximum tangential velocity $\upsilon_{\max}$ and energetics — total energy $\mathcal{E}$, kinetic energy $\mathcal{K}$, and potential energy $\mathcal{P}$. For case A, we see that the ratio of BV2 over BV1 stays close to unity for $\upsilon_{\max}$, $\mathcal{E}$, and $\mathcal{K}$. Once $\upsilon_{\max}$ exceeds 110 m s^{-1}, a value not representative of tropical cyclones, we see a 1-2% difference in these quantities. There is a larger difference between $\mathcal{P}$ in the two models. However, $\mathcal{P}$ only represents a small contribution to the total energy. While the maximum tangential velocity in case B does not initially diverge, the energy immediately deviates between the two models for the first internal mode. This suggests that caution should be used for $c \approx 60$ m s^{-1}. The differences in the second and third internal mode, cases C and D, for all four quantities suggest that the wave–vortex approximation is unacceptable for flows with $c < 60$ m s^{-1}.

2.7 DISCUSSION

In this work, we explore the application of the wave–vortex approximation to the shallow water equations for tropical cyclones by developing a simple, one-layer, forced, balanced model for intensification. In the simulations, we develop analytic and numerical solutions to show the effects of piecewise mass sinks confined between absolute angular momentum surfaces. With this framework, we explore the effect of changing the radial extent of an area-averaged mass sink on the "incubation" time and intensification rate of vortices using a two-region analytic model with constant forcing. This model is

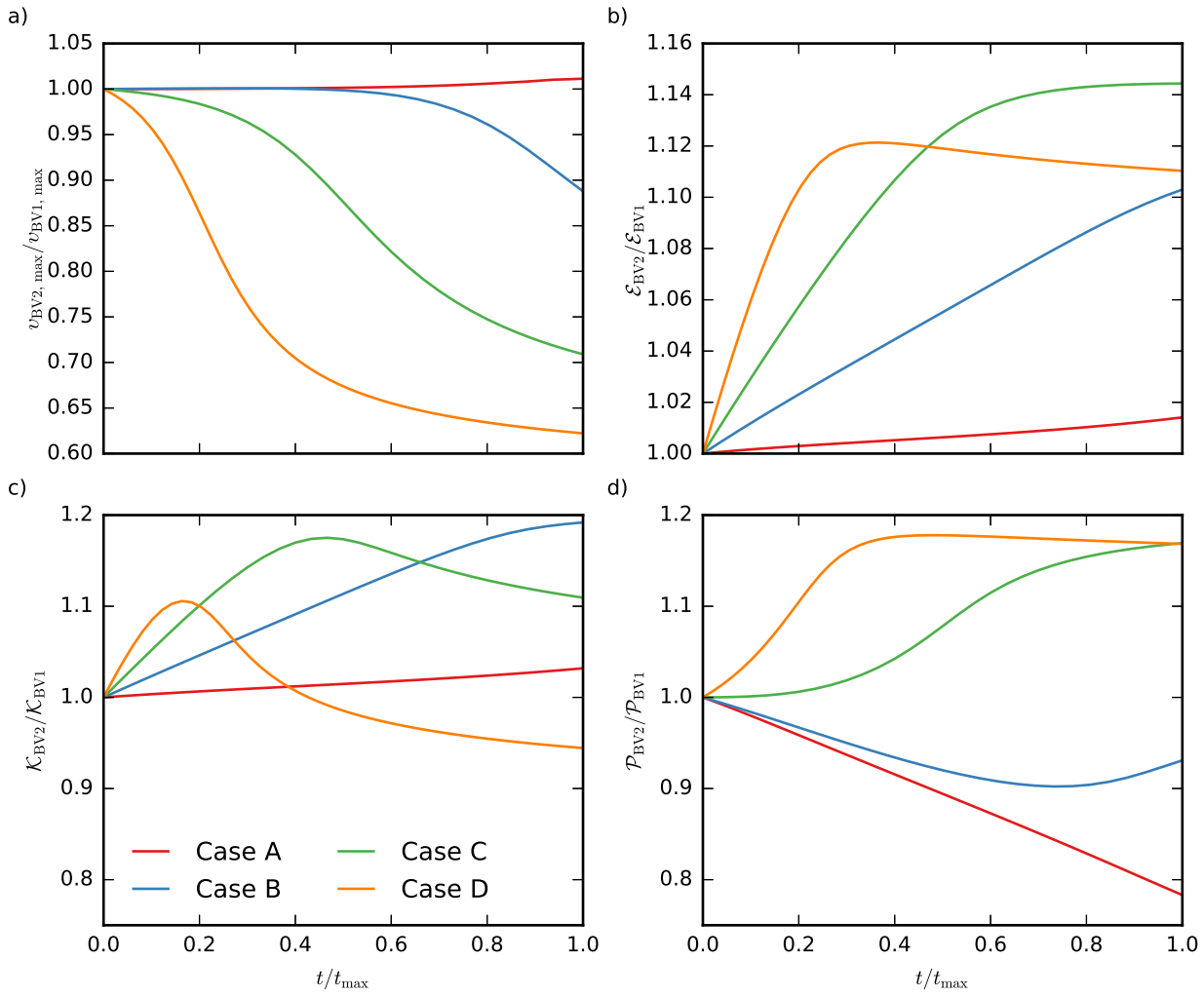

FIG. 2.19. The ratio BV2 over BV1 for a) maximum tangential velocity $v_{\max}$ b) total energy $\mathcal{E}$, c) kinetic energy $\mathcal{K}$ and d) potential energy $\mathcal{P}$. The cases A–D, shown in Table 2.5, are run until the iterative procedure fails to converge on a solution for the two tridiagonal systems for that case. This value is noted by $t_{\max}$.

sensitive to the radial extent of the area-averaged mass sink and bounding absolute angular momentum surface. The "incubation" time until rapid intensification of the vortex increases with larger values for the initial radius of this surface. The results also show that intensity is connected to the fraction of the initial fluid volume that must be removed before the potential vorticity monopole will develop in these cases.

Subsequently, the results from the two-region model are generalized to a three-region model, which we use to create a partition between regions that we designate as the core and the eyewall. This division between regions allows us to examine the formation and thinning of potential vorticity rings and assess

the relationship between absolute angular momentum surfaces and the radius of maximum tangential wind by examining the effects of a mass sink surrounding the nascent eye becoming larger than anywhere else. The annular region that is bounded by the two absolute angular momentum surfaces begins to contract radially inward and the annulus begins to shrink. The result is that the potential vorticity within the annular region grows faster than the inner region, developing a hollow potential vorticity tower and a 'U'-shaped tangential wind profile. While the work shown here is in an axisymmetric framework, the evolution of the results for later times can still be discussed. In this work, we show the development of thin rings of potential vorticity. In the axisymmetric framework, we see how these features develop a 'U'-shaped tangential wind profile. However, using the work of Schubert et al. (1999), we can assume that the thin rings of potential vorticity will allow for barotropic instability and a breakdown of this ring at a later time.

The mechanism shown here for generating a hollow potential vorticity tower based on the distribution of the mass sink is different than the production of this feature due to the frictional boundary layer (Smith and Vogl 2008; Kepert 2010a; Williams et al. 2013; Slocum et al. 2014). This frictional boundary layer mechanism involves the production of a shock-like structure through the nonlinear dynamics. Understanding the relative importance of these two mechanisms in real tropical cyclones remains a challenging problem. It is also hard to separate these two mechanisms from one another as the eyewall convection is tied to the region of maximized Ekman pumping (e.g., Ooyama 1969a,b, 1982; Raymond and Herman 2012; Kepert and Nolan 2014; Frisius and Lee 2016).

Next, we further generalize the model to one that can be run with multiple regions in the R space. In these results, we compare four different mass sink distributions with a constant value of $\bar{S}$. From these results, we see that the inward movement of absolute angular momentum surfaces can be impeded if the mass sink is low in the center of the vortex. However, a small amount of mass sink in the center of the vortex does not inhibit the ability of the wind field to expand. From assessing the model output in $\mathcal{E}-V_{\max}$ space, we see rapid expansion in the cases where the mass sink is further away from the center. In the eyewall replacement experiment, we see a jump in the total energy $\mathcal{E}$ while the outer eyewall continues to develop. Interestingly, once the outer eyewall overtakes the inner eyewall in intensity, the vortex develops as if the inner eyewall never existed, which suggests that an eye that gets "stuck" during replacement is simply continuing to evolve based on the current structure of the mass sink.

Finally, we compare the forced, balanced model based on the wave–vortex approximation to a model that uses the gradient balance relation. For the external mode, e.g., $c \approx 250$ m s^{-1}, the difference

between the maximum tangential velocity and the energetics is negligible. When $c \approx 60$ m s^{-1}, a value representative of the first internal mode, the differences in the maximum tangential velocity remain small for reasonable speed. However the energetics between the model quickly diverge. Simulations representative of the second and third internal mode show that the wave–vortex approximation can no longer be considered appropriate due to the small Froude number restriction.

In all the models, we define regions in which forcing is and is not present. For regions in which a forcing is present, we see that the Rossby length $(c/f)e^{-\tau}$ decreases exponentially with time. However, this work does not explore the implications of this physical property of both balanced vortex models presented in this chapter. As discussed by Schubert et al. (2007) and Schubert and McNoldy (2010), larger dynamical eyes should produce eye features such as moats, hub clouds, a warm-ring thermal structure, and upper-level cloud overhang. This work raises questions relating to the time evolution of these features in barotropic vortices and whether or not these features would provide a diagnostic tool for both modeled and real storms.

CHAPTER 3

SHOCK-LIKE STRUCTURES IN THE SLAB TROPICAL CYCLONE BOUNDARY LAYER[2]

Questions such as "why does a tropical cyclone have an eye?", "what controls the eye size?", and "how does eyewall replacement work?" have perplexed the tropical cyclone community. From works as early as Haurwitz (1935, 1936), studies have turned to the role of the boundary layer to the development and formation of inner-core vortex features (e.g., the eye, eyewall). In an interview with Platzman (1985), Haurwitz explained that in his desire to understand why tropical cyclones have eyes, he turned to a linearized form of the boundary layer akin to Ekman (1905). Haurwitz rightly assumed that the frictionally induced convergence of boundary layer air and resulting Ekman pumping play vital roles in the formation and placement of the eye and eyewall. After a respite in the literature, the works by Ooyama (1969a,b), Rosenthal (1970, 1971), Eliassen (1971), Eliassen and Lystad (1977), and Yamasaki (1977) returned to the boundary layer in search of an explanation of where the Ekman pumping maximizes in relation to the axis of the tropical cyclone and the radius of maximum winds. While not all of the mass pumped out of the boundary layer is ventilated into the eyewall, the location of the maximized Ekman pumping due to frictional convergence is critical in organizing the annular ring of diabatic heating associated with the eyewall (e.g., Ooyama 1969a,b, 1982; Raymond and Herman 2012; Kepert and Nolan 2014; Frisius and Lee 2016). The placement of this diabatic heating is critical to determining how a storm will evolve in terms of the intensity and structure (Eliassen 1951; Shapiro and Willoughby 1982; Schubert and Hack 1982) as discussed in chapter 2. The intensity and structure are directly and indirectly impacted by the location of eyewall convection (e.g., where the diabatic heating is located in proximity to the high inertial stability region and diabatic heating associated with outer and spiral rainbands). More recent work suggests that the boundary layer has a fundamental role in the formation of secondary eyewalls and the replacement of the primary eyewall. As these topics have been of interest to the community from aspects of basic science and forecasting, understanding the level to which the tropical cyclone boundary layer influences these processes is key to creating a conceptual picture of the early stages of the "life cycle" of the tropical cyclone.

While recent work has focused on full-physics model simulations during rapid intensification and secondary eyewall formation to understand the role of the boundary layer in these processes, some

[2]This chapter contains material and results included in Slocum et al. (2014) and Schubert et al. (2017).

of the fundamental dynamics of the tropical cyclone boundary layer have yet to be completely understood. The role of the nonlinear terms in the boundary layer equations is one source of disagreement within the tropical cyclone boundary layer literature (Ooyama 1969a,b; Kepert 2001; Kepert and Wang 2001; Vogl and Smith 2009; Kepert 2017). Ooyama (1969a,b) shows that the inclusion of the nonlinear terms shifts the Ekman pumping inside of the radius of maximum gradient wind, which would assist in shifting the annular ring of diabatic heating into the high inertial stability region of the vortex. However, Kepert (2001) suggests that an Ekman-like linearization is a reasonably first order approximation to the structure and is adequate in capturing the role of the tropical cyclone boundary layer in the overall "life cycle." In addition to the updraft placement, the nonlinear terms are also responsible for the development of supergradient winds within the tropical cyclone boundary layer, a well observed feature (La Seur and Hawkins 1963; Hawkins and Rubsam 1968; Willoughby 1990) that some studies have deemed a critical feature to reproduce in modeling work (Smith and Vogl 2008; Bryan and Rotunno 2009).

Recently, the literature has turned to the boundary layer to explain secondary eyewall formation and eyewall replacement. Again, full-physics modeling studies have been used to highlight features such as the expansion of gradient wind above the boundary layer before the onset of eyewall formation and replacement as well as a reduction of the inflow to the primary eye (Rozoff et al. 2012). While the argument has been made that the boundary layer plays a role, the full extent to which this is the case is not completely understood. The debate over the importance of nonlinear terms in the boundary layer equations extends to discussions related to secondary eyewall formation and eyewall replacement (Kepert 2013; Abarca and Montgomery 2013; Montgomery et al. 2014; Kepert and Nolan 2014).

To add to the discussion of the role of the boundary layer, we will investigate how and when the nonlinear terms come into play through using shock dynamics. Figure 3.1 shows observed flight-level winds from aircraft reconnaissance for Hurricanes Allen (1980) on 06 August and Hugo (1989) on 15 September. For both storms, the NOAA WP-3D Orion aircraft is flying at an altitude near 450 m. In the tangential and radial wind profiles, abrupt jumps in the wind are present. In Hurricane Allen (1980), the tangential wind drops from 80 to 40 m s^{-1} and the radial inflow is reduced by 30 m s^{-1} over 5 km. The change for Hurricane Hugo (1989) is much more abrupt with the tangential wind dropping 60 m s^{-1} and the inflow changing by 35 m s^{-1} in approximately 1 km. Williams et al. (2013) and Slocum et al. (2014) interpret these abrupt changes as "shock-like" structures arising from the nonlinear terms in the boundary layer equations. Shocks can be understood through Burgers' equation, the simplest equation

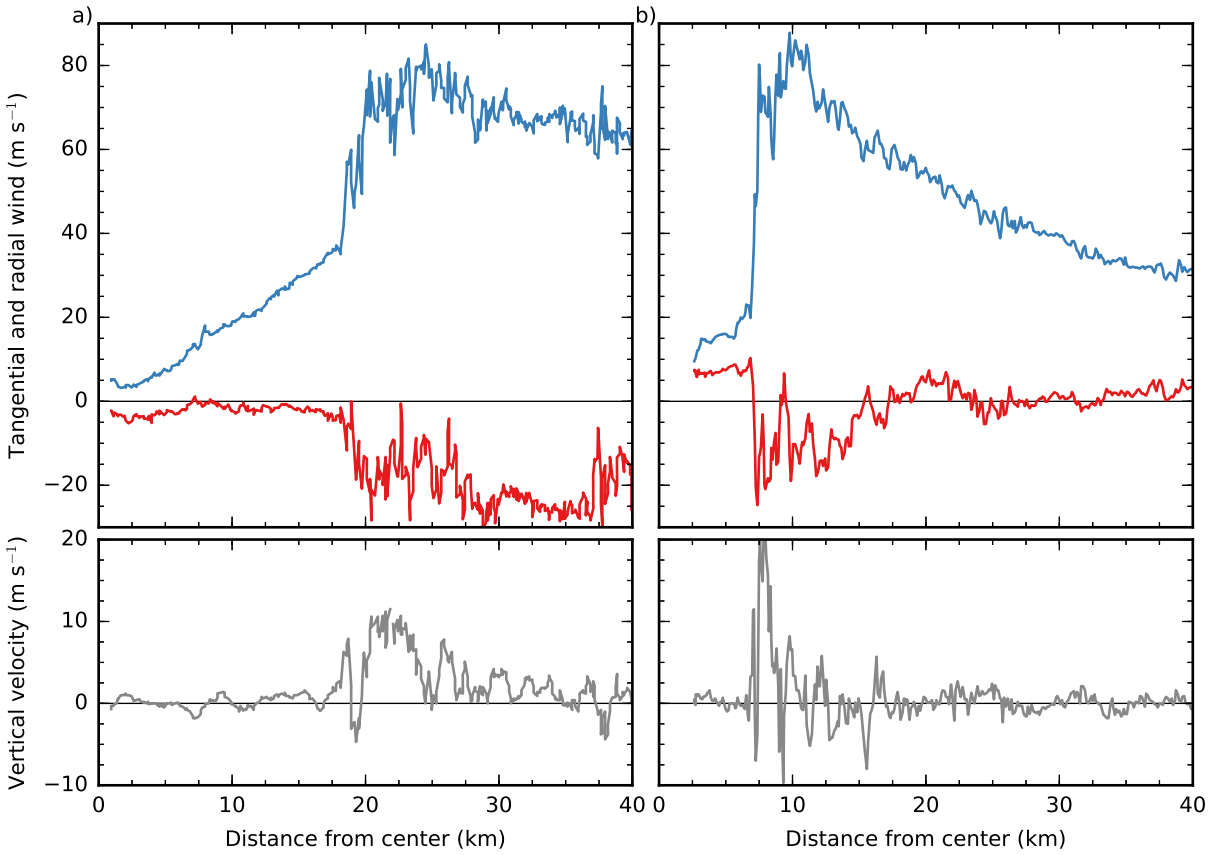

FIG. 3.1. Flight-level winds from aircraft reconnaissance from the NOAA WP-3D Orion for a) Hurricanes Allen on 06 August 1980 and b) Hugo on 15 September 1989. The flight-level altitude for both storms is near 450 m or 950 hPa. The top row contains the tangential winds v (blue curve) and radial winds u (red curve) and the bottom row is the vertical velocity w (gray curve).

combining both nonlinear propagation and diffusive effects (Bateman 1915; Burgers 1948). Williams et al. (2013) and Slocum et al. (2014) note that the radial momentum equation contains an embedded Burgers' equation, which plays a role in flows that are out of gradient balance such as the boundary layer. In these works, the authors show that near-discontinuous radial and tangential winds and corresponding near-singular frictional updrafts (i.e., Ekman pumping) and vorticity develop from smooth initial conditions. Slocum et al. (2014) and Schubert et al. (2017) offered a set of "metaphor" or "toy" models that show that a subset of terms from the full slab boundary layer equations can be solved through the method of characteristics to assist in understanding the connection between the embedded Burgers' equation and the inner-core dynamics of tropical cyclones.

This work extends previous work on invoking shock dynamics to understand the tropical cyclone boundary layer, the placement and magnitude of the frictionally induced convergence, and criteria for when the nonlinear terms play a vital role in the "life cycle" of tropical cyclones. In section 3.1,

we present the depth-averaged, f-plane boundary layer equations. In section 3.2, we discuss basic concepts involved with shock formation using a series of "metaphor" models. Solutions for shocks with curvature and surface drag effects and for y-independent shocks are obtained in sections 3.2.1 and 3.2.2 . In section 3.3, we develop two different local approximations to the slab boundary layer equations. In section 3.4, we present results for a steady forcing for the nonlinear model and local models. In section 3.5, we explore changes to the boundary layer with an expanding wind field to provide insight into eyewall replacement. Lastly, we provide some concluding remarks in section 3.6.

3.1 SLAB BOUNDARY LAYER MODEL

We consider a depth-averaged, f-plane boundary layer model that is for an axisymmetric, incompressible fluid, as outlined by Williams et al. (2013), Slocum (2013), and Slocum et al. (2014).[3] The horizontal wind components are discontinuous across the top of the boundary layer. In the overlying layer, the radial wind is assumed to be negligible and the tangential wind is assumed to be in gradient balance and constant in time. The boundary layer flow is driven by the radial pressure gradient force that occurs in the overlying fluid. This means that the pressure gradient force is expressed as the specified function $\rho^{-1}(\partial p/\partial r) = (f + v_{\rm gr}/r)\, v_{\rm gr}$, where $v_{\rm gr}(r)$ is the tangential wind in gradient balance. Kepert (2017) revisited the idea that the boundary layer can be solved as a response to a constant gradient balanced flow in the overlying layer. He concluded that the approximation is representative of tropical cyclones. The governing system of differential equations take the form

$$\frac{\partial u}{\partial t} + u\frac{\partial u}{\partial r} + w^{-}\left(\frac{u}{h}\right) = \left(f + \frac{v + v_{\rm gr}}{r}\right)(v - v_{\rm gr}) - c_{_D} U \frac{u}{h} + K\frac{\partial}{\partial r}\left(\frac{\partial (r\,u)}{r\,\partial r}\right), \tag{3.1}$$

$$\frac{\partial v}{\partial t} + u\left(f + \frac{\partial v}{\partial r} + \frac{v}{r}\right) + w^{-}\left(\frac{v - v_{\rm gr}}{h}\right) = -c_{_D} U \frac{v}{h} + K\frac{\partial}{\partial r}\left(\frac{\partial (r\,v)}{r\,\partial r}\right), \tag{3.2}$$

$$w = -h\frac{\partial (r\,u)}{r\,\partial r} \quad \text{and} \quad w^{-} = \frac{1}{2}(|w| - w), \tag{3.3}$$

where

$$U = k\left(u^2 + v^2\right)^{1/2} \tag{3.4}$$

[3] It should be noted that the slab (i.e., depth-averaged) boundary layer model used in this work employs different methods than the models used by Smith (2003), Smith and Vogl (2008), and Kepert (2010a,b), In the formulation of the slab model used in these papers, the authors follow Smith (1968) and Ooyama (1969a) by integrating inward from a large radius. The authors find that certain $v_{\rm gr}(r)$ profiles produce oscillations and can fail to find a solution inward to $r = 0$; both features tend to occur for small, strong vortices. One possible explanation for the existence of these features is the presence of shocks in the fluid dynamics. Thinking about the problem from the standpoint of the system's families of characteristics, the information from large radii does not guarantee a solution of the system with the possibility of shocks. The model used here uses both an inner and outer boundary condition and integrates in time to find the solution to the slab boundary layer model. The inclusion of numerical diffusion prevents the model from becoming multivalued if shocks do indeed form (Von Neumann and Richtmyer 1950).

is the wind speed at 10 m height, f is the constant Coriolis parameter, K is the constant horizontal diffusivity, and k is the relationship between the 10 m wind and the mean boundary layer wind taken here as the wind speed throughout the depth, h, of the model. The drag coefficient, c_D, is assumed to depend on the 10 m wind speed according to the function

$$c_D = 10^{-3} \begin{cases} 2.70/U + 0.142 + 0.0764\,U & \text{if } U \leq 25 \\ 2.16 + 0.5406\,\{1 - \exp[-(U-25)/7.5]\} & \text{if } U \geq 25, \end{cases} \tag{3.5}$$

where the 10 m wind speed U is expressed in m s^{-1}. The first line of (3.5) where $U \leq 25$ is based on Large and Pond (1982) and Large et al. (1994). At extreme wind speeds, the value of c_D is still up for debate.[4] For $U \geq 25$, we have chosen a function based on Powell et al. (2003) and Donelan et al. (2004) in which the value of c_D saturates at 2.8×10^{-3} at large wind speeds. The value of k is also under some debate. Observational work suggests that a reasonable value is in the range $0.78 \leq k \leq 0.83$, but the value could fall within $0.55 \leq k \leq 0.97$ (Deardorff 1968; Powell et al. 2003, 2009; Harper et al. 2010). We have chosen $k = 0.80$ for the simulations contained in this work. Despite the uncertainties associated with c_D and k, we note that the quantitative differences are small and the qualitative interpretation is unchanged.

3.2 Some basic concepts involved with shocks

While solving the slab boundary layer model (3.1)–(3.2) requires numerical methods, it is possible to simplify the slab boundary layer equations to understand portions of the dynamics. In making simplifications to find analytic solutions, we lose some physical effects that are essential to relating the analytic solutions to tropical cyclones. With this in mind, we will consider the models presented here as "toys" or "metaphors." The insight we gain from these models will assist in interpreting the results from the complete slab boundary layer model. In this section, we will first explore the effect of ignoring the pressure gradient and horizontal diffusion terms, then we will bring back the pressure gradient terms in a line symmetric framework.

To offer context for these "toy" or "metaphor" models, we will briefly discuss some of the features that arise from smooth initial conditions in hyperbolic systems. The shock dynamic literature tends to classify the shock waves into two categories — triangular waves and N-waves (Whitham 1974; LeVeque 1992). In Fig. 3.2, the upper panel of the schematic shows an initial condition for the formation

[4] Equation (3.5) assumes that c_D levels off at high wind speeds. However, more recent literature argues that c_D decreases as the wind speed continues to increase. In the context of the work presented here, the difference in c_D at high wind speeds does not change the interpretation of the results.

of a triangular wave. The profile shows a background wind speed U of -5 m s^{-1} with a region of enhanced flow (i.e., $u_0(x) < U$). The lower panel shows the evolution of this profile's characteristics in time. The brown line shows the formation of a shock in which the information from the intersecting characteristics is lost. In Fig. 3.3, the upper panel of the schematic shows an initial condition for the formation of an N-wave. In this scenario, the initial profile has a region of enhanced inflow and a region of reduced inflow. The lower panel of Fig. 3.3 shows the evolution of the characteristics. In this case, a pair of shocks form to develop an N-wave. Schubert et al. (2017) use the formation of triangular waves and N-waves in solutions to Burgers' equation to explain aspects of the dynamics associated with primary and secondary eyewalls in tropical cyclones. At first glance at Figs. 3.2 and 3.3, it is clear why one would make such an analogy when looking at radial inflow profiles from the tropical cyclone boundary layer. In that work, the authors apply the Cole–Hopf transformation (Lighthill 1956; Whitham 1974) to find analytic solutions of Burgers' equation and make analogies to the tropical cyclone boundary layer. Keeping the ideas associated with triangular waves and N-waves in mind, we will step through several of these "metaphor" models.

3.2.1 Solutions for shocks with curvature and surface drag effects

In Slocum et al. (2014), the authors argue that the dependence of shock formation in the u and v fields in the tropical cyclone boundary layer depends on the $u(\partial u/\partial r)$ and $u[f+(\partial v/\partial r)+(v/r)]$ terms in (3.1) and (3.2). To understand the flow of information within the system, we approximate the radial and tangential wind equations in the boundary layer by neglecting the horizontal diffusion terms, the w^- terms, and the agradient forcing $(v-v_{\mathrm{gr}})$ term. Equations (3.1) and (3.2) simplify to

$$\frac{\partial u}{\partial t}+u\frac{\partial u}{\partial r}=-\frac{u}{\tau}, \tag{3.6}$$

$$\frac{\partial v}{\partial t}+u\left(f+\frac{\partial v}{\partial r}+\frac{v}{r}\right)=-\frac{v}{\tau}, \tag{3.7}$$

where the constant damping time scale τ is a typical value of $h/(c_{_D}U)$. As can be shown through a scale analysis, (3.6) and (3.7) do not capture important features of the tropical cyclone boundary layer. However, they provide a context for interpreting part of the dynamics involved in the tropical cyclone boundary layer. To understand the differences between (3.1)–(3.2) and (3.6)–(3.7), it must be noted that the forcing in the slab model generates the same final u profile regardless of the initial u profile as will be shown in section 3.4. In this simple model, u must be nonzero and the choice of the initial u profile affects the time and radius of shock formation.

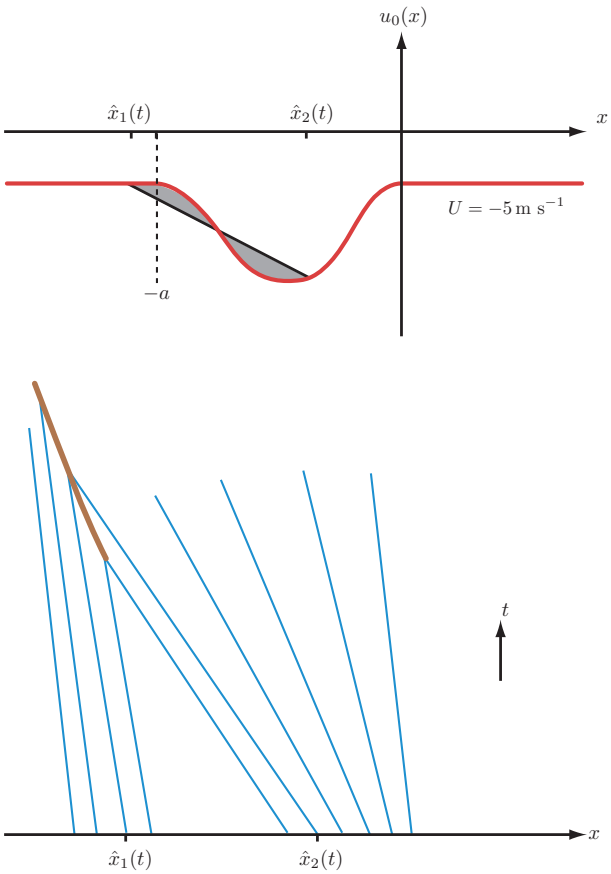

FIG. 3.2. The upper panel shows the initial condition $u_0(x)$, which has the constant value $U = -5$ m s^{-1} for $x \le -a$ and $x \ge 0$, and has enhanced inflow, $u_0(x) < U$, in the region $-a < x < 0$. The lower panel shows selected characteristics in the (x, t) plane. According to the equal area property, the two characteristics labeled $\hat{x}_1(t)$ and $\hat{x}_2(t)$ will simultaneously reach the shock at time t if the secant line between them cuts off equal areas of the $u_0(x)$ curve, as indicated by the gray shaded region in the upper panel.

We continue to present the work done by Slocum et al. (2014) to find solutions to (3.6)–(3.7), which can be written in the form

$$\left.\begin{aligned} \frac{d}{dt}\left\{u e^{t/\tau}\right\} &= 0 \\ \frac{d}{dt}\left\{r v e^{t/\tau} + f\left[\hat{r}\,t + u_0(\hat{r})\tau\left(t - \hat{t}(t)\right)\right] u_0(\hat{r})\right\} &= 0 \end{aligned}\right\} \text{ on } \frac{dr}{dt} = u, \tag{3.8}$$

where $(d/dt) = (\partial/\partial t) + u(\partial/\partial r)$ is the derivative following the boundary layer radial motion. The characteristics $\hat{r}$ are defined as

$$r = \hat{r} + \hat{t}(t) u_0(\hat{r}), \tag{3.9}$$

with the function $\hat{t}(t)$ defined as

$$\hat{t}(t) = \tau\left(1 - e^{-t/\tau}\right). \tag{3.10}$$

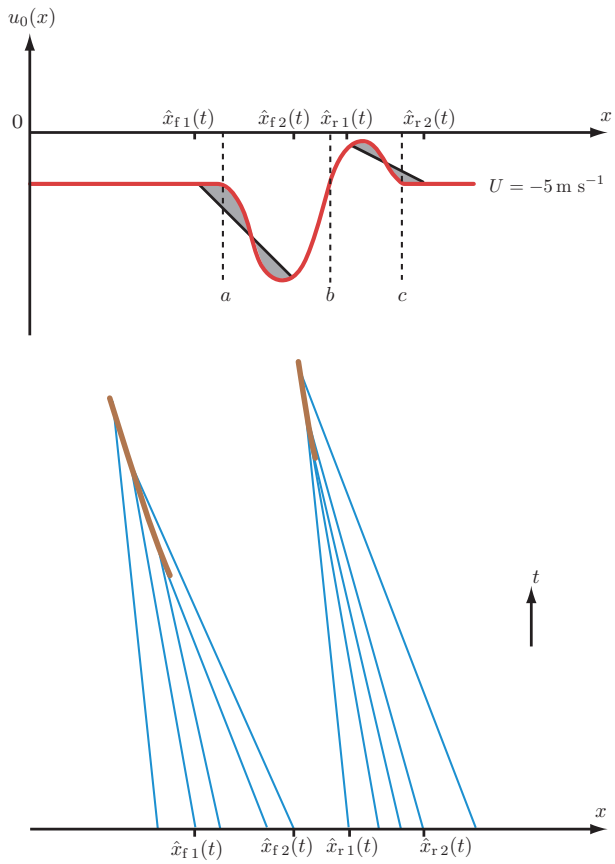

FIG. 3.3. The upper panel shows the initial condition $u_0(x)$, which has the constant value $U = -5$ m s^{-1} for $x \le a$, $x \ge c$, and $x = b$; enhanced inflow, $u_0(x) < U$, in the region $a < x < b$; and reduced inflow, $u_0(x) > U$, in the region $b < x < c$. The lower panel shows selected characteristics in the (x,t) plane. According to the equal area property, the two characteristics labeled $x_{f1}(t)$ and $x_{f2}(t)$ will simultaneously reach the forward shock if the secant line on the left cuts off equal areas of the $u_0(x)$ curve. Similarly, the two characteristics labeled $x_{r1}(t)$ and $x_{r2}(t)$ will simultaneously reach the rear shock if the secant line on the right cuts off equal areas of the $u_0(x)$ curve. In this example, the forward shock forms sooner and is stronger. Note that the divergent region between the shocks becomes wider with time.

Integration of (3.8) yields the solutions

$$u(r,t) = u_0(\hat{r})e^{-t/\tau}, \tag{3.11}$$

$$r\upsilon(r,t) = \left\{\hat{r}\,\upsilon_0(\hat{r}) - f\left[\hat{r}\,t + u_0(\hat{r})\tau\left(t - \hat{t}(t)\right)\right]u_0(\hat{r})\right\}e^{-t/\tau}. \tag{3.12}$$

For a given characteristic $\hat{r}$, $u(r,t)$ exponentially damps according to the solution (3.11). However, (3.12) shows that $\upsilon(r,t)$ varies in a much more complicated way with time due to the $(\hat{r}/r)e^{-t/\tau}$ factor. The result of (3.12) is that $\upsilon(r,t)$ can increase along characteristics. Another way to think about the effect of the amplification factor $(\hat{r}/r)$ is that it allows for the development of a supergradient region,

$v > v_{\text{gr}}$, and a subgradient region, $v < v_{\text{gr}}$. Through using (3.9), we can eliminate $u_0(\hat{r})$ in (3.12) to obtain another useful form

$$r\,v(r,t) = \left\{ \hat{r}\,v_0(\hat{r}) + f\,\frac{t}{\hat{t}(t)}\left[\hat{r} + (r-\hat{r})\left(\frac{\tau\left[t-\hat{t}(t)\right]}{t\,\hat{t}(t)} \right) \right](\hat{r}-r) \right\} e^{-t/\tau}. \tag{3.13}$$

In the context of (3.6) and (3.7), we can understand when the derivatives $(\partial u/\partial r)$ and $(\partial v/\partial r)$ become infinite, i.e. discontinuities develop in u and v. First, we note that taking $(\partial/\partial t)$ and $(\partial/\partial r)$ of (3.9) gives us

$$-\frac{\partial \hat{r}}{\partial t} = \frac{u_0(\hat{r})e^{-t/\tau}}{1+\hat{t}(t)u_0'(\hat{r})}, \tag{3.14}$$

$$\frac{\partial \hat{r}}{\partial r} = \frac{1}{1+\hat{t}(t)u_0'(\hat{r})}. \tag{3.15}$$

Next, we take $(\partial/\partial t + 1/\tau)$ and $u(\partial/\partial r)$ of (3.11) to yield

$$\frac{\partial u}{\partial t} + \frac{u}{\tau} = e^{-t/\tau}u_0'(\hat{r})\frac{\partial \hat{r}}{\partial t} = -\frac{e^{-2t/\tau}u_0(\hat{r})u_0'(\hat{r})}{1+\hat{t}(t)u_0'(\hat{r})}, \tag{3.16}$$

$$u\frac{\partial u}{\partial r} = e^{-2t/\tau}u_0(\hat{r})u_0'(\hat{r})\frac{\partial \hat{r}}{\partial r} = \frac{e^{-2t/\tau}u_0(\hat{r})u_0'(\hat{r})}{1+\hat{t}(t)u_0'(\hat{r})}, \tag{3.17}$$

where the final equalities follow from using (3.14) and (3.15) to eliminate $(\partial \hat{r}/\partial t)$ and $(\partial \hat{r}/\partial r)$. Then, taking the sum of (3.16) and (3.17), we see that (3.11) and (3.12) constitute a solution of (3.6) and (3.7).

Now, we can compute the time of shock formation, t_s, by assessing the behaviors of the denominators of the right-hand sides of (3.16) and (3.17). The derivatives $(\partial u/\partial t)$ and $(\partial u/\partial r)$ become infinite if

$$\hat{t}(t)u_0'(\hat{r}) = -1 \tag{3.18}$$

along one or more of the characteristics. Returning to the definition of τ, we see that $0 \le \hat{t}(t) < \tau$. This means that if the value $\hat{t}(t)$ does not become large enough to satisfy (3.18), a shock will not form. Stated another way, shock formation is possible if and only if $\tau[u_0'(\hat{r}_s)] < -1$, where $\hat{r}_s$ is the originating characteristic for shock formation. In the case of (3.6) and (3.7), $\hat{r}_s$ corresponds to the minimum value of $u_0'(r)$. Using (3.10) and (3.18), the shock formation time is

$$t_s = -\tau \ln\left(1 + \frac{1}{\tau\,u_0'(\hat{r}_s)}\right), \tag{3.19}$$

and the radius of shock formation determined by (3.9) and (3.18) is

$$r_s = \hat{r}_s - \frac{u_0(\hat{r}_s)}{u_0'(\hat{r}_s)}. \tag{3.20}$$

An interesting point that arises from (3.19) and (3.20) is that t_s is dependent on the damping time scale τ, but r_s is independent of τ.

From the solutions for $u(r,t)$, (3.11), and $v(r,t)$, (3.12), we can compute the solutions for the divergence, $\delta(r,t) = \partial[r\,u(r,t)]/r\,\partial r$, and the relative vorticity, $\zeta(r,t) = \partial[r\,v(r,t)]/r\,\partial r$. The boundary layer divergence or equivalently the boundary layer pumping, $w(r,t) = -h\delta(r,t)$, is obtained by using (3.11), which yields

$$\delta(r,t) = \left(\frac{u_0'(\hat{r})}{1+\hat{t}(t)u_0'(\hat{r})} + \frac{u_0(\hat{r})}{r}\right)e^{-t/\tau}. \tag{3.21}$$

Similarly, the relative vorticity is obtained by differentiation of (3.12), which yields

$$\begin{aligned}\zeta(r,t) = \Bigg\{ &\left(\frac{\left[1+\left(1-\frac{r}{\hat{r}}\right)\left(1-\frac{2\tau\left[t-\hat{t}(t)\right]}{t\,\hat{t}(t)}\right)\right]f + \zeta_0(\hat{r})}{1+\hat{t}(t)u_0'(\hat{r})}\right)\frac{t}{\hat{t}(t)}\frac{\hat{r}}{r} \\ &- f\frac{t}{\hat{t}(t)}\left[1-\left(1-\frac{r}{\hat{r}}\right)\left(1-\frac{2\tau\left[t-\hat{t}(t)\right]}{t\,\hat{t}(t)}\right)\right]\Bigg\}e^{-t/\tau},\end{aligned} \tag{3.22}$$

where $\zeta_0(r) = \partial[r\,v_0(r)]/r\,\partial r$ is the initial relative vorticity. Because of the presence of the $1+\hat{t}(t)u_0'(\hat{r})$ term in the denominators of both (3.21) and (3.22), the relative vorticity $\zeta(r,t)$, divergence $\delta(r,t)$, and boundary layer pumping $w(r,t)$ become infinite when $\hat{t}(t)u_0'(\hat{r}) = -1$.

In a simple example, we will start with an initial condition that allows for the formation of a triangular wave in which

$$u_0(r) = u_m\left(\frac{4(r/a)^3}{1+3(r/a)^4}\right), \tag{3.23}$$

$$v_0(r) = v_m\left(\frac{2(r/a)}{1+(r/a)^2}\right), \tag{3.24}$$

where the constants a, u_m, and v_m specify the radial extent and strength of the initially smooth radial and tangential flow. The derivative of (3.23) is

$$u_0'(r) = \frac{12u_m}{a}\left(\frac{(r/a)^2\left[1-(r/a)^4\right]}{\left[1+3(r/a)^4\right]^2}\right), \tag{3.25}$$

and the initial relative vorticity is obtained by differentiation of (3.24)

$$\zeta_0(r) = \frac{4\upsilon_m}{a[1+(r/a)^2]}. \tag{3.26}$$

With the initial conditions (3.23) and (3.24), (3.11) and (3.12) become

$$u(r,t) = u_m\left(\frac{4(r/a)^3}{1+3(r/a)^4}\right)e^{-t/\tau}, \tag{3.27}$$

$$\upsilon(r,t) = \left\{\hat{r}\,\upsilon_m\left(\frac{2(r/a)}{1+(r/a)^2}\right) + f\,\frac{t}{\hat{t}(t)}\left[\hat{r} + (r-\hat{r})\left(\frac{\tau\left[t-\hat{t}(t)\right]}{t\,\hat{t}(t)}\right)\right](\hat{r}-r)\right\}e^{-t/\tau}, \tag{3.28}$$

and the characteristic equation (3.20) is defined by

$$r = \hat{r} + u_m\left(\frac{4(r/a)^3}{1+3(r/a)^4}\right)\hat{t}(t). \tag{3.29}$$

For the initial conditions (3.23) and (3.24), we find that the time of shock formation t_s is given by

$$t_s \approx -\tau\ln\left(1-\frac{a}{2.032\tau|u_m|}\right), \tag{3.30}$$

and the position of the shock formation r_s is

$$r_s \approx 0.5426\hat{r}_s \approx 0.2931a. \tag{3.31}$$

Isolines of the shock formation time t_s, as given by (3.30), are shown in Fig. 3.4. As U increases, it becomes less likely for larger storms with weak inflow to develop a shock. Weak storms, on the other hand, are more likely to form a shock, but the long time until shock formation indicates that this process could easily be interrupted. The solutions for u, υ, w, and ζ/f, as given by (3.27) and (3.28), are plotted in Fig. 3.5 for the constants $U = 35$ m s^{-1}, $a = 60$ km, and $u_m = 4.5, 9$ m s^{-1}. The plots cover the region from $0 \le r \le 100$ km and are for $t = 0$ and $t = t_s$, where $t_s = 1.82, 0.91$ h is the shock formation time for each initial condition. The time evolution of the divergence and vorticity along the first shock-producing characteristic (not shown here) indicates that both examples are vorticity-preferred, i.e., $|\delta|/\zeta < 1$.

While this model assists in understanding the characteristics $\hat{r}$ and shock formation time t_s in a subset of the boundary layer equations that includes curvature effects, these cases are dependent upon the initial radial wind profile because the axisymmetric solutions presented here lack the agradiant forcing term $(\upsilon - \upsilon_{\rm gr})$.

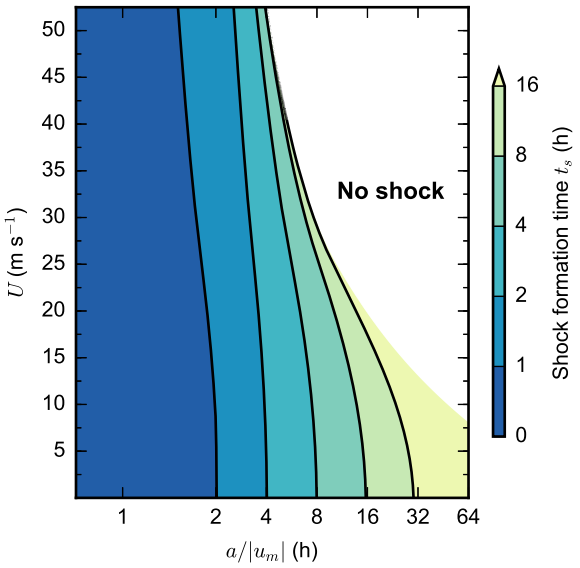

FIG. 3.4. Isolines of the shock formation time t_s (colored shading) for axisymmetric solutions of shocks with surface drag effects, as described by (3.30). The abscissa is a measure of the maximum initial convergence (h) and the ordinate is the wind speed U (m s^{-1}).

3.2.2 Solutions for y -independent shocks

In the previous section, we solve the hyperbolic system of equations using the method of characteristics through neglecting the horizontal diffusion, the w^-, and the pressure gradient forcing terms, but we kept curvature effects. In this section, we return to the slab boundary layer model equations (3.1) and (3.2) to make a different set of assumptions to further advance our understanding of the complete system. As in Schubert et al. (2017), we consider the line-symmetric slab boundary layer equations

$$\frac{\partial u}{\partial t} + u\frac{\partial u}{\partial x} - fv + \frac{c_D U}{h}u = -\frac{1}{\rho}\frac{\partial p}{\partial x}, \tag{3.32}$$

$$\frac{\partial v}{\partial t} + u\frac{\partial v}{\partial x} + fu + \frac{c_D U}{h}v = 0, \tag{3.33}$$

where we now define the wind speed as $U = (u^2+v^2)^{1/2}$ and where f is the constant Coriolis parameter, h is the boundary layer depth, and c_D is the drag coefficient. We set f, h, and c_D to 5×10^{-5} s^{-1}, 1000 m, and 2×10^{-3} respectively. Similar to the full slab boundary layer model equations, the forcing term $-(1/\rho)(\partial p/\partial x)$ is interpreted as a specified geostrophic wind v_g because $fv_g = (1/\rho)(\partial p/\partial x)$. In

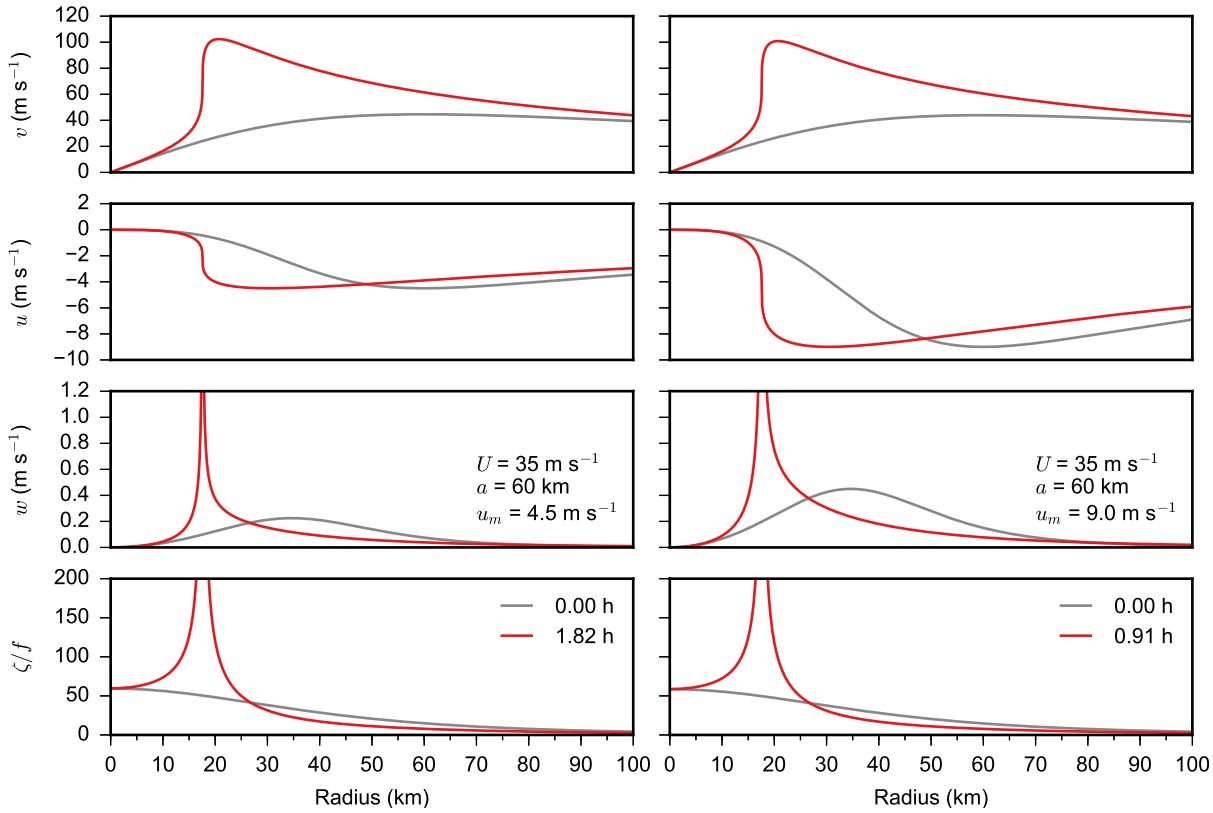

FIG. 3.5. The two columns show two examples for shocks as determined by the axisymmetric analytic solutions (3.27) and (3.28). The initial conditions are in the gray curves, while the distributions at the shock formation times are shown by the red curves. Both cases have $U = 35$ m s^{-1} and $a = 60$ km with $u_m = 4.5$ m s^{-1} for the left column and $u_m = 9$ m s^{-1} for the right column.

order to find an analytic solution to (3.32) and (3.33), we assume that v_g is a constant in t and x for an infinite domain and subject to the initial conditions

$$u(x,0) = u_0(x) \quad \text{and} \quad v(x,0) = v_0(x), \tag{3.34}$$

where $u_0(x)$ and $v_0(x)$ are specified functions. As noted at the start of this section, the lack of curvature effects and spatial variation in the pressure gradient forcing terms means that we must regard this model as a metaphor to the full tropical cyclone boundary layer model. However, (3.32) and (3.33) provide another opportunity to solve the coupled pair of equations analytically and increase our understanding of shock dynamics within the full slab.

From the quasi-linear system (3.32) and (3.33), we will introduce the constant Ekman flow components u_E and v_E so that we can solve the hyperbolic system through the methods of characteristics. The nonlinear algebraic system is

$$-f v_E + \frac{c_D U_E}{h} u_E = -f v_g, \tag{3.35}$$

$$f u_E + \frac{c_D U_E}{h} v_E = 0, \tag{3.36}$$

where $U_E = (u_E^2 + v_E^2)^{1/2}$. The solutions to (3.35) and (3.36) are

$$u_E = -\left(\frac{f(c_D U_E/h)}{f^2 + (c_D U_E/h)^2} \right) v_g, \tag{3.37}$$

$$v_E = \left(\frac{f^2}{f^2 + (c_D U_E/h)^2} \right) v_g. \tag{3.38}$$

Equations (3.37) and (3.38) are implicit because of the U_E dependence on u_E and v_E. Taking the square of (3.37) and (3.38), we can find an explicit solution for $c_D U_E/h$. Adding the result, we obtain

$$k^2 = \left(\frac{f^2}{f^2 + k^2} \right) k_g^2, \tag{3.39}$$

where $k = c_D U_E/h$ and $k_g = c_D v_g/h$ are the inverse of damping time scales. We will interpret k/f as the "slab Ekman number" and k_g/f as the "forced Ekman number." We solve (3.39) as a quadratic for k^2 to obtain

$$\frac{k}{f} = \left\{ \left[\frac{1}{4} + \left(\frac{k_g}{f} \right)^2 \right]^{1/2} - \frac{1}{2} \right\}^{1/2}. \tag{3.40}$$

Now, we approximate $c_D U$ with $c_D U_E$ in (3.32) and (3.33)

$$\frac{\partial u}{\partial t} + u \frac{\partial u}{\partial x} - f v + \frac{c_D U_E}{h} u = -\frac{1}{\rho} \frac{\partial p}{\partial x}, \tag{3.41}$$

$$\frac{\partial v}{\partial t} + u \frac{\partial v}{\partial x} + f u + \frac{c_D U_E}{h} v = 0, \tag{3.42}$$

and combine this form with (3.35) and (3.36) to obtain the characteristic form

$$\left.\begin{aligned} \frac{d(u-u_E)}{dt} - f(v-v_E) + k(u-u_E) = 0 \\ \frac{d(v-v_E)}{dt} + f(u-u_E) + k(v-v_E) = 0 \end{aligned}\right\} \text{on } \frac{dx}{dt} = u, \tag{3.43}$$

where we will interpret $(d/dt) = (\partial/\partial t) + u(\partial/\partial x)$ as the derivative along a characteristic $\hat{x}$.

TABLE 3.1. The geostrophic wind v_g, the corresponding "forced Ekman number" k_g/f, the "slab Ekman number" (or dimensionless damping rate) k/f, and the steady-state Ekman layer components u_E and v_E for five selected cases.

v_g (m s^{-1})	k_g/f	k/f	u_E (m s^{-1})	v_E (m s^{-1})
10	0.4	0.3746	−3.29	8.77
20	0.8	0.6659	−9.23	13.86
30	1.2	0.8944	−14.91	16.67
40	1.6	1.0846	−19.93	18.38
50	2.0	1.2496	−24.39	19.52

The solutions to the coupled equations u and v in (3.43) are

$$u(x,t) = u_E + [u_0(\hat{x}) - u_E]e^{-kt}\cos(ft) + [v_0(\hat{x}) - v_E]e^{-kt}\sin(ft), \tag{3.44}$$

$$v(x,t) = v_E - [u_0(\hat{x}) - u_E]e^{-kt}\sin(ft) + [v_0(\hat{x}) - v_E]e^{-kt}\cos(ft), \tag{3.45}$$

where $\hat{x}$ indicates the label of the initial position of the characteristics. As can be seen by inspecting (3.44) and (3.45), there will be damped inertial oscillations along each characteristic that will eventually lead to a steady-state Ekman balance if $u_0(x) \neq u_E$ and/or $v_0(x) \neq v_E$.

We now use (3.44) and substitute $u(x,t)$ into the right-hand side of $(dx/dt) = u$. Next, we integrate from 0 to t along a characteristic and obtain

$$x = \hat{x} + u_E t + [u_0(\hat{x}) - u_E]t_1(t) + [v_0(\hat{x}) - v_E]t_2(t), \tag{3.46}$$

where the $t_1(t)$ and $t_2(t)$ functions are written as

$$t_1(t) = \frac{k - e^{-kt}[k\cos(ft) - f\sin(ft)]}{f^2 + k^2}, \tag{3.47}$$

$$t_2(t) = \frac{f - e^{-kt}[k\sin(ft) + f\cos(ft)]}{f^2 + k^2}. \tag{3.48}$$

Table 3.1 shows a range of values for the forced Ekman number k_g/f, the slab Ekman number k/f, and steady-state Ekman layer components u_E and v_E. Plots of $t_1(t)$ and $t_2(t)$ are shown in the two panels of Fig. 3.6 for the cases where $k/f = 0.7632$ and 1.0121, which correspond to $v_g = 24$ and 36 m s^{-1} respectively. $\hat{x}$ represents a unique label for each characteristic. These labels can be used to find the variation of u and v from (3.44) and (3.45). The shape of the characteristics comes from (3.46). This means that (3.44)–(3.48) are the solution to (3.32) and (3.33) from $0 \leq t \leq t_s$.

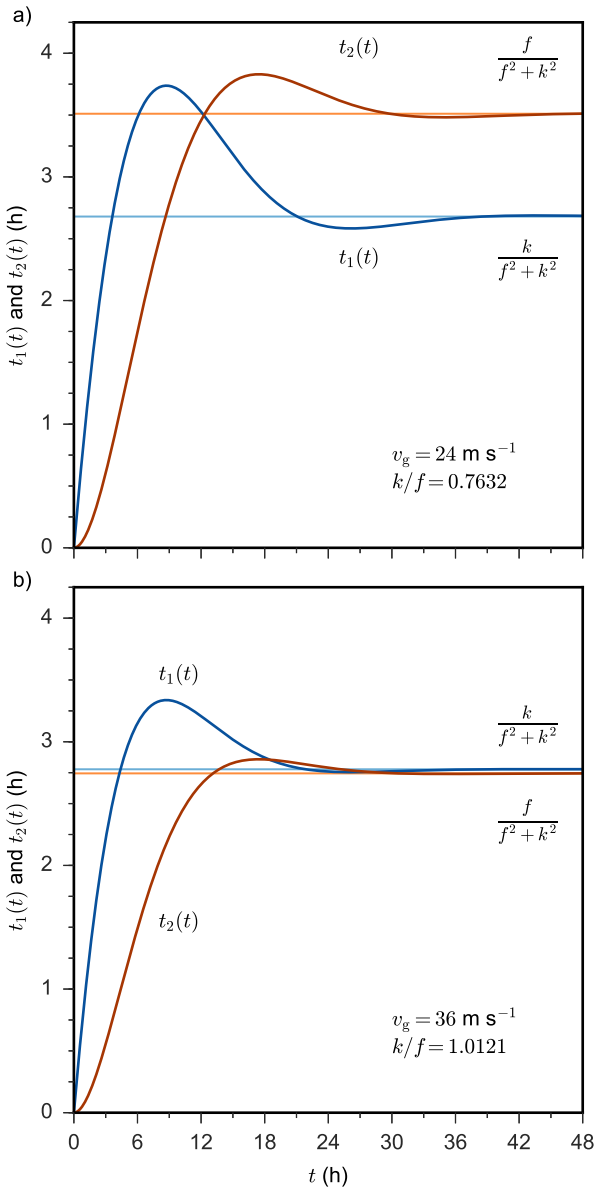

FIG. 3.6. The functions $t_1(t)$ (blue curves) and $t_2(t)$ (red curves) for a) $k/f = 0.7632$ ($v_g = 24$ m s^{-1}) and b) $k/f = 1.0121$ ($v_g = 36$ m s^{-1}). Note that $t_1(t) \to k/(f^2+k^2)$ (horizontal blue lines) and $t_2(t) \to f/(f^2+k^2)$ (horizontal red lines) as $t \to \infty$. The maximum value of $t_1(t)$ occurs at $t = \pi/(2f) \approx 8.7$ h, while the maximum value of $t_2(t)$ occurs at $t = \pi/f \approx 17.5$ h.

As in the previous section, we want to understand when the divergence $\delta = (\partial u/\partial x)$ and the vorticity $\zeta = (\partial v/\partial x)$ become infinite. First, we will take $(\partial/\partial x)$ of (3.46) to obtain

$$\frac{\partial \hat{x}}{\partial x} = \frac{1}{1 + t_1(t)\delta_0(\hat{x}) + t_2(t)\zeta_0(\hat{x})}. \tag{3.49}$$

Using this, we take the $(\partial/\partial x)$ of (3.44) and (3.45)

$$\delta(x,t) = \frac{e^{-kt}[\delta_0(\hat{x})\cos(ft) + \zeta_0(\hat{x})\sin(ft)]}{1 + t_1(t)\delta_0(\hat{x}) + t_2(t)\zeta_0(\hat{x})}, \tag{3.50}$$

$$\zeta(x,t) = \frac{e^{-kt}[\delta_0(\hat{x})\sin(ft) + \zeta_0(\hat{x})\cos(ft)]}{1 + t_1(t)\delta_0(\hat{x}) + t_2(t)\zeta_0(\hat{x})}. \tag{3.51}$$

From the analytical solutions (3.50) and (3.51), we obtain

$$\left(\frac{\delta^2(x,t) + \zeta^2(x,t)}{\delta_0^2(\hat{x}) + \zeta_0^2(\hat{x})}\right)^{1/2} = \frac{e^{-kt}}{1 + t_1(t)\delta_0(\hat{x}) + t_2(t)\zeta_0(\hat{x})}. \tag{3.52}$$

Evaluating (3.50)–(3.52), we see that the divergence and vorticity share the same denominators and can become infinite when

$$t_1(t)\delta_0(\hat{x}) + t_2(t)\zeta_0(\hat{x}) = -1 \tag{3.53}$$

along one or more of the characteristic curves. It is possible that neither t_1 and t_2 will become large enough to satisfy the condition in (3.53). Equation (3.53) also alludes to the possibility that shocks can arise from either the initial divergence or vorticity fields. Schubert et al. (2017) discuss an alternative derivation of the δ and ζ solutions.

3.2.3 Line-symmetric examples

To increase our understanding of the line-symmetric slab boundary layer equations, our first set of examples will start with only an initial divergence profile. Then, we look at examples with only an initial vorticity profile. The advantage of this approach is that we can isolate the effects of $t_1(t)$ and $t_2(t)$.

In our first example, we will start by looking at the formation of a triangular wave in initially divergent flow with the initial conditions

$$u_0(x) = u_{_E} - u_m\left(\frac{1}{1 + (x/a)^2}\right) \quad \text{and} \quad \upsilon_0 = \upsilon_{_E}, \tag{3.54}$$

where the constants a and u_m specify the horizontal extent and strength of this initial symmetric divergent flow anomaly. The corresponding initial divergence and vorticity associated with (3.54) are

$$\delta_0(x) = \frac{2u_m}{a}\left(\frac{x/a}{[1 + (x/a)^2]^2}\right) \quad \text{and} \quad \zeta_0(x) = 0. \tag{3.55}$$

We assume that $u_m > 0$ so that initially, convergence appears to the left of the origin and divergence to the right. With the initial conditions (3.54) and (3.55), (3.44) and (3.45) simplify to

$$u(x,t) = u_{_E} - u_m \left(\frac{1}{1+(\hat{x}/a)^2} \right) e^{-kt} \cos(ft), \tag{3.56}$$

$$v(x,t) = v_{_E} + u_m \left(\frac{1}{1+(\hat{x}/a)^2} \right) e^{-kt} \sin(ft), \tag{3.57}$$

and the characteristic equation (3.46) becomes

$$x = \hat{x} + u_{_E} t - u_m \left(\frac{1}{1+(\hat{x}/a)^2} \right) t_1(t). \tag{3.58}$$

The solutions (3.50) and (3.51) for the divergence and vorticity simplify to

$$\delta(x,t) = \frac{\delta_0(\hat{x}) e^{-kt} \cos(ft)}{1 + t_1(t)\delta_0(\hat{x})}, \tag{3.59}$$

$$\zeta(x,t) = -\frac{\zeta_0(\hat{x}) e^{-kt} \sin(ft)}{1 + t_1(t)\delta_0(\hat{x})}, \tag{3.60}$$

so that (3.52) becomes

$$\left(\frac{\delta^2(x,t) + \zeta^2(x,t)}{\delta_0^2(\hat{x})} \right)^{1/2} = \frac{e^{-kt}}{1 + t_1(t)\delta_0(\hat{x})}. \tag{3.61}$$

From (3.59) and (3.60) or (3.61), we see that shock formation occurs along the characteristic $\hat{x}$ when the denominator becomes zero, i.e., $t_1(t)\delta_0(\hat{x}) = -1$. This occurs first along the characteristic with the minimum value of $\delta_0(\hat{x})$. For this example, the minimum value of $\delta_0(\hat{x})$ occurs at $\hat{x} = -a/\sqrt{3} \equiv \hat{x}_s$, so that, from (3.55), $\min[\delta_0(\hat{x})] = \delta_0(\hat{x}_s) = -(3\sqrt{3}/8)(u_m/a)$. Application of (3.61) along the characteristic $\hat{x} = \hat{x}_s$ yields

$$\left(\frac{\delta^2(x,t) + \zeta^2(x,t)}{\delta_0^2(\hat{x}_s)} \right)^{1/2} = \frac{e^{-kt}}{1 - (3\sqrt{3}/8)(u_m/a) t_1(t)}. \tag{3.62}$$

Using (3.62), we find that the time of shock formation t_s is given implicitly by

$$t_1(t_s) = \frac{8\sqrt{3}}{9} \frac{a}{u_m} \approx 1.54 \frac{a}{u_m}, \tag{3.63}$$

and, from (3.58), the position of the shock formation $\hat{x}_s$ is

$$\hat{x}_s = -\sqrt{3}a + u_{_E} t_s. \tag{3.64}$$

From Fig. 3.6, note that (3.63) has a solution only when $(8\sqrt{3}/9)(a/u_m)$ is smaller than the maximum value of $t_1(t)$. The maximum value of $t_1(t)$ occurs at $t=\pi/(2f)\approx 8.73$ h and, from (3.47), has the value

$$\max[t_1(t)] = \frac{k+f\exp[-(\pi/2)(k/f)]}{f^2+k^2}. \tag{3.65}$$

Thus, the condition for shock formation is

$$\frac{u_m}{fa} > \left(\frac{u_m}{fa}\right)_c \equiv \frac{8\sqrt{3}}{9}\left(\frac{1+(k/f)^2}{(k/f)+\exp[-(\pi/2)(k/f)]}\right). \tag{3.66}$$

Equations (3.63) and (3.66) have been used to construct the top panel of Fig. 3.7, which shows isolines of the shock formation time t_s and the shock critical condition (thick black curve) in the (u_m/fa, v_g) plane. There is only a weak dependence of t_s on v_g, with shock formation times less than one hour when $u_m/fa > 9$. The three columns of Fig. 3.8 show three examples of the analytical solutions (3.56)–(3.60). The four rows are plots of u, v, δ/f, and ζ/f as functions of $x-u_{_E}t$ with the initial conditions given by the gray curves and the distributions at the time of shock formation given by the red curves. The shock formation times for the three columns are $t_s = 45, 29, 22$ min for the three cases A_δ, B_δ, and C_δ. As the spatial perturbation to the background flow of the initial u increases, the final jump in the u field also increases, but the final jump in v changes little. The time evolution of the divergence and vorticity along the shock-producing characteristics for the triangular waves is shown by the bluish curves in the top panel of Fig. 3.9. Since the final jumps in v are smaller than the corresponding final jumps in u, all three cases can be classified as divergence-preferred triangular waves.

For the second example, we will look for the formation of an N-wave from an initially divergent flow with the initial conditions

$$u_0(x) = u_{_E} + u_m\left(\frac{2x/a}{1+(x/a)^2}\right) \quad \text{and} \quad v_0(x) = v_{_E}, \tag{3.67}$$

where the constants a and u_m now specify the horizontal extent and strength of this initial antisymmetric divergent flow anomaly. The initial divergence and vorticity associated with (3.67) are

$$\delta_0 = \frac{2u_m}{a}\left(\frac{1-(x/a)^2}{[1+(x/a)^2]^2}\right) \quad \text{and} \quad \zeta_0(x) = 0. \tag{3.68}$$

We assume that $u_m > 0$, which is the case leading to the formation of an N-wave and a double shock structure. With the initial conditions (3.67), the solutions (3.44) and (3.45) become

$$u(x,t) = u_E + u_m \left(\frac{2\hat{x}/a}{1+(\hat{x}/a)^2} \right) e^{-kt} \cos(ft), \tag{3.69}$$

$$v(x,t) = v_E - u_m \left(\frac{2\hat{x}/a}{1+(\hat{x}/a)^2} \right) e^{-kt} \sin(ft), \tag{3.70}$$

and the characteristic equation (3.46) becomes

$$x = \hat{x} + u_E t + u_m \left(\frac{2\hat{x}/a}{1+(\hat{x}/a)^2} \right) t_1(t). \tag{3.71}$$

The solutions (3.50) and (3.51) for the divergence and vorticity become

$$\delta(x,t) = \frac{\delta_0(\hat{x}) e^{-kt} \cos(ft)}{1 + t_1(t)\delta_0(\hat{x})}, \tag{3.72}$$

$$\zeta(x,t) = -\frac{\zeta_0(\hat{x}) e^{-kt} \sin(ft)}{1 + t_1(t)\delta_0(\hat{x})}, \tag{3.73}$$

so that (3.52) becomes

$$\left(\frac{\delta^2(x,t) + \zeta^2(x,t)}{\delta_0^2(\hat{x})} \right)^{1/2} = \frac{e^{-kt}}{1 + t_1(t)\delta_0(\hat{x})}. \tag{3.74}$$

From (3.72) and (3.73) or (3.74), we see that shock formation occurs along a characteristic $\hat{x}$ when the denominator becomes zero, i.e., $t_1(t)\delta_0(\hat{x}) = -1$. This occurs first along the two characteristics with the minimum value of the initial divergence $\delta_0(\hat{x})$, i.e., along the two characteristics with the maximum value of initial convergence. For this example, the two minimum values of $\delta_0(\hat{x})$ occur at $\hat{x} = \pm\sqrt{3}a$, so that, from (3.68), $\min[\delta_0(\hat{x})] = -u_m/4a$. Application of (3.74) along the two characteristics $\hat{x} = \pm\hat{x}_s$, where $\hat{x}_s = \sqrt{3}a$, yields

$$\left(\frac{\delta^2(x,t) + \zeta^2(x,t)}{\delta_0^2(\pm\hat{x}_s)} \right)^{1/2} = \frac{e^{-kt}}{1 - (u_m/4a)t_1(t)}. \tag{3.75}$$

From (3.75), the time of shock formation t_s is given implicitly by

$$t_1(t_s) = \frac{4a}{u_m}, \tag{3.76}$$

and, from (3.71), the positions of shock formation are

$$x_s = u_E t_s \pm 3\sqrt{3}a. \tag{3.77}$$

From Fig. 3.6, note that (3.76) has a solution only when $4a/u_m$ is smaller than the maximum value of $t_1(t)$. The maximum value of $t_1(t)$ occurs at $t=\pi/(2f)\approx 8.73$ h and, from (3.47), has the value

$$\max[t_1(t)]=\frac{k+f\exp[-(\pi/2)(k/f)]}{f^2+k^2}. \tag{3.78}$$

This means that the condition for shock formation is

$$\frac{u_m}{4fa}>\left(\frac{u_m}{4fa}\right)_c\equiv\frac{1+(k/f)^2}{(k/f)+\exp[-(\pi/2)(k/f)]}. \tag{3.79}$$

Isolines of the shock formation time t_s, as given implicitly by (3.76), and the shock condition, as given by (3.79), are shown in the bottom panel of Fig. 3.7. The solutions for u, v, δ/f, and ζ/f, as given by (3.69)–(3.73), are plotted in Fig. 3.10 for the particular constants $v_g=36$ m s^{-1}, $a=10$ km, and for the three cases $u_m=4.5,6.0,9.0$ m s^{-1}. All three examples evolve into N-waves in u and v and singularities in the Ekman pumping on both edges of the widening moat.

The time evolution of the divergence and vorticity along the shock-producing characteristics for these N-waves is shown by the bluish curves in the lower panel of Fig. 3.9. All three cases are divergence-preferred, so the discontinuities in u are larger than those in v.

In the last two examples, we explored the formation of triangular waves and N-waves in initial conditions with nonzero divergence and zero vorticity. Next, we will examine the formation of triangular waves and N-waves in a series of initial conditions that have zero divergence and nonzero vorticity.

For the first set of simple examples for flow with initial vorticity, we consider the formation of triangular waves with the initial conditions

$$u_0(x)=u_E\quad\text{and}\quad v_0(x)=v_E-v_m\left(\frac{1}{1+(x/b)^2}\right), \tag{3.80}$$

where the constants b and v_m specify the horizontal extent and strength of this initial rotational flow anomaly. The initial divergence and vorticity associated with (3.80) are

$$\delta_0(x)=0\quad\text{and}\quad\zeta_0(x)=\frac{2v_m}{b}\left(\frac{1}{[1+(x/b)^2]^2}\right). \tag{3.81}$$

We assume $v_m>0$ so that negative initial vorticity appears to the left of the origin. With these initial conditions, the solutions (3.44) and (3.45) simplify to

$$u(x,t)=u_E-v_m\left(\frac{1}{1+(\hat{x}/b)^2}\right)e^{-kt}\sin(ft), \tag{3.82}$$

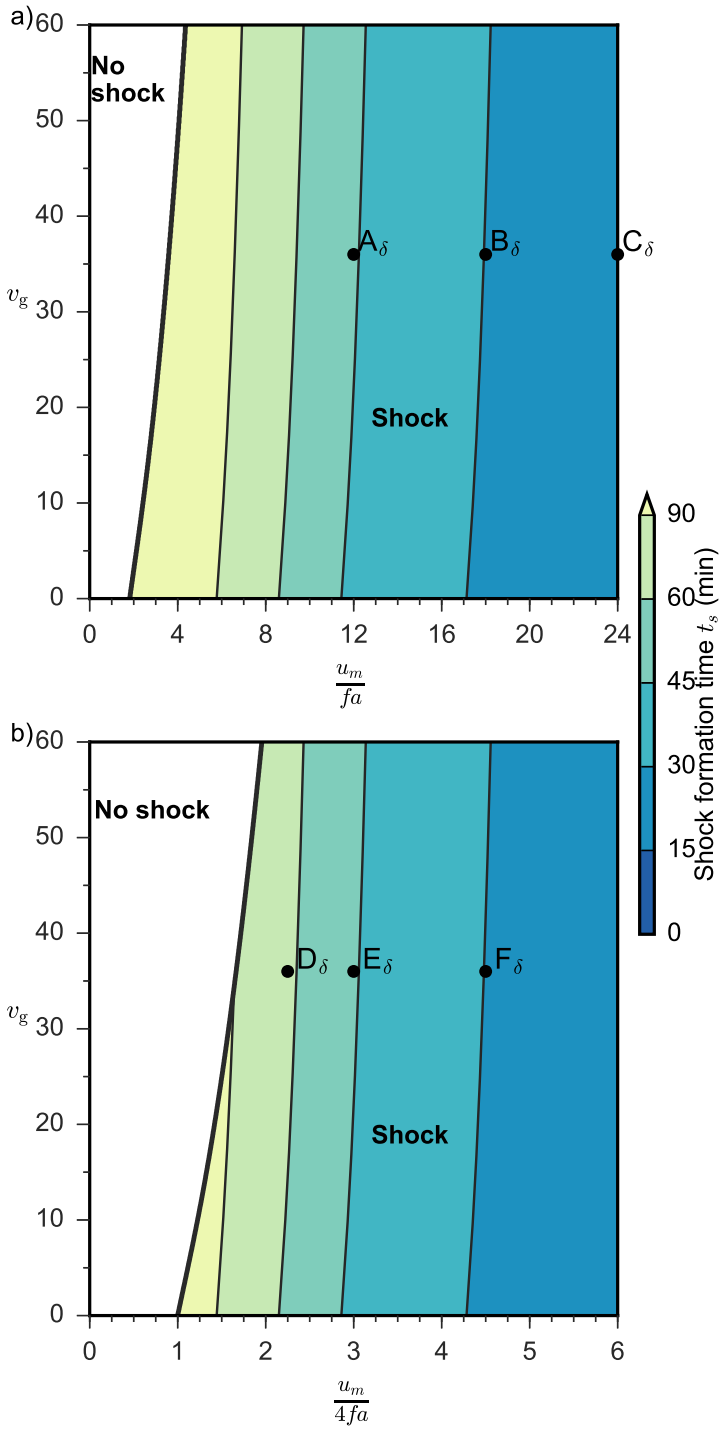

FIG. 3.7. Isolines of the shock formation time t_s (colored shading) and the shock condition (thick curve) for a) the initial divergence cases resulting in triangular waves, as described by equations (3.63) and (3.66) and b) the initial divergence cases resulting in N-waves, as described by equations (3.76) and (3.79). The abscissa in each panel is a dimensionless measure of the maximum initial convergence. The points A_δ, B_δ, and C_δ in the upper panel correspond to the three columns in Fig. 3.8, while the points D_δ, E_δ, and F_δ in the lower panel correspond to the three columns in Fig. 3.10.

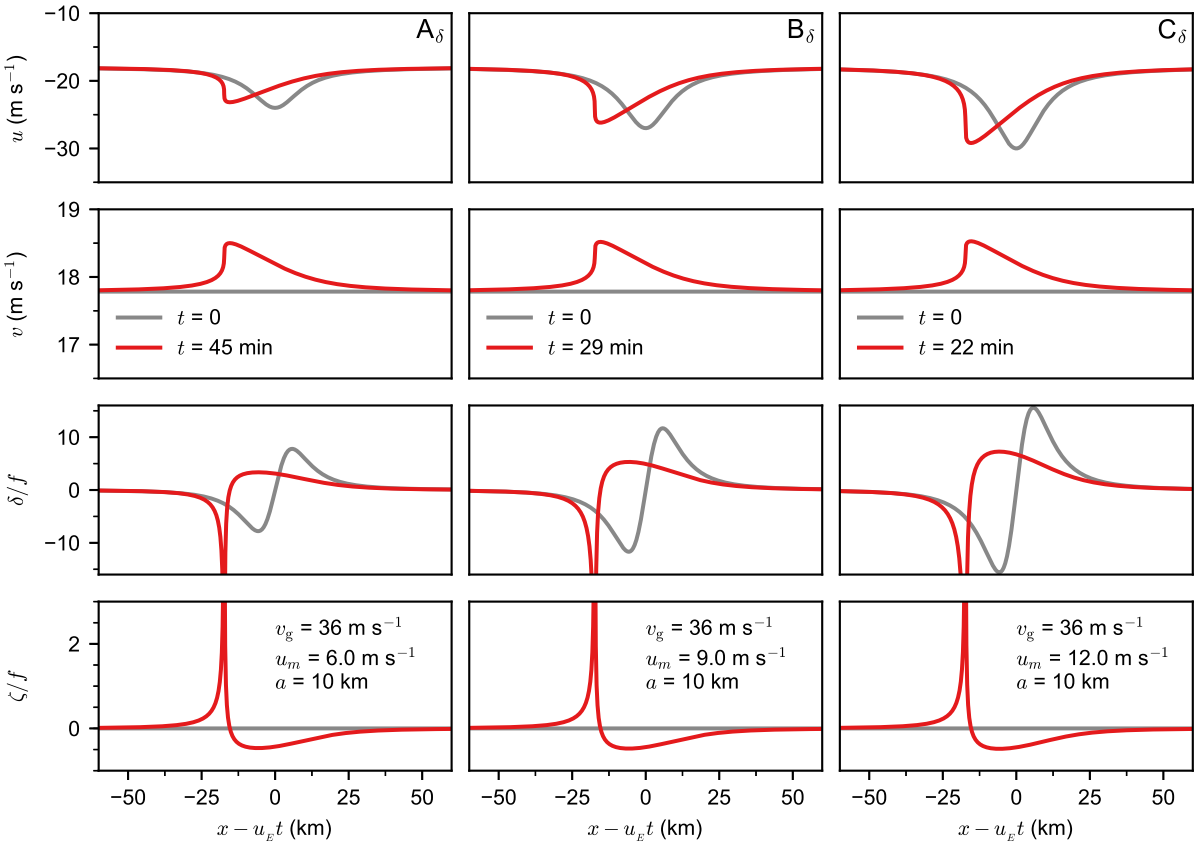

FIG. 3.8. The three columns show three examples with initial divergence only, as determined by the analytical solutions (3.56)–(3.60). All three lead to the formation of triangular waves in u and v. The spatial distributions at $t = 0$ are shown by the gray curves, while the distributions at shock formation time are shown by the red curves. All three cases have $v_g = 36$ m s^{-1}, $a = 10$ km, and the same initial $v_0(x) = v_E = 17.8$ m s^{-1}, so that the initial vorticity is zero. These three examples correspond to the three points labeled A$_\delta$,B$_\delta$, and C$_\delta$ in the top panel of Fig. 3.7.

$$v(x,t) = v_E - v_m \left(\frac{1}{1+(\hat{x}/b)^2} \right) e^{-kt} \cos(ft), \tag{3.83}$$

while the characteristic equation (3.46) simplifies to

$$x = \hat{x} + u_E t - v_m \left(\frac{1}{1+(\hat{x}/b)^2} \right) t_2(t). \tag{3.84}$$

The solutions (3.50) and (3.51) for the divergence and vorticity become

$$\delta(x,t) = \frac{\zeta_0(\hat{x}) e^{-kt} \sin(ft)}{1 + t_2(t)\zeta_0(\hat{x})}, \tag{3.85}$$

$$\zeta(x,t) = \frac{\zeta_0(\hat{x}) e^{-kt} \cos(ft)}{1 + t_2(t)\zeta_0(\hat{x})}, \tag{3.86}$$

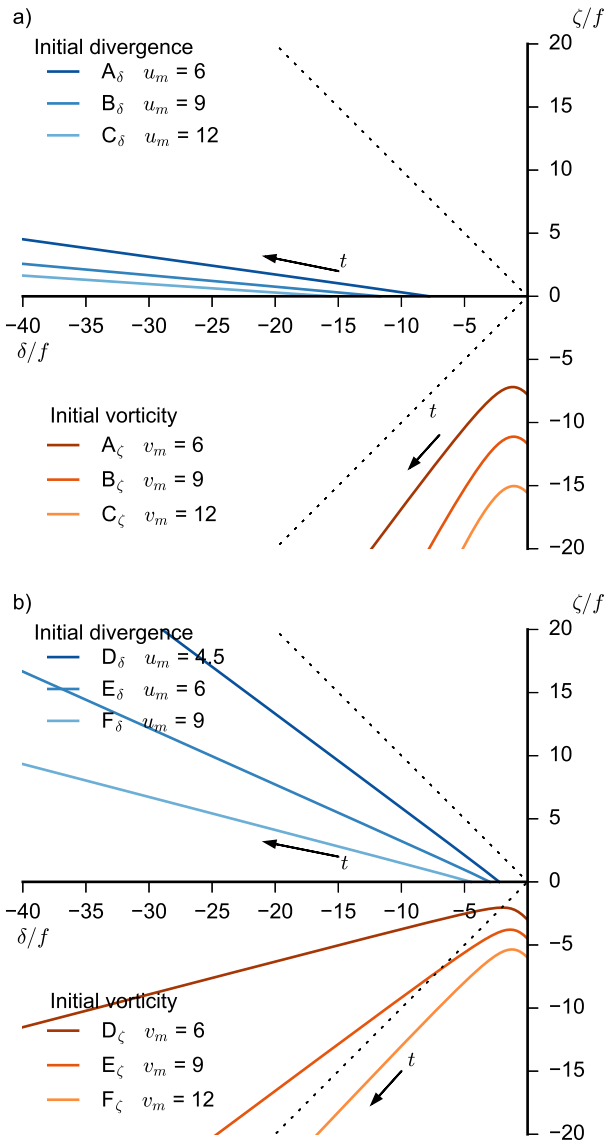

FIG. 3.9. Time evolution of the vorticity and divergence along the first shock-producing characteristics for the triangular waves (upper panel) and for the N-waves (lower panel). The bluish curves are initialized with $\zeta = 0$ and $\delta \neq 0$, while the reddish curves are initialized with $\delta = 0$ and $\zeta \neq 0$. The direction of increasing time is indicated by the arrows. The dashed lines are defined by $|\zeta| = |\delta|$. In the upper panel, the three cases A_δ, B_δ, and C_δ are divergence preferred triangular waves, while the three cases A_ζ, B_ζ, and C_ζ are vorticity preferred triangular waves. In the lower panel, the four cases D_δ, E_δ, F_δ, and D_ζ are divergence-preferred N-waves, while E_ζ and F_ζ are N-waves with nearly the same magnitude in the singularities of δ and ζ.

so that (3.52) becomes

$$\left(\frac{\delta^2(x,t)+\zeta^2(x,t)}{\zeta_0^2(\hat{x})}\right)^{1/2} = \frac{e^{-kt}}{1+t_2(t)\zeta_0(\hat{x})}. \tag{3.87}$$

From (3.85) and (3.86) or (3.87), we see that shock formation occurs along the characteristic $\hat{x}$ when the denominator becomes zero, i.e., $t_2(t)\zeta_0(\hat{x}) = -1$. This occurs first along the characteristic with the

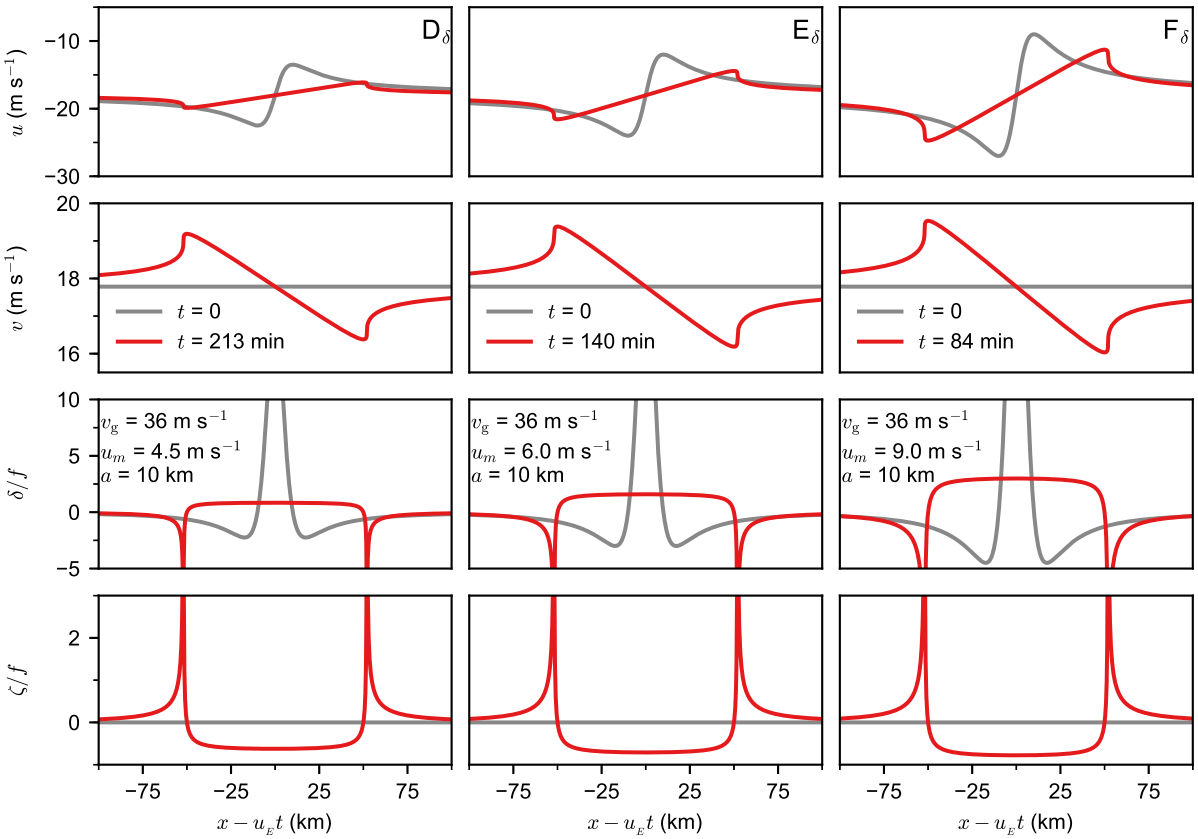

FIG. 3.10. The three columns show three examples with initial divergence only, as determined by the analytical solutions (3.69)–(3.73). All three lead to the formation of N-waves in u and v. The spatial distributions at $t = 0$ are shown by the gray curves, while the distributions at shock formation time are shown by the red curves. All three cases have $v_g = 36$ m s^{-1}, $a = 10$ km, and the same initial $v_0(x) = v_E = 17.8$ m s^{-1}, so that the initial vorticity is zero. These three examples correspond to the three points labeled D$_\delta$, E$_\delta$, and F$_\delta$ in the bottom panel of Fig. 3.7.

minimum value of $\zeta_0(\hat{x})$. For this example, the minimum value of $\zeta_0(\hat{x})$ occurs at $\hat{x} = -b/\sqrt{3} \equiv \hat{x}_s$ so that, from (3.81), $\min[\zeta_0(\hat{x})] = \zeta_0(\hat{x}_s) = -(3\sqrt{3}/8)(v_m/b)$. Application of (3.87) along the characteristic $\hat{x} = \hat{x}_s$ yields

$$\left(\frac{\delta^2(x,t)+\zeta^2(x,t)}{\zeta_0^2(\hat{x}_s)}\right)^{1/2} = \frac{e^{-kt}}{1-(3\sqrt{3}/8)(v_m/b)t_2(t)}. \tag{3.88}$$

Thus, the shock formation time t_s is given implicitly by

$$t_2(t_s) = \frac{8\sqrt{3}}{9}\frac{b}{v_m} \approx 1.54\frac{b}{v_m}, \tag{3.89}$$

and, from (3.84), the position of shock formation is

$$x_s = u_E t_s - \sqrt{3}b. \tag{3.90}$$

From Fig. 3.6, note that (3.89) has a solution only when $(8\sqrt{3}/9)(b/\upsilon_m)$ is smaller than the maximum value of $t_2(t)$. The maximum value of $t_2(t)$ occurs at $t=\pi/f\approx 17.46$ h and, from (3.48), has the value

$$\max[t_2(t)]=\frac{f+f\exp[-\pi(k/f)]}{f^2+k^2}. \tag{3.91}$$

The condition for shock formation is

$$\frac{\upsilon_m}{f\,b}>\left(\frac{\upsilon_m}{f\,b}\right)_c\equiv\frac{8\sqrt{3}}{9}\left(\frac{1+(k/f)^2}{1+\exp[-\pi(k/f)]}\right). \tag{3.92}$$

Equations (3.89) and (3.92) have been used to construct the top panel of Fig. 3.11, which shows isolines of the shock formation time t_s and the shock critical condition (thick curve) in the $(\upsilon_m/f\,b,\upsilon_g)$ plane. There is only a weak dependence of t_s on υ_g.

The solutions for $u,\upsilon,\delta/f$, and ζ/f, as given by (3.82)–(3.86), are plotted in Fig. 3.12 for the constants $\upsilon_g=36$ m s^{-1}, $b=10$ km, and $\upsilon_m=6,9,12$ m s^{-1} for cases A_ζ, B_ζ and C_ζ. The plots cover the spatial interval $-80\le x\le 80$ km and are for $t=0$ and $t=t_s$, where $t_s=3.5,2.7,2.3$ h is the shock formation time for each initial condition.

The time evolution of the divergence and vorticity along the first shock-producing characteristic is shown by the reddish curves in the top panel of Fig. 3.9. Note that from (3.85) and (3.86) that $\delta/\zeta=\tan(f\,t)$, so that the shock is vorticity-preferred if $0<f\,t_s<\pi/4$ and is divergence-preferred if $\pi/4<f\,t_s<\pi/2$. A_ζ, B_ζ and C_ζ fall in the former range and are vorticity-preferred triangular waves.

For the second set of simple examples for flow with initial vorticity, we consider the formation of an N-wave with the initial conditions

$$u_0(x)=u_{_E}\quad\text{and}\quad\upsilon_0(x)=\upsilon_{_E}+\upsilon_m\left(\frac{2x/b}{1+(x/b)^2}\right), \tag{3.93}$$

where the constants b and υ_m now specify the horizontal extent and strength of this initial anti-symmetric rotational flow anomaly. The initial divergence and vorticity associated with (3.93) are

$$\delta_0(x)=0\quad\text{and}\quad\zeta_0(x)=\frac{2\upsilon_m}{b}\left(\frac{2x/b}{[1+(x/b)^2]^2}\right). \tag{3.94}$$

We assume $v_m > 0$, so that negative initial vorticity appears on the winds of a central region of positive vorticity. With these initial conditions, the solutions (3.44) and (3.45) simplify to

$$u(x,t) = u_E + v_m \left(\frac{2\hat{x}/b}{1+(\hat{x}/b)^2} \right) e^{-kt} \sin(ft), \tag{3.95}$$

$$v(x,t) = v_E + v_m \left(\frac{2\hat{x}/b}{1+(\hat{x}/b)^2} \right) e^{-kt} \cos(ft), \tag{3.96}$$

while the characteristic equation (3.46) simplifies to

$$x = \hat{x} + u_E t + v_m \left(\frac{2\hat{x}/b}{1+(\hat{x}/b)^2} \right) t_2(t). \tag{3.97}$$

The solutions (3.50) and (3.51) for the divergence and vorticity become

$$\delta(x,t) = \frac{\zeta_0(\hat{x}) e^{-kt} \sin(ft)}{1 + t_2(t)\zeta_0(\hat{x})}, \tag{3.98}$$

$$\zeta(x,t) = \frac{\zeta_0(\hat{x}) e^{-kt} \cos(ft)}{1 + t_2(t)\zeta_0(\hat{x})}, \tag{3.99}$$

so that (3.52) becomes

$$\left(\frac{\delta^2(x,t) + \zeta^2(x,t)}{\zeta_0^2(\hat{x})} \right)^{1/2} = \frac{e^{-kt}}{1 + t_2(t)\zeta_0(\hat{x})}. \tag{3.100}$$

From (3.98) and (3.99) or (3.100), shock formation occurs along a characteristic $\hat{x}$ when $t_2(t)\zeta_0(\hat{x}) = -1$. This occurs first along the two characteristics with the minimum value of the initial vorticity $\zeta_0(\hat{x})$. For this example, the two minimum values of $\zeta_0(\hat{x})$ occur at $\hat{x} = \pm\sqrt{3}b$, so that, from (3.94), $\min[\zeta_0(\hat{x})] = -v_m/4b$. Application of (3.100) along the two characteristics $\hat{x} = \pm\hat{x}_s$, where $\hat{x}_s = \sqrt{3}b$, yields

$$\left(\frac{\delta^2(x,t) + \zeta^2(x,t)}{\zeta_0^2(\pm\hat{x}_s)} \right)^{1/2} = \frac{e^{-kt}}{1 - (v_m/4b)t_2(t)}. \tag{3.101}$$

The shock formation time t_s is given implicitly by

$$t_2(t_s) = \frac{4b}{v_m}, \tag{3.102}$$

and, from (3.97), the positions of shock formation are

$$x_s = u_E t_s \pm 3\sqrt{3}b. \tag{3.103}$$

From Fig. 3.6, note that (3.102) has a solution only when $4b/v_m$ is smaller than the maximum value of $t_2(t)$. The maximum value of $t_2(t)$ occurs at $t = \pi/f \approx 17.46$ h and from (3.48), has the value

$$\max[t_2(t)] = \frac{f + f\exp[-\pi(k/f)]}{f^2 + k^2}. \tag{3.104}$$

Thus, the condition for shock formation is

$$\frac{v_m}{4fb} > \left(\frac{v_m}{4fb}\right)_c \equiv \frac{1 + (k/f)^2}{1 + \exp[-\pi(k/f)]}. \tag{3.105}$$

Isolines of the shock formation time t_s, as given implicitly by (3.102), and the shock condition, as given by (3.103), are shown in the bottom panel of Fig. 3.11. The solutions for $u, v, \delta/f$, and ζ/f, as given by (3.95)–(3.99), are plotted in Fig. 3.13, using the constants $v_g = 36$ m s^{-1}, $b = 10$ km, and $v_m = 6, 9, 12$ m s^{-1} for cases D_ζ, E_ζ, and F_ζ. The time evolution of the divergence and vorticity along the first shock-producing characteristic is shown by the reddish curves in the top panel of Fig. 3.9. D_ζ is a divergence-preferred N-wave and E_ζ, and F_ζ have nearly the same magnitude in the singularities of δ and ζ.

3.3 Development of a local model

In this section, we return to the axisymmetric, slab boundary layer equations under a specified pressure field. We develop two local, steady-state models that are approximations of the original set of equations. The first, Local Model 1 (LM1), neglects the local time derivative ($\partial/\partial t$) terms, the horizontal diffusion terms, and the vertical advection w^- terms as well as making selective use of the gradient balance approximation. The second, Local Model 2 (LM2), is a further approximation of LM1. In LM2, we neglect the surface drag terms in the radial momentum equation, so that the boundary layer wind becomes the same as the gradient wind in the layer above the boundary layer. LM2 is essentially the same boundary layer model used by Ooyama (1969a).

First estimates of the axisymmetric flow in the boundary layer of a stationary tropical cyclone can be obtained by considering local approximations of the slab boundary layer equations (3.1) and (3.2). The following two subsections consider two different local approximations, designated LM1 and LM2

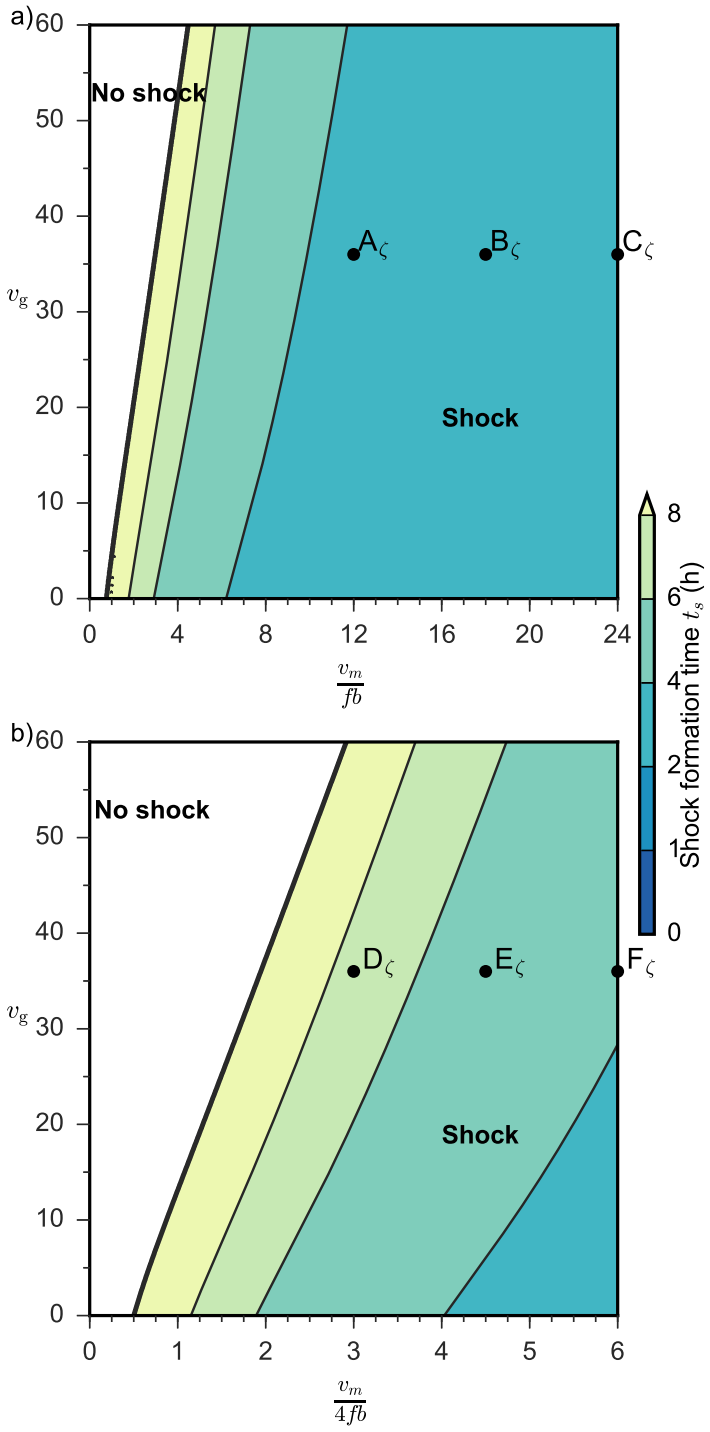

FIG. 3.11. Isolines of the shock formation time t_s (colored shading) and the shock condition (thick curve) for a) the initial vorticity cases resulting in triangular waves, as described by equations (3.89) and (3.92) and b) the initial vorticity cases resulting in N-waves, as described by equations (3.102) and (3.105). The abscissa in each panel is a dimensionless measure of the maximum initial vorticity. The points A_ζ, B_ζ, and C_ζ in the upper panel correspond to the three columns in Fig. 3.12, while the points D_ζ, E_ζ, and F_ζ in the lower panel correspond to the three columns in Fig. 3.13.

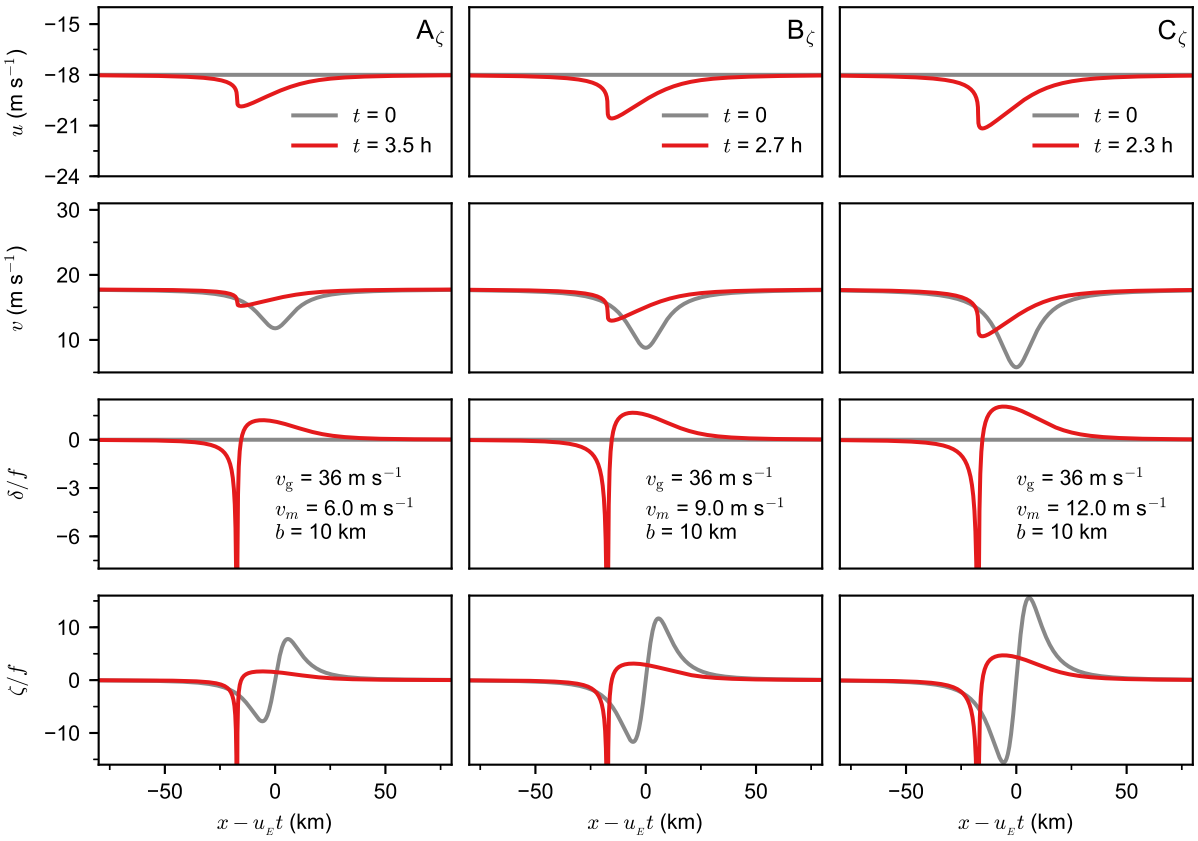

FIG. 3.12. The three columns show three examples with initial vorticity only, as determined by the analytical solutions (3.82)–(3.86). All three lead to the formation of triangular waves. The spatial distributions at $t = 0$ are shown by the gray curves, while the distributions at shock formation time are shown by the red curves. All three cases have $v_g = 36$ m s^{-1}, $b = 10$ km, and the same initial $u_0(x) = u_E = -18$ m s^{-1}, so that the initial divergence is zero. These three examples correspond to the three points labeled A$_\zeta$, B$_\zeta$, and C$_\zeta$ in the top panel of Fig. 3.11.

using the approximations outlined above to the boundary layer equations (3.1) and (3.2). The resulting equations can then be written in the form

$$u\frac{\partial u}{\partial r} - (f+\zeta)v + \frac{\partial}{\partial r}\left(\frac{p}{\rho} + \tfrac{1}{2}v^2\right) = -\frac{c_D U}{h}u, \tag{3.106}$$

$$(f+\zeta)u = -\frac{c_D U}{h}v, \tag{3.107}$$

where the boundary layer relative vorticity is defined by

$$\zeta = \frac{\partial(rv)}{r\,\partial r}. \tag{3.108}$$

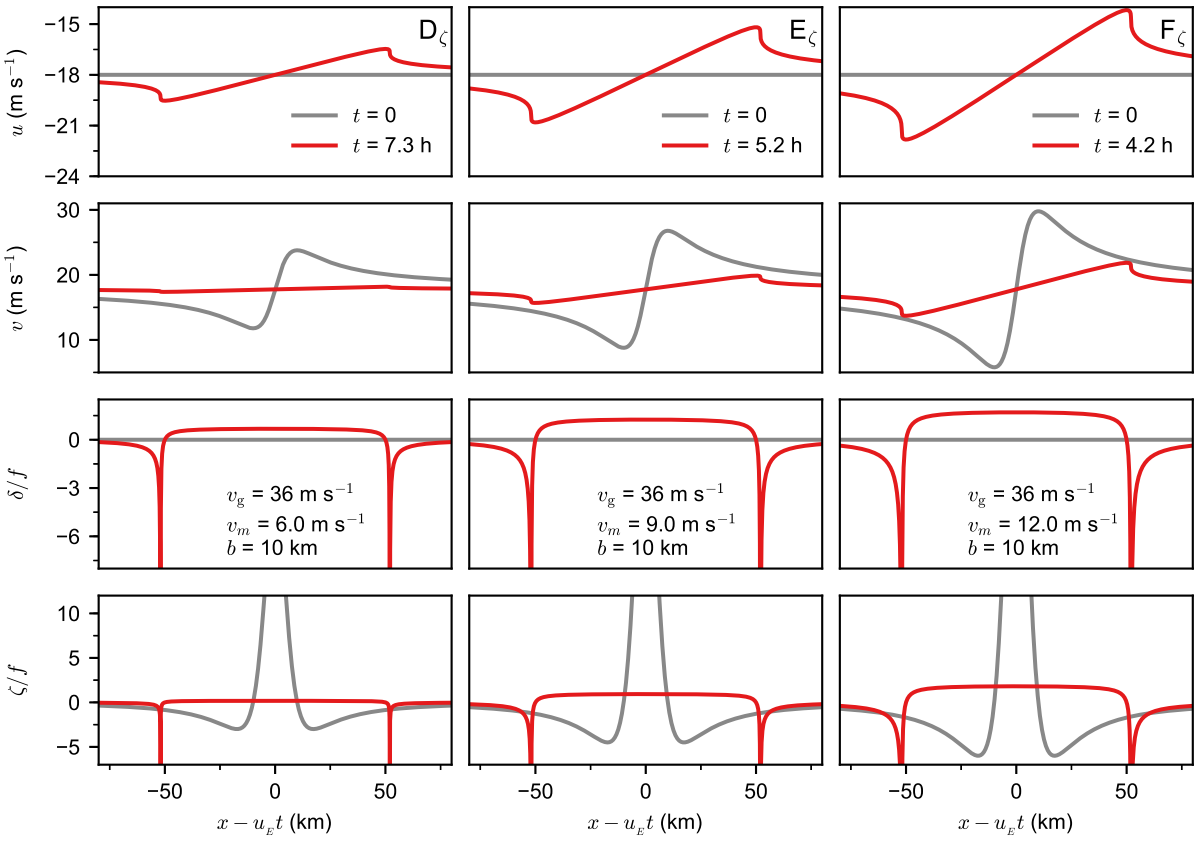

FIG. 3.13. The three columns show three examples with initial vorticity only, as determined by the analytical solutions (3.95)–(3.99). The spatial distributions at $t = 0$ are shown by the gray curves, while the distributions at shock formation time are shown by the red curves. All three cases have $v_g = 36$ m s^{-1}, $a = 10$ km, and the same initial $u_0(x) = u_E = 18$ m s^{-1}, so that the initial divergence is zero. These three examples correspond to the three points labeled D$_\zeta$, E$_\zeta$, and F$_\zeta$ in the top panel of Fig. 3.11.

Next, $f+\zeta$ is approximated by $f+\zeta_{\rm gr}$ and $(p/\rho)+1/2v^2$ by $(p/\rho)+1/2v_{\rm gr}^2$ to obtain

$$u\frac{\partial u}{\partial r} - (f+\zeta_{\rm gr})v + c_D U\frac{u}{h} = -(f+\zeta_{\rm gr})v_{\rm gr}, \tag{3.109}$$

$$(f+\zeta_{\rm gr})u + c_D U\frac{v}{h} = 0, \tag{3.110}$$

where the relative vorticity of the gradient wind is

$$\zeta_{\rm gr} = \frac{\partial(r v_{\rm gr})}{r\,\partial r}. \tag{3.111}$$

From this point in the derivation, the following steps are taken to provide the equations for LM1 and LM2.

3.3.1 Local model 1 (LM1)

The final step to derive LM1 is to neglect the $u(\partial u/\partial r)$ term in (3.109). By removing this nonlinear term, the resulting equations for LM1 are

$$-(f+\zeta_{\mathrm{gr}})v+\left(\frac{c_{_D}k(u^2+v^2)^{1/2}}{h}\right)u=-(f+\zeta_{\mathrm{gr}})v_{\mathrm{gr}}, \tag{3.112}$$

$$(f+\zeta_{\mathrm{gr}})u+\left(\frac{c_{_D}k(u^2+v^2)^{1/2}}{h}\right)v=0. \tag{3.113}$$

Given a radial profile $v_{\mathrm{gr}}(r)$ and its associated $\zeta_{\mathrm{gr}}(r)$, we can solve the above equations for u and v at each point.

The "solution" of this system of equations is

$$u=-\left(\frac{E}{1+E^2}\right)v_{\mathrm{gr}}, \qquad v=\left(\frac{1}{1+E^2}\right)v_{\mathrm{gr}}, \tag{3.114}$$

where the Ekman number is defined by

$$E=\frac{c_{_D}U}{h(f+\zeta_{\mathrm{gr}})}=\frac{c_{_D}k(u^2+v^2)^{1/2}}{h(f+\zeta_{\mathrm{gr}})}. \tag{3.115}$$

The Ekman number is the ratio of the characteristic value of the drag term, $c_{_D}U^2/h$, to the characteristic value of the rotational term, $(f+\zeta_{\mathrm{gr}})U$. This matches the standard definition of the Ekman number with three main differences: the slab boundary layer depth h is used instead of the characteristic vertical depth scale, the absolute vorticity $f+\zeta_{\mathrm{gr}}$ is used instead of just the planetary component, and E is unknown because of the dependence on u and v.

It is important to note that (3.114) is not an explicit solution of the nonlinear equations. Because of the dependence of E on the u and v, (3.114) are implicit relations for u and v in terms of the specified forcing v_{gr}. However, we can make progress by taking the sum of the squares of the two equations in (3.114), thereby obtaining

$$u^2+v^2=\left(\frac{1}{1+E^2}\right)v_{\mathrm{gr}}^2. \tag{3.116}$$

After rearranging, (3.116) can be written in the form

$$E^4+E^2-E_{\mathrm{f}}^2=0, \tag{3.117}$$

where $E_{\rm f}$ is the "forced Ekman number" and is defined by

$$E_{\rm f} = \frac{c_{_D}\, k v_{\rm gr}}{h(f+\zeta_{\rm gr})}. \tag{3.118}$$

Solving (3.117) as a quadratic equation for E^2 and choosing the physically relevant root yields

$$E = \left[\left(\frac{1}{4} + E_{\rm f}^2\right)^{1/2} - \frac{1}{2}\right]^{1/2}. \tag{3.119}$$

If $c_{_D}$ were considered to be a constant, an assumption that is not unreasonable given relatively constant values are used in other modeling studies (e.g., Bryan 2012; Bryan et al. 2017), then $E_{\rm f}$ could be considered as specified, and (3.119) would constitute an explicit solution for the Ekman number E. It should be noted that in the results presented here, we are considering $c_{_D}$ to be dependent on U, as parameterized by (3.5). Then, equations (3.5), (3.115), (3.118), and (3.119) must be iteratively solved to obtain E, $E_{\rm f}$, $c_{_D}$, and U, after which u and v can be calculated from (3.114). After solving for E, the flow direction can be found as follows. Defining θ as the inflow angle relative to the azimuthal direction, we can write $\theta = \tan^{-1}(-u/v)$, or

$$\theta = \tan^{-1} E, \tag{3.120}$$

which follows from the use of (3.114). The orange curve in Fig. 3.14 shows E as a function of $E_{\rm f}$, with corresponding values of the inflow angle θ at 5° intervals, as indicated by the dots. Since (3.115) and (3.118) imply that

$$\frac{E}{E_{\rm f}} = \frac{(u^2+v^2)^{1/2}}{v_{\rm gr}}, \tag{3.121}$$

and since the orange curve in Fig. 3.14 falls below the diagonal line $E = E_{\rm f}$, the LM1 solutions obey the inequality $(u^2+v^2)^{1/2} < v_{\rm gr}$, as can also be seen from (3.116). However, as $E_{\rm f} \to 0$, we have $E \to E_{\rm f}$ for the LM1 solutions. As an example, the point corresponding to $\theta = 15°$ on the orange curve has the value $E/E_{\rm f} = 0.966$, so that $(u^2+v^2)^{1/2} \approx v_{\rm gr}$ to within an accuracy of 3.4%.

3.3.2 Local model 2 (LM2)

Looking at the boundary layer portion of Ooyama (1969a), we see that it is a further approximation of (3.113). The surface drag term in the first line of (3.113) is neglected, so that $v = v_{\rm gr}$. The surface drag term in the second line of (3.113) is approximated by $(k c_{_D} v_{\rm gr}/h)v$, so that the LM2 version of (3.114) is

$$u = -E_{\rm f} v_{\rm gr}, \quad v = v_{\rm gr}, \tag{3.122}$$

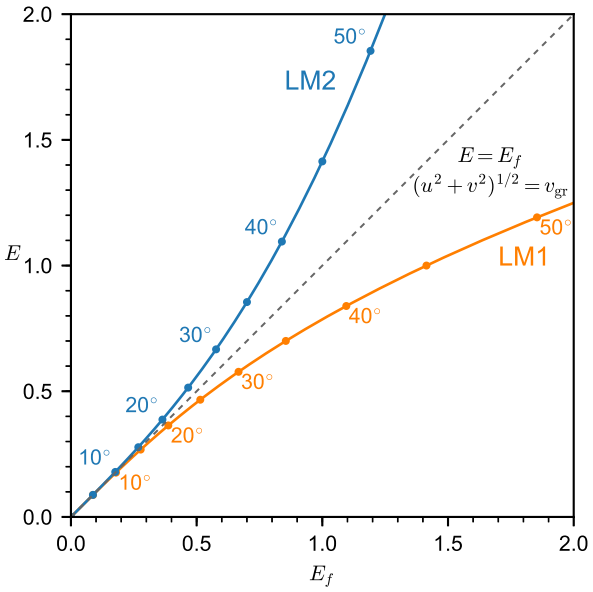

FIG. 3.14. The Ekman number E as a function of the "forced Ekman number" E_f, as determined from (3.119) for LM1 and from (3.124) for LM2. The dots along the two curves give the inflow angle θ (every 5°) relative to the azimuthal direction, as determined by (3.120) for LM1 and by (3.125) for LM2. Note that, for small E_f, the solutions for both LM1 and LM2 approach the diagonal line $E = E_f$.

where E_f is again defined by (3.118). Taking the sum of the squares of the two equations in (3.122), we obtain

$$u^2 + v^2 = \left(1 + E_f^2\right) v_{gr}^2. \tag{3.123}$$

After rearrangement, (3.123) can be written in the form

$$E = E_f \left(1 + E_f^2\right)^{1/2}, \tag{3.124}$$

where E is again defined by (3.115). Again, we define θ as $\tan^{-1}(-u/v)$ as the inflow angle relative to the azimuthal direction and write

$$\theta = \tan^{-1} E_f, \tag{3.125}$$

which follows from the use of (3.122). Equations (3.124) and (3.125) have been used to produce the blue LM2 curve in Fig. 3.14.

As can be seen from Fig. 3.14, the LM1 and LM2 models produce very similar solutions when E_f and E are less than 1/2, but the models produce significantly different solutions when E_f and E exceed unity. Thus, LM2 should be regarded as inaccurate for values of E_f and E exceeding unity. We noted that an interesting feature of these solutions, which can be deduced from (3.116) and (3.123), is that

$u^2+v^2 < v_{gr}^2$ for LM1, while $u^2+v^2 > v_{gr}^2$ for LM2. In other words, for LM1, the boundary layer kinetic energy per unit mass is less than the kinetic energy per unit mass in the overlying fluid. For LM2, the conclusion is just the opposite. However, for E_f and E less than 0.2, both LM1 and LM2 yield $u^2+v^2 \approx v_{gr}^2$ to within a few percent accuracy.

As will be illustrated in greater depth in the next section, E_f and E are less than unity for all radii for many radial profiles of v_{gr}. However, for certain strong vortices, the values of E_f and E can exceed unity at radii just outside the maximum values of v_{gr}. At these radii, the numerator in (3.118) is still relatively large, but the denominator is much reduced (the vorticity skirt effect), so that E_f and E are locally enhanced, leading to large differences between the solutions LM1 and LM2. However, it should be pointed out that a radial profile of $u(\partial u/\partial r)$ is implied at these radii even though this term has been neglected in the local models. Because of the implied $u(\partial u/\partial r)$, if the solution of (3.113) in LM1 and LM2 is to be accepted as a self-consistent approximation of the solution to the original equations (3.1)–(3.5), we must have

$$R = \frac{|u(\partial u/\partial r)|}{(f+\zeta_{gr})v_{gr}} \ll 1, \tag{3.126}$$

where R is the dimensionless ratio. We interpret R as a local Rossby number based on the absolute vorticity of the gradient flow $(f+\zeta_{gr})$ and on the magnitude and radial scale of the boundary layer inflow $u(\partial u/\partial r)$. At radii where R becomes greater than unity, the usefulness of local solutions tends to disappear because the solutions are not self-consistent. In these regions, the hyperbolic nature of the original boundary layer problem (3.1)–(3.5) can come into play and shocks can form.

3.4 Results for a steady forcing

In this section, we will look at the numerical and local model response to a series of forcing profiles from idealized vortex profiles. Some of the profiles exhibit characteristics not frequently observed in tropical cyclones, but the profiles provide context for shock formation. For the forcing profiles, we will use a polynomial vortex defined as

$$v_{gr}(r) = v_{max}\left(\frac{n(r/a)^{n-1}}{1+(n-1)(r/a)^n}\right), \tag{3.127}$$

where the constants v_{max}, a, and n respectively specify the maximum gradient wind, radius of maximum gradient wind, and the shape of the gradient wind profile (larger values of n both increase the

hollowness of the center of the profile and reduce the vorticity skirt outside the radius of maximum wind). The vorticity profile corresponding to this vortex is

$$\zeta_{\rm gr}(r) = -\upsilon_{\rm max}\left(\frac{(n-1)n(r/a)^{n-2}[(r/a)^n-1]}{(r/a)^2\,[1+(n-1)(r/a)^n]^2}\right). \tag{3.128}$$

The slab boundary layer model is solved numerically using centered, second-order spatial finite difference methods on the domain $0 \le r \le 1000$ km with a uniform radial spacing of 100 m and a fourth-order Runge–Kutta time differencing scheme with a time step of 1 s. The forcing illustrates how the boundary layer flow transitions from one quasi-steady state to another in response to the balanced wind field $\upsilon_{\rm gr}(r)$ above the boundary layer. The constants for slab boundary layer model and local models LM1 and LM2 have been chosen as $h = 1000$ m, $f = 5\times10^{-5}$ s^{-1}, and $K = 1500$ m^2 s^{-1}.

Solutions to the slab boundary layer model and local models LM1 and LM2 are presented in Figs. 3.15 and 3.16 with the specified pressure field using the constants for the polynomial vortex shown in Table 3.2. The six rows show plots of the tangential velocity υ, the radial velocity u, the vertical velocity w, the relative vorticity ζ/f, the inflow angel θ, and the dimensionless ratio R. In the weak cases TS1 and TS2 shown in Fig. 3.15, the values for R are less than unity in the eyewall regions. We see that LM1 and LM2 match the magnitude of the inflow in the slab model reasonably well, but do not replicate the jump in the inflow, displace the maximum Ekman pumping $w_{\rm max}$ outside of the radius of maximum tangential wind, and match the spatial extent of the updraft. This result is similar to the experiment done by Ooyama (1969b) as shown by Fig. 3.17. While both local models lack the supergradient winds $\upsilon > \upsilon_{\rm gr}$, LM1 captures the subgradient winds $\upsilon < \upsilon_{\rm gr}$ that are produced by the slab model. Figure 3.16 shows the output for the slab boundary layer model and local models LM1 and LM2 for cases Cat1 and Cat3 from Table 3.2. In this case, R is much larger than unity near the region with the radius of maximum wind and the shock-like structures. While LM1 and LM2 produce unrealistic results for υ, u, and w in this region, outside of that region, R returns to a value less than unity and the local models produce winds close to those of the full slab model.

Motivated by the weak Ekman pumping produced in the TS1 case with the slab model, we run the slab boundary layer and use the polynomial vortex with constant parameters $n = 1, 6, 11$, $4 \le \upsilon_{\rm max} \le 80$ at 2 m s^{-1} intervals, and $10 \le a \le 150$ km at 2 km intervals to assess the changes to the maximum Ekman pumping $w_{\rm max}$ and the maximum agradient tangential flow $(\upsilon - \upsilon_{\rm gr})_{\rm max}$. Figure 3.18 shows contours for $w_{\rm max} = 1, 2, 4, 8, 16, 32$ m s^{-1} and colored shading for $(\upsilon - \upsilon_{\rm gr})_{\rm max}$. The $n = 1$ experiments shown in

TABLE 3.2. The constants v_{max} and a for Figs. 3.15 and 3.16 for different values of n. These cases loosely correspond to characteristic values for weak (TS1) and strong (TS2) tropical storms, and to category 1 and 3 hurricanes.

Case	v_{max} (m s^{-1})	a (km)	n
TS1	20	50	6
TS2	30	40	6
Cat1	40	30	11
Cat3	50	20	11

panel a) have the largest vorticity skirt of the three cases. We see that the boundary layer model struggles to produce large values of w_{max} and lacks large supergradient winds $v > v_{gr}$ with the $n = 1$ forcing profile while panels b) and c) develop Ekman pumping at v_{max} near tropical storm force (17 m s^{-1}) and hurricane force (33 m s^{-1}) winds. While not shown here, a Gaussian vortex containing a hollowness parameter was used to assess whether or not 'U'-shaped wind profiles inside the radius of maximum wind are responsible for the $n = 1$ case struggling to produce Ekman pumping. While hollow vortices will have larger values of $(v - v_{gr})_{max}$ because of the rate by which v_{gr} drops off in the center of the storm and the displacement radially inward of the supergradient winds as illustrated by the top panel of Fig. 3.17, the results for w_{max} and the development of shock-like structures remained unchanged, which suggests that the outer wind structure is critical to this process. This idea is consistent with the ideas presented using the "metaphor" models in which the methods of characteristics are used to find solutions for shocks. With the "metaphor" models, we see the flow of information moves from large radii inward rather than from $r = 0$ outward.

3.5 THE POTENTIAL ROLE OF SHOCKS IN THE EYEWALL REPLACEMENT CYCLE

Using a full-physics modeling simulation, Rozoff et al. (2012) note that v_{gr} expands prior to the formation of a secondary eyewall, a finding supported by observational work (Sitkowski et al. 2011; Didlake and Houze 2011). This expanding wind field is the result of diabatic heating outside of the radius of maximum wind of the primary eyewall as discussed in chapter 2 and by Wang (2009), Hill and Lackmann (2009), and Moon and Nolan (2010). To understand the changes in the inflow during eyewall replacement, Kepert (2013) and Slocum et al. (2014) conducted a series of experiments with a secondary wind maximum in the balanced wind field above the boundary layer. These results show a decrease in the inflow for the primary eyewall as the intensity of the outer eyewall increases. However, these works did not explore an expanding wind field without a secondary maximum to see how the

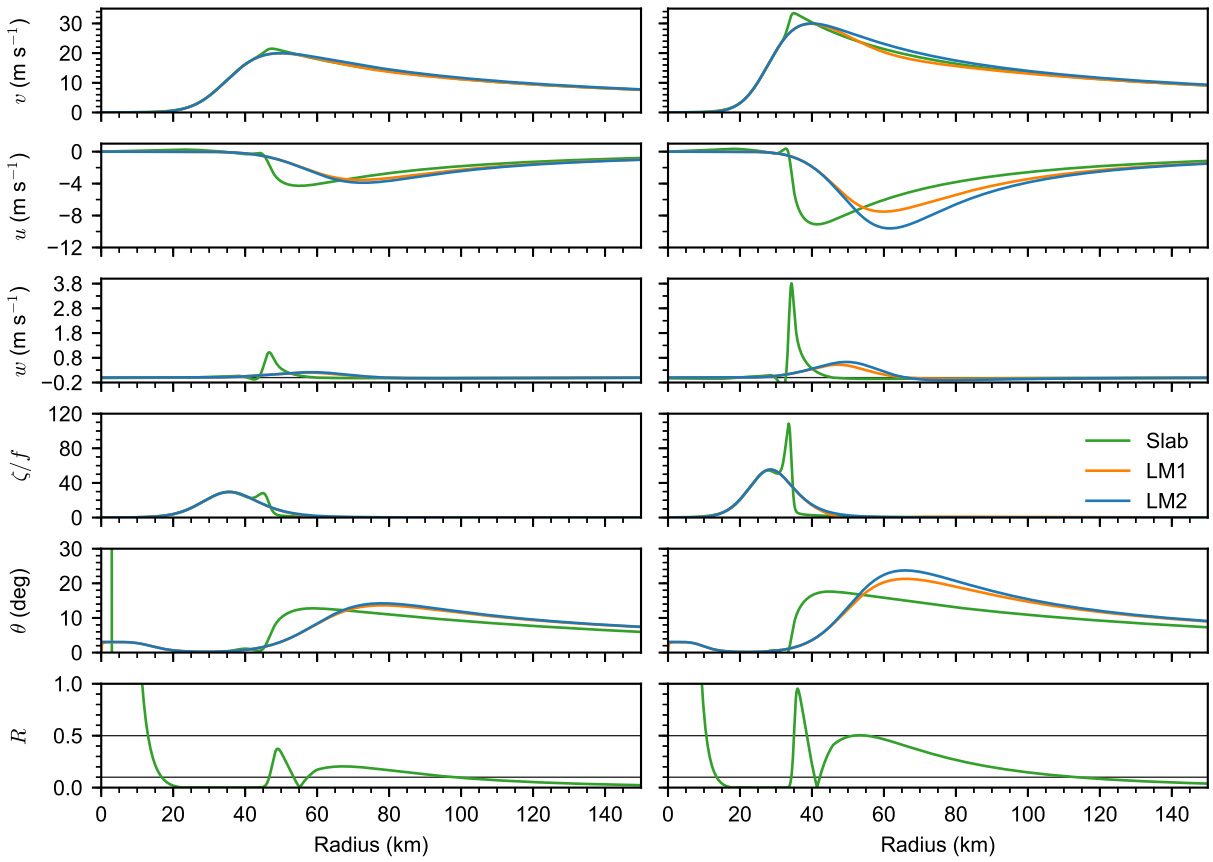

FIG. 3.15. Solutions for the TS1 (left column) and TS2 (right column) vortices listed in Table 3.2 for a polynomial vortex (3.127) with the constants $n = 6$, $\upsilon_{\max} = 20, 30$ m s^{-1}, and $a = 50, 40$ km. The rows in each panel are the tangential velocity υ, the radial velocity u, the vertical velocity w, the relative vorticity ζ/f, the inflow angel θ, and the dimensionless radio R for the slab boundary layer model (green curve) and local models LM1 (orange curve) and LM2 (blue curve).

boundary layer responds to assist with secondary eyewall formation. In the previous section, we see that an expanding wind field without a secondary maximum reduces or hinders large Ekman pumping as shown by the simulations with the polynomial vortex with the constant parameter $n = 1$. As the wind field continues to expand, a secondary inflow maximum should develop. To understand the role of shock dynamics during secondary eyewall formation, we will run a set of experiments in the slab boundary layer model in which we expand the outer wind field. We specify the pressure profile using the double Gaussian vortex

$$\upsilon_{\rm gr}(r) = \frac{\Gamma}{2\pi r}\left[1 - \frac{\gamma\Gamma_1}{\Gamma}\left(1 + h_1\frac{r^2}{a_1^2}\right)e^{-r^2/a_1^2} - \frac{(1-\gamma)\Gamma_2}{\Gamma}\left(1 + h_2\frac{r^2}{a_2^2}\right)e^{-r^2/a_2^2}\right], \tag{3.129}$$

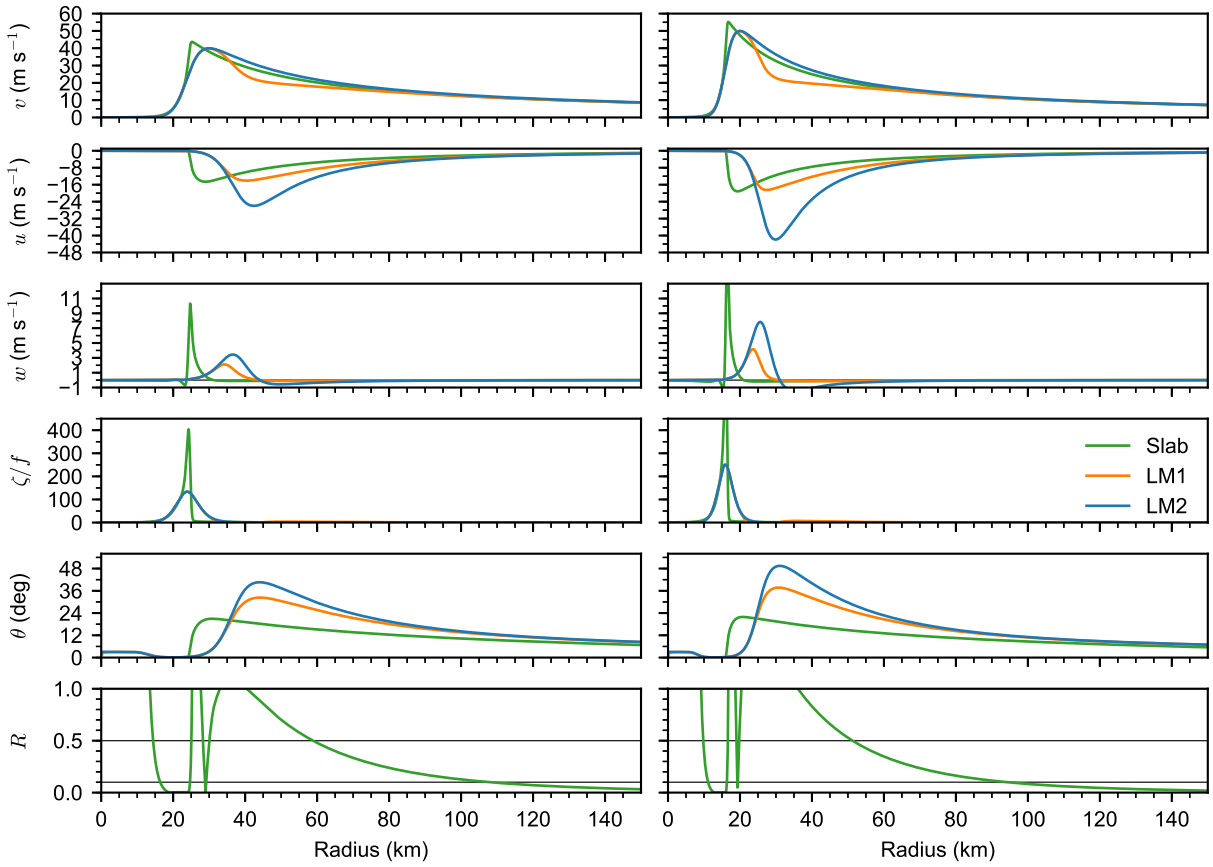

FIG. 3.16. Solutions for the Cat1 (left column) and Cat3 (right column) vortices listed in Table 3.2 for a polynomial vortex (3.127) with the constants $n = 11$, $\upsilon_{\max} = 40, 50$ m s^{-1}, and $a = 30, 20$ km. The rows in each panel are the tangential velocity υ, the radial velocity u, the vertical velocity w, the relative vorticity ζ/f, the inflow angel θ, and the dimensionless radio R for the slab boundary layer model (green curve) and local models LM1 (orange curve) and LM2 (blue curve). Note that the ordinate had a different scale than the ordinate in Fig. 3.15.

where $a_1, a_2, h_1, h_2, \Gamma_1, \Gamma_2$, and γ are constant parameters and $\Gamma = \gamma\Gamma_1 + (1-\gamma)\Gamma_2$. The vorticity associated with (3.129) is

$$\zeta_{\rm gr}(r) = \gamma\zeta_1 + (1-\gamma)\zeta_2 = \frac{\gamma\Gamma_1}{\pi a_1^2}\left(1 - h_1 + h_1\frac{r^2}{a_1^2}\right)e^{-r^2/a_1^2} + \frac{(1-\gamma)\Gamma_2}{\pi a_2^2}\left(1 - h_2 + h_2\frac{r^2}{a_2^2}\right)e^{-r^2/a_2^2}. \qquad (3.130)$$

The slab boundary layer model is configured as discussed in section 3.4. Table 3.3 contains parameters associated with the eyewall replacement cases using (3.129) for the specified pressure forcing $\upsilon_{\rm gr}(r)$ above the boundary layer. In the five experiments, we set $\Gamma_1 = 14 \times 10^6$ m^2 s^{-1} and $\Gamma_2 = \{0, 3.5, 7, 14, 28\} \times 10^6$ m^2 s^{-1} so that we can see how the boundary layer responds to an expanding wind field. Figure 3.19 contains solutions to the slab boundary layer equations using the prescribed parameters. Case A is our control case. With $\Gamma_2 = 0$, the wind field represents the decay rate originating from

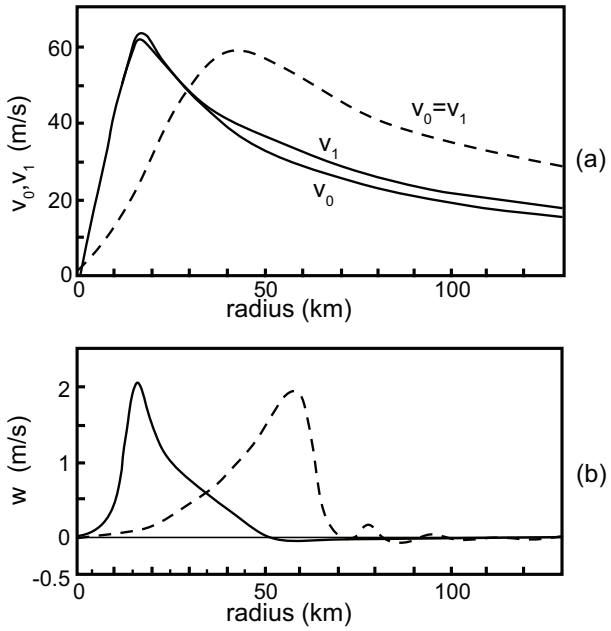

FIG. 3.17. The a) tangential wind υ and b) vertical velocity w output from two versions of the Ooyama (1969a) axisymmetric, three-layer model. The first model has gradient balanced winds in the boundary layer similar to LM2 (dashed curves) and the second model had a more realistic boundary layer formulation (solid curves). v_0 denotes the tangential velocity in the boundary layer and v_2 denotes the tangential velocity in the middle layer. Reproduced from Fig. 2 of Ooyama (1969b).

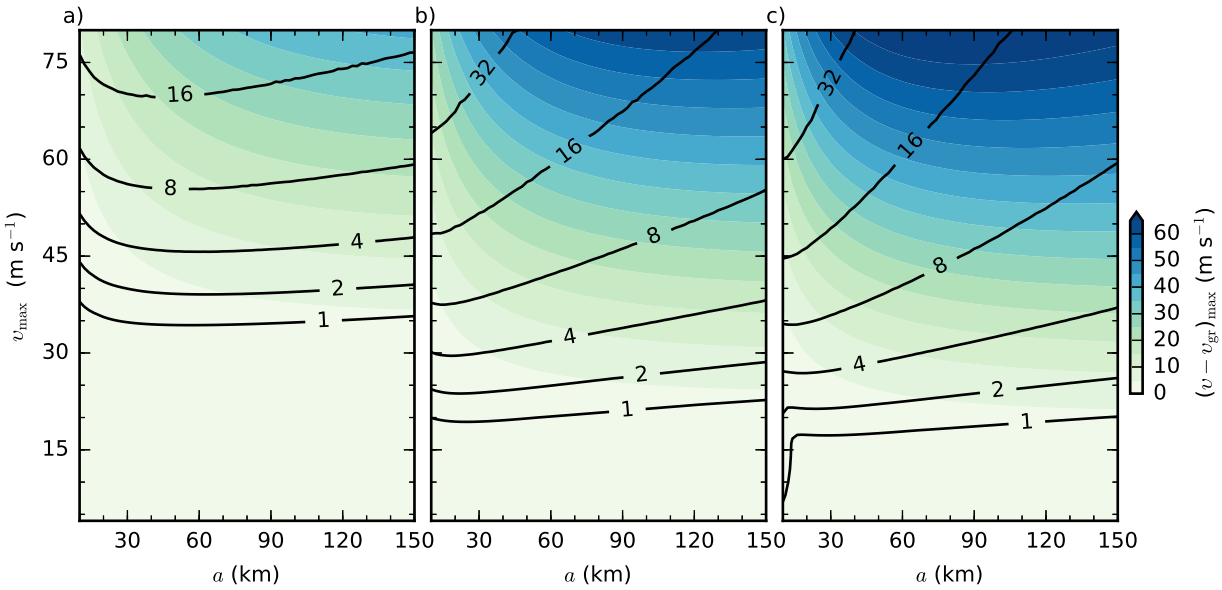

FIG. 3.18. The maximum updraft in black contours for $w_{\max} = 1, 2, 4, 8, 16, 32$ m s^{-1} and maximum agradient tangential flow $(\upsilon - \upsilon_{gr})_{\max}$ in colored shading for individual model runs with υ_{gr} set with the polynomial vortex (3.127) for a) $n = 1$, b) $n = 6$, and c) $n = 11$ where the constant parameters $\upsilon_{\max}$ and a are indicated by the ordinate and the abscissa respectively.

TABLE 3.3. The parameters for the double Gaussian vortex (3.129) used in cases A–E for the slab boundary layer model for the eyewall replacement experiments. a_1 and a_2 determine the horizontal extent of the circulation, h_1 and h_2 control the hollowness of the profile, Γ_1 and Γ_2 are the magnitudes of the circulation, and γ sets the weight given to each vortex. The value of $v_{gr,max}$ and $r_{gr,max}$ are provided for each set of (3.129) parameters.

Case	a_1 (km)	a_2 (km)	h_1	h_2	Γ_1 (10^6 m^2 s^{-1})	Γ_2 (10^6 m^2 s^{-1})	γ	$v_{gr,max}$ (m s^{-1})	$r_{gr,max}$ (km)
A	10	45	0.6	1.0	14	0	0.5	56.0	15.7
B	10	45	0.6	1.0	14	3.5	0.5	56.1	15.7
C	10	45	0.6	1.0	14	7	0.5	56.2	15.8
D	10	45	0.6	1.0	14	14	0.5	56.5	15.9
E	10	45	0.6	1.0	14	28	0.5	57.0	16.0

a single Gaussian vortex. Case E contains a visible secondary bump in $v_{gr}(r)$. This case can be considered to represent the early stages of a secondary eyewall. Cases B and D do not contain any abrupt features that would suggest the development of a secondary maximum in the radial inflow or outer region with Ekman pumping. However, we see that the boundary layer response to an expanding wind field $v_{gr}(r)$ is to cutoff the inflow and reduce the supergradient winds associated with the primary eyewall and create a secondary maximum in v, u, and w that would be associated with the formation of a secondary eyewall.

3.6 DISCUSSION

In this work, we use a series of models to extend our understanding of the role and development of shock-like structures in the tropical cyclone boundary layer. In section 3.2, we develop "metaphor" or "toy" models to look at aspects of the dynamics. In section 3.2.1, we solve the system and examine the role of the drag coefficient by using the method of characteristics after neglecting the horizontal diffusion terms, w^- terms, and the agradient tangential flow $(v - v_{gr})$ terms. We also see that given certain initial radial wind profiles, shocks may fail to form. Since the analytic model lacks several key characteristics of real tropical cyclones, we proceed to a second series of "metaphor" or "toy" models in section 3.2.2 where we use the line-symmetric slab boundary equations to allow us to keep the agradient tangential flow $(v - v_{gr})$ terms while continuing to neglect the horizontal diffusion terms and w^- terms. Although the models lack important curvature effects that are present in the axisymmetric formulation, the line-symmetric model helps us to explore analytic solutions that allow for the formation of triangular waves and N-waves.

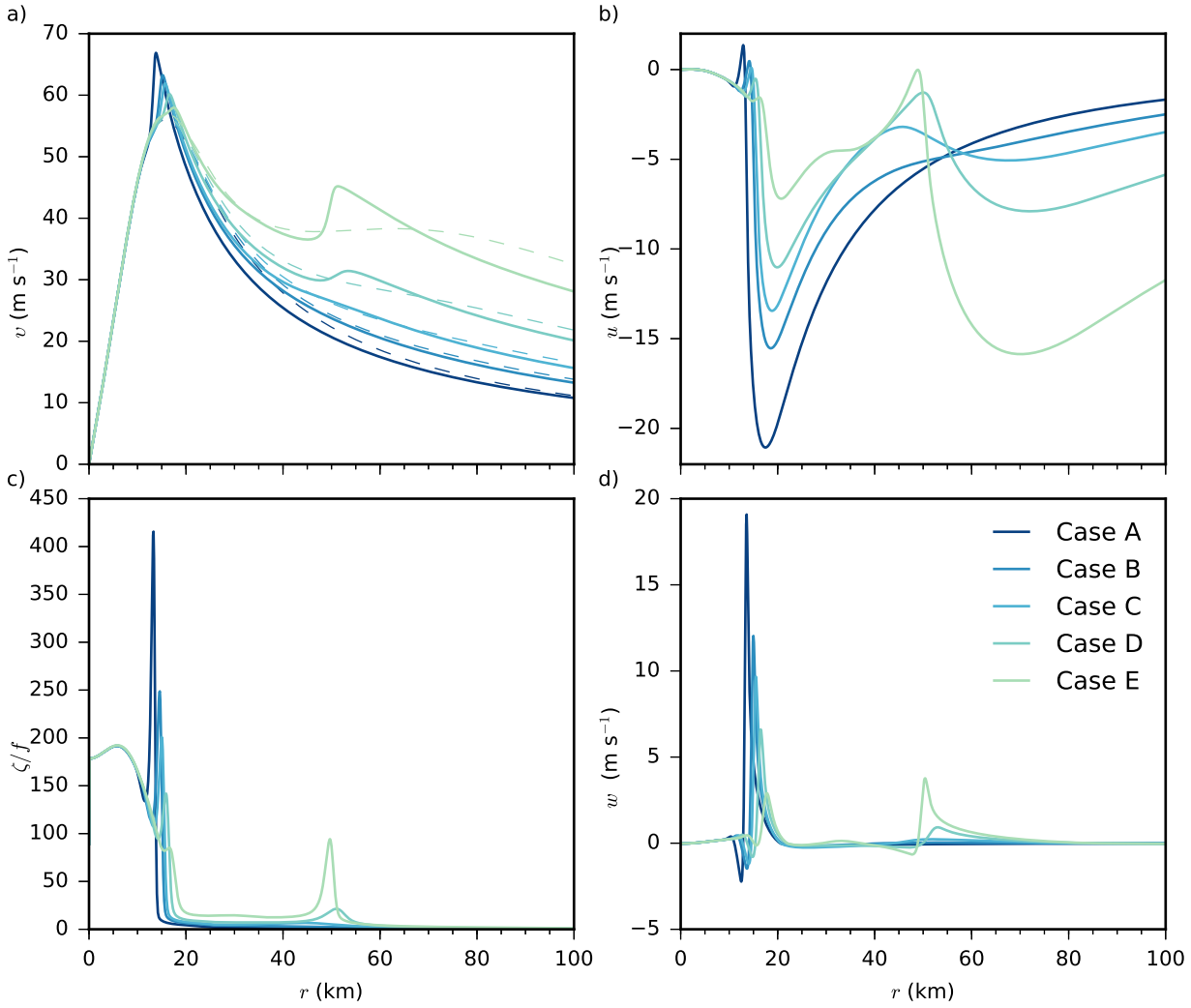

FIG. 3.19. Solutions to cases A–E in Table 3.3 for initial profiles generated with (3.129) where the value of $\Gamma_1 = 14\times10^6$ m^2 s^{-1} and $\Gamma_2 = \{0, 3.5, 7, 14, 28\}\times10^6$ m^2 s^{-1}. The solutions for a) the tangential wind v, b) radial wind u, c) relative vorticity ζ/f, and d) vertical velocity w are for a time after the boundary layer has reached a quasi-steady state with v_{gr}. The dashed curves in panel a) are the specified $v_{gr}(r)$.

Returning to the slab boundary layer model equations in sections 3.3and 3.4, we develop two local, steady-state models that neglect the local time derivative $(\partial/\partial t)$ terms, the horizontal diffusion terms, and the vertical advection w^- terms as well as making selective use of the gradient balance approximation. From these local models, we see that these simplifications are reasonable first approximations of the axisymmetric, boundary layer flow for weak, broad tropical cyclones and for radii where the ratio of the gradient flow and magnitude and radial scale of the boundary layer inflow is small ensuring that the solutions are self-consistent. The results concur that the suggestion regarding a linearized set of

boundary layer equations in Kepert (2001) is right under specific circumstances. The slab model results with the steady-state forcing shown in section 3.4 indicate that the role of the nonlinear term in the radial momentum equation is highly dependent on intensity and the decay rate of the tangential wind (e.g., the extent of the vorticity skirt). While both storms are of similar intensity, this idea appears to be consistent with what is shown by the aircraft reconnaissance data in Fig. 3.1. Hurricane Allen (1980) has a larger radius of maximum tangential wind and extent to the wind field than the Hurricane Hugo (1989) data. The result is a broad region of inflow that does not have as sharp of a jump. It appears that the nonlinear terms are vital to organizing the eyewall convection as the storm intensity nears hurricane force. In other words, the result suggests that the boundary layer plays a limited role in storm organization during the early incipient or incubation phase of the "life cycle" of the tropical cyclone. However, after a long incubation period, the vortex slowly intensifies to a tropical storm, which allows boundary layer pumping to form just inside or near the radius of maximum wind (e.g., the high inertial stability region). The location of the frictionally induced convergence concentrates the diabatic heating associated with the eyewall and allows the storm to transition to the rapidly intensifying or deepening phase of the life cycle.

To explore the role of an expanding wind field in eyewall replacement, we use a double Gaussian vortex in a series of experiments in section 3.5. The experiments show that as the wind field above the boundary layer expands, the radial inflow associated with the primary eyewall is slowly cut off as a secondary maximum in radial inflow develops. From these experiments, we can make two conclusions. We see that the Ekman pumping associated with the primary eyewall can shift radially outward as the vortex expands. This process could signal the end of the rapidly intensifying or deepening phase of the life cycle as the eyewall shifts outward away from the high inertial stability region. Also, the results from these experiments indicate that as the wind field continues to expand, a secondary eyewall will develop and an eyewall replacement process will commence.

This work does not take into account storm motion. In a series of papers, Chow (1971), Shapiro (1983), and Ooyama (1984) simulated the frictional boundary layer of the tropical cyclone using a two-dimensional translating slab model. In these simulations, the authors look at the boundary layer response to a vortex translating at 10 m s^{-1}. The results show a region of enhanced convergence displaced slightly to the right on the storm motion vector and strong radial inflow that abruptly stops for the spatial resolution of these simulations. Curiously, Ooyama (1984) makes a note that a "shock front" develops in regards to his results without any additional insights, explanations, or references to the

origin or reason for using such a term. In the context of the axisymmetric work presented here, the development of shock-like features in association with storm motion agrees with the notion of the shape of the gradient tangential wind profile above the boundary layer.

CHAPTER 4

CONCLUDING REMARKS

In this work, we seek to add to the understanding of the role by which inner-core and boundary layer dynamics impact the life cycle of the tropical cyclone. We examine the boundary layer and overlying vortex separately so that we can simplify the interpretation of features developing within our results and present analytic solutions to aspects of the inner-core and boundary layer dynamics. However, the results highlight the interplay and vital role of each in the life cycle of the tropical cyclone.

In chapter 2, we develop a simple, one-layer, forced, balanced model for the time evolution of the tropical cyclone. This model uses the wave–vortex approximation developed by Salmon (2014). In this work, we show that while a large fraction of the initial volume of the vortex has been removed in regions where a mass sink is present, the vortex is initially slow to intensify providing dynamical insight into why storms can have a long incubation period before rapidly intensifying. In real tropical cyclones, environmental factors, such as dry air, also contribute to the development rate by interfering with the diabatic heating or convection around the incipient vortex. Next, we show how hollow potential vorticity towers can develop without the presence of boundary layer dynamics. In these cases, a smaller mass sink is located closer to the center than the larger mass sink values. We see that inner absolute angular momentum surfaces hinder the inward movement of the outer surfaces causing the formation of vortex sheets and potential vorticity towers. These results also show absolute angular momentum surfaces sweeping through the radius of maximum wind supporting the idea that there is not a one-to-one relationship between the absolute angular momentum surfaces and the radius of maximum wind. Even if the radius of maximum wind ceases to contract, an inward movement of these surfaces accompanies vortex intensification. Then, we show the evolution of the vortex in the $\mathcal{E} - V_{\max}$ space. In this space, we see the impact of the radial distribution of the mass sink in controlling storm size and intensity during storm development and eyewall replacement. Lastly, we compare the balance relation originating from the wave–vortex approximation to gradient balance because of the small Froude number restriction resulting from the approximation made to kinetic energy to the model developed in this work. We see that for the external vertical mode, only minor deviations between the maximum tangential wind and total energy in the two models. The deviations become significantly larger for models run with phase speeds characteristic of the first three internal vertical modes. This suggests that the wave–vortex approximation is applicable to the mean vertical structure of tropical cyclones.

In chapter 3, we use a series of models to gain insight into the role of shocks originating from the embedded viscous Burgers' equation in developing primary and secondary eyewalls in the tropical cyclone. We develop a series of analytic models to understand formation time and position due to curvature and surface drag effects before looking at the role of geostrophic forcing in a line-symmetric model. From these models, we gain insight into the development of triangular waves and N-waves and the role of shock dynamics to the tropical cyclone boundary layer. Next, we develop two local, steady-state models that allow us to dissect how the nonlinear terms, especially the $u(\partial u/\partial r)$ term, impact the structure of the boundary layer given specified gradient wind profiles in the overlying layer. From these results, we see that when the inflow angle is small, typically seen in weak vortices, the local models capture the radial inflow and Ekman pumping produced by the full axisymmetric, slab boundary layer model. However, as the storm intensifies, the ratio of the magnitude of the radial profile of $u(\partial u/\partial r)$ to the absolute vorticity of the gradient flow exceeds unity, which means that the local models fail to capture the hyperbolic nature of the tropical cyclone boundary layer. In the experiments conducted here, the hyperbolic nature of the system becomes apparent once the storm intensifies to tropical storm force wind speeds. This suggests that the boundary layer becomes critical to storm organization and development shortly before the deepening stage of the life cycle. Prior to boundary layer processes helping to control the development, the evolution of the vortex intensity is likely dominated by the response to diabatic heating in the overlying vortex as shown in chapter 2. Interestingly, as the vortex tangential wind field becomes broader, it is easier to maintain unity. As the vortex continues to broaden, the radial inflow to the primary, inner eyewall is reduced. Eventually, a secondary maximum in the radial inflow and Ekman pumping develops. This shift captures the transition observed during secondary eyewall formation and replacement of the primary eyewall. Broadening of the vortex is the result of the vortex responding to diabatic heating outside of the radius of maximum wind. As shown in chapter 2, the wind field will expand even if the angular momentum surfaces are hindered from collapsing.

In closing, we note that several interesting questions arise from this work. First, how does intensification of the vortex control the formation of eye features such as eye moats, warm-ring thermal structures, etc. Some hints to the connection between the dynamic eye size or Rossby length have been explored (e.g., Schubert et al. 2007; Schubert and McNoldy 2010). The interaction between the overlying fluid and boundary layer to these features has not been explored. In regards to shock formation and the interactions between the primary and secondary eyewall, we focus on axisymmetric,

non-translating pressure fields, which result in a circular shock-like structure. However, tropical cyclones are rarely stationary. Features developing in work that has looked at translating storms allude to a critical need to understand shock dynamics in this framework (e.g., Chow 1971; Shapiro 1983; Ooyama 1984).

REFERENCES

Abarca, S. F. and M. T. Montgomery, 2013: Essential dynamics of secondary eyewall formation. *J. Atmos. Sci.*, **70**, 3216–3230, doi: 10.1175/JAS-D-12-0318.1.

Bateman, H., 1915: Some recent researches on the motion of fluids. *Mon. Wea. Rev.*, **43**, 163–170, doi: 10.1175/1520-0493(1915)43<163:SRROTM>2.0.CO;2.

Bouchut, F., J. Lambaerts, G. Lapeyre, and V. Zeitlin, 2009: Fronts and nonlinear waves in a simplified shallow-water model of the atmosphere with moisture and convection. *Phys. Fluids*, **21**, 116 604, doi: 10.1063/1.3265970.

Bryan, G. H., 2012: Effects of surface exchange coefficients and turbulence length scales on the intensity and structure of numerically simulated hurricanes. *Mon. Wea. Rev.*, **140**, 1125–1143, doi: 10.1175/MWR-D-11-00231.1.

Bryan, G. H. and R. Rotunno, 2009: The maximum intensity of tropical cyclones in axisymmetric numerical model simulations. *Mon. Wea. Rev.*, **137**, 1770–1789, doi: 10.1175/2008MWR2709.1.

Bryan, G. H., R. P. Worsnop, J. K. Lundquist, and J. A. Zhang, 2017: A simple method for simulating wind profiles in the boundary layer of tropical cyclones. *Bound.-Layer Meteor.*, **162**, 475–502, doi: 10.1007/s10546-016-0207-0.

Burgers, J. M., 1948: A mathematical model illustrating the theory of turbulence. *Adv. Appl. Mech.*, **1**, 171–199, doi: 10.1016/S0065-2156(08)70100-5.

Chan, K. T. F. and J. C. L. Chan, 2012: Size and strength of tropical cyclones from QuikSCAT data. *Mon. Wea. Rev.*, **140**, 811–824, doi: 10.1175/MWR-D-10-05062.1.

Chan, K. T. F. and J. C. L. Chan, 2014: Impacts of initial vortex size and planetary vorticity on tropical cyclone size. *Quart. J. Roy. Meteor. Soc.*, **140**, 2235–2248, doi: 10.1002/qj.2292.

Chan, K. T. F. and J. C. L. Chan, 2015: Impacts of vortex intensity and outer winds on tropical cyclone size. *Quart. J. Roy. Meteor. Soc.*, **141**, 525–537, doi: 10.1002/qj.2374.

Chow, S. H., 1971: A study of the wind field in the planetary boundary layer of a moving tropical cyclone. M.S. thesis, Dept. of Meteorology and Oceanography, New York University, 59 pp.

Davis, C. A., 2015: The formation of moist vortices and tropical cyclones in idealized simulations. *J. Atmos. Sci.*, **72**, 3499–3516, doi: 10.1175/JAS-D-15-0027.1.

Deardorff, J. W., 1968: Dependence of air-sea transfer coefficients on bulk stability. *J. Geophys. Res.*, **73**, 2549–2557, doi: 10.1029/JB073i008p02549.

DeMaria, M., 1996: The effect of vertical shear on tropical cyclone intensity change. *J. Atmos. Sci.*, **53**, 2076–2087, doi: 10.1175/1520-0469(1996)053<2076:TEOVSO>2.0.CO;2.

DeMaria, M. and J. Kaplan, 1994: A Statistical Hurricane Intensity Prediction Scheme (SHIPS) for the Atlantic basin. *Wea. Forecasting*, **9**, 209–220, doi: 10.1175/1520-0434(1994)009<0209:ASHIPS>2.0.CO;2.

DeMaria, M., M. Mainelli, L. K. Shay, J. A. Knaff, and J. Kaplan, 2005: Further improvements to the Statistical Hurricane Intensity Prediction Scheme (SHIPS). *Wea. Forecasting*, **20**, 531–543, doi: 10.1175/WAF862.1.

DeMaria, M. and J. D. Pickle, 1988: A simplified system of equations for simulation of tropical cyclones. *J. Atmos. Sci.*, **45**, 1542–1554, doi: 10.1175/1520-0469(1988)045<1542:ASSOEF>2.0.CO;2.

Didlake, A. C., Jr. and R. A. Houze, Jr., 2011: Kinematics of the secondary eyewall observed in Hurricane Rita (2005). *J. Atmos. Sci.*, **68**, 1620–1636, doi: 10.1175/2011JAS3715.1.

Donelan, M. A., B. K. Haus, N. Reul, W. J. Plant, M. Stiassnie, H. C. Graber, O. B. Brown, and E. S. Saltzman, 2004: On the limiting aerodynamic roughness of the ocean in very strong winds. *Geophys. Res. Lett.*, **31**, L18 306, doi: 10.1029/2004GL019460.

Ekman, V. W., 1905: On the influence of the Earth's rotation on ocean-currents. *Arch. Math. Astron. Phys.*, **2**, 1–52.

Eliassen, A., 1951: Slow thermally or frictionally controlled meridional circulation in a circular vortex. *Astrophys. Norv.*, **5**, 19–60.

Eliassen, A., 1971: On the Ekman layer in a circular vortex. *J. Meteor. Soc. Japan*, **49**, 784–789, doi: 10.2151/jmsj1965.49A.0_784.

Eliassen, A. and M. Lystad, 1977: The Ekman layer of a circular vortex. A numerical and theoretical study. *Geophys. Norv.*, **7**, 1–16.

Emanuel, K. A., 1986: An air-sea interaction theory for tropical cyclones. Part I: Steady-state maintenance. *J. Atmos. Sci.*, **43**, 585–604, doi: 10.1175/1520-0469(1986)043<0585:AASITF>2.0.CO;2.

Emanuel, K. A., 1997: Some aspects of hurricane inner-core dynamics and energetics. *J. Atmos. Sci.*, **54**, 1014–1026, doi: 10.1175/1520-0469(1997)054<1014:SAOHIC>2.0.CO;2.

Frank, W. M. and E. A. Ritchie, 2001: Effects of vertical wind shear on the intensity and structure of numerically simulated hurricanes. *Mon. Wea. Rev.*, **129**, 2249–2269, doi: 10.1175/1520-0493(2001)129<2249:EOVWSO>2.0.CO;2.

Frisius, T. and M. Lee, 2016: The impact of gradient wind imbalance on tropical cyclone intensification within Ooyama's three-layer model. *J. Atmos. Sci.*, **73**, 3659–3679, doi: 10.1175/JAS-D-15-0336.1.

Fulton, S. R. and W. H. Schubert, 1985: Vertical normal mode transforms: Theory and application. *Mon. Wea. Rev.*, **113**, 647–658, doi: 10.1175/1520-0493(1985)113<0647:VNMTTA>2.0.CO;2.

Gray, W. M., 1968: Global view of the origin of tropical disturbances and storms. *Mon. Wea. Rev.*, **96**, 669–700, doi: 10.1175/1520-0493(1968)096<0669:GVOTOO>2.0.CO;2.

Gray, W. M., 1981: *Recent advances in tropical cyclone research from rawinsonde composite analysis*. World Meteorological Organization, 407 pp.

Harper, B. A., J. D. Kepert, and J. D. Ginger, 2010: Guidelines for converting between various wind averaging periods in tropical cyclone conditions. World Meteorological Organization Tech. Doc. WMO/TD-1555, 54 pp. [Available from World Meteorological Organization online at https://www.wmo.int/pages/prog/www/tcp/documents/WMO_TD_1555_en.pdf.].

Haurwitz, B., 1935: On the change of the wind with elevation under the influence of viscosity in curved air currents. *Gerlands Beitr. Geophys.*, **45**, 243–267.

Haurwitz, B., 1936: Supplementary to: On the change of the wind with elevation under the influence of viscosity in curved air currents. *Gerlands Beitr. Geophys.*, **47**, 203–205.

Hawkins, H. F. and D. T. Rubsam, 1968: Hurricane Hilda 1964. Part II: Structure and budget of the hurricane core on 1 October 1964. *Mon. Wea. Rev.*, **96**, 617–636, doi: 10.1175/1520-0493(1968)096<0617:HH>2.0.CO;2.

Hill, K. A. and G. M. Lackmann, 2009: Influence of environmental humidity on tropical cyclone size. *Mon. Wea. Rev.*, **137**, 3294–3315, doi: 10.1175/2009MWR2679.1.

Holland, G. J., 1997: The maximum potential intensity of tropical cyclones. *J. Atmos. Sci.*, **54**, 2519–2541, doi: 10.1175/1520-0469(1997)054<2519:TMPIOT>2.0.CO;2.

Jones, S. C., 1995: The evolution of vortices in vertical shear. I: Initially barotropic vortices. *Quart. J. Roy. Meteor. Soc.*, **121**, 821–851, doi: 10.1002/qj.49712152406.

Kepert, J. D., 2001: The dynamics of boundary layer jets within the tropical cyclone core. Part I: Linear theory. *J. Atmos. Sci.*, **58**, 2469–2484, doi: 10.1175/1520-0469(2001)058<2469:TDOBLJ>2.0.CO;2.

Kepert, J. D., 2010a: Slab- and height-resolving models of the tropical cyclone boundary layer. Part I: Comparing the simulations. *Quart. J. Roy. Meteor. Soc.*, **136**, 1686–1699, doi: 10.1002/qj.667.

Kepert, J. D., 2010b: Slab- and height-resolving models of the tropical cyclone boundary layer. Part II: Why the simulations differ. *Quart. J. Roy. Meteor. Soc.*, **136**, 1700–1711, doi: 10.1002/qj.685.

Kepert, J. D., 2013: How does the boundary layer contribute to eyewall replacement cycles in axisymmetric tropical cyclones? *J. Atmos. Sci.*, **70**, 2808–2830, doi: 10.1175/JAS-D-13-046.1.

Kepert, J. D., 2017: Time and space scales in the tropical cyclone boundary layer, and the location of the eyewall updraft. *J. Atmos. Sci.*, **74**, 3305–3323, doi: 10.1175/JAS-D-17-0077.1.

Kepert, J. D. and D. S. Nolan, 2014: Reply to "Comments on 'How does the boundary layer contribute to eyewall replacement cycles in axisymmetric tropical cyclones?' ". *J. Atmos. Sci.*, **71**, 4692–4704, doi: 10.1175/JAS-D-14-0014.1.

Kepert, J. D. and Y. Wang, 2001: The dynamics of boundary layer jets within the tropical cyclone core. Part II: Nonlinear enhancement. *J. Atmos. Sci.*, **58**, 2485–2501, doi: 10.1175/1520-0469(2001)058<2485:TDOBLJ>2.0.CO;2.

Kimball, S. K. and M. S. Mulekar, 2004: A 15-year climatology of North Atlantic tropical cyclones. Part I: Size parameters. *J. Climate*, **17**, 3555–3575, doi: 10.1175/1520-0442(2004)017<3555:AYCONA>2.0.CO;2.

Kleinschmidt, E., Jr., 1951: Grundlagem einer theorie der tropischen zyklonen. *Arch. Met. Geophys. Bioklimatol.*, **4a**, 57–72.

Knaff, J. A., S. P. Longmore, and D. A. Molenar, 2014: An objective satellite-based tropical cyclone size climatology. *J. Climate*, **27**, 455–476, doi: 10.1175/JCLI-D-13-00096.1.

Knaff, J. A., C. R. Sampson, M. DeMaria, T. P. Marchok, J. M. Gross, and C. J. McAdie, 2007: Statistical tropical cyclone wind radii prediction using climatology and persistence. *Wea. Forecasting*, **22**, 781–791, doi: 10.1175/WAF1026.1.

Kuo, A. C. and L. M. Polvani, 1997: Time-dependent fully nonlinear geostrophic adjustment. *J. Phys. Oceanogr.*, **27**, 1614–1634, doi: 10.1175/1520-0485(1997)027<1614:TDFNGA>2.0.CO;2.

La Seur, N. E. and H. F. Hawkins, 1963: An analysis of Hurricane Cleo (1958) based on data from research reconnaissance aircraft. *Mon. Wea. Rev.*, **91**, 694–709, doi: 10.1175/1520-0493(1963)091<0694:AAOHCB>2.3.CO;2.

Lambaerts, J., G. Lapeyre, V. Zeitlin, and F. Bouchut, 2011: Simplified two-layer models of precipitating atmosphere and their properties. *Phys. Fluids*, **23**, 046 603, doi: 10.1063/1.3582356.

Large, W. G., J. C. McWilliams, and S. C. Doney, 1994: Oceanic vertical mixing: A review and a model with a nonlocal boundary layer parameterization. *Rev. Geophys.*, **32**, 363–403, doi: 10.1029/94RG01872.

Large, W. G. and S. Pond, 1982: Sensible and latent heat flux measurements over the ocean. *J. Phys. Oceanogr.*, **12**, 464–482, doi: 10.1175/1520-0485(1982)012<0464:SALHFM>2.0.CO;2.

LeVeque, R. J., 1992: *Numerical methods for conservation laws*. Birkhäuser, 228 pp.

Lighthill, M. J., 1956: Viscosity effects in sound waves of finite amplitude. *Surveys in Mechanics*, G. K. Batchelor and R. M. Davies, Eds., Cambridge Univ. Press, 250–351.

Liu, K. S. and J. C. L. Chan, 1999: Size of tropical cyclones as inferred from ERS-1 and ERS-2 data. *Mon. Wea. Rev.*, **127**, 2992–3001, doi: 10.1175/1520-0493(1999)127<2992:SOTCAI>2.0.CO;2.

Maclay, K. S., M. DeMaria, and T. H. Vonder Haar, 2008: Tropical cyclone inner-core kinetic energy evolution. *Mon. Wea. Rev.*, **136**, 4882–4898, doi: 10.1175/2008MWR2268.1.

Merrill, R. T., 1984: A comparison of large and small tropical cyclones. *Mon. Wea. Rev.*, **112**, 1408–1418, doi: 10.1175/1520-0493(1984)112<1408:ACOLAS>2.0.CO;2.

Miller, B. I., 1958: On the maximum intensity of hurricanes. *J. Meteor.*, **15**, 184–195, doi: 10.1175/1520-0469(1958)015<0184:OTMIOH>2.0.CO;2.

Montgomery, M. T., S. F. Abarca, R. K. Smith, C.-C. Wu, and Y.-H. Huang, 2014: Comments on "How does the boundary layer contribute to eyewall replacement cycles in axisymmetric tropical cyclones?". *J. Atmos. Sci.*, **71**, 4682–4691, doi: 10.1175/JAS-D-13-0286.1.

Montgomery, M. T. and R. K. Smith, 2014: Paradigms for tropical cyclone intensification. *Aust. Meteor. Oceanogr. J.*, **64**, 37–66, doi: 10.22499/2.6402.005.

Montgomery, M. T. and R. K. Smith, 2017: Recent developments in the fluid dynamics of tropical cyclones. *Annu. Rev. Fluid Mech.*, **49**, 541–574, doi: 10.1146/annurev-fluid-010816-060022.

Moon, Y. and D. S. Nolan, 2010: The dynamic response of the hurricane wind field to spiral rainband heating. *J. Atmos. Sci.*, **67**, 1779–1805, doi: 10.1175/2010JAS3171.1.

Musgrave, K. D., R. K. Taft, J. L. Vigh, B. D. McNoldy, and W. H. Schubert, 2012: Time evolution of the intensity and size of tropical cyclones. *J. Adv. Model. Earth Syst.*, **4**, M08 001, doi: 10.1029/2011MS000104.

Ooyama, K., 1969a: Numerical simulation of the life cycle of tropical cyclones. *J. Atmos. Sci.*, **26**, 3–40, doi: 10.1175/1520-0469(1969)026<0003:NSOTLC>2.0.CO;2.

Ooyama, K., 1969b: Numerical simulation of tropical cyclones with an axi-symmetric model. *Proc. Third Symposium on Numerical Weather Prediction*, Tokyo, WMO/IUGG, 81–88.

Ooyama, K., 1982: Conceptual evolution of the theory and modeling of the tropical cyclone. *J. Meteor. Soc. Japan*, **60**, 369–380, doi: 10.2151/jmsj1965.60.1_369.

Ooyama, K., 1984: A model for hurricane prediction. *Proc. 15th Technical Conference on Hurricanes and Tropical Meteorology*, Miami, AMS, 344–349.

Platzman, G. W., 1985: Conversations with Bernhard Haurwitz. NCAR Tech. Note NCAR/TN-257+PROC, 184 pp., Boulder, CO. doi: 10.5065/D6862DDK, [Available from NCAR online at https://opensky.ucar.edu/islandora/object/technotes%3A367.].

Powell, M. D. and T. A. Reinhold, 2007: Tropical cyclone destructive potential by integrated kinetic energy. *Bull. Amer. Meteor. Soc.*, **88**, 513–526, doi: 10.1175/BAMS-88-4-513.

Powell, M. D., E. W. Uhlhorn, and J. D. Kepert, 2009: Estimating maximum surface winds from hurricane reconnaissance measurements. *Wea. Forecasting*, **24**, 868–883, doi: 10.1175/2008WAF2007087.1.

Powell, M. D., P. J. Vickery, and T. A. Reinhold, 2003: Reduced drag coefficient for high wind speeds in tropical cyclones. *Nature*, **422**, 279–283, doi: 10.1038/nature01481.

Raymond, D. J. and M. J. Herman, 2012: Frictional convergence, atmospheric convection, and causality. *Atmósfera*, **25**, 253–267.

Rogers, R. F., P. D. Reasor, and S. Lorsolo, 2013: Airborne Doppler observations of the inner-core structural differences between intensifying and steady-state tropical cyclones. *Mon. Wea. Rev.*, **141**, 2970–2991, doi: 10.1175/MWR-D-12-00357.1.

Rogers, R. F., P. D. Reasor, and J. A. Zhang, 2015: Multiscale structure and evolution of Hurricane Earl (2010) during rapid intensification. *Mon. Wea. Rev.*, **143**, 536–562, doi: 10.1175/MWR-D-14-00175.1.

Rosenthal, S. L., 1970: A circularly symmetric primitive equation model of tropical cyclone development containing an explicit water vapor cycle. *Mon. Wea. Rev.*, **98**, 643–663, doi: 10.1175/1520-0493(1970)098<0643:ACSPEM>2.3.CO;2.

Rosenthal, S. L., 1971: The response of a tropical cyclone model to variations in boundary layer parameters, initial conditions, lateral boundary conditions, and domain size. *Mon. Wea. Rev.*, **99**, 767–777, doi: 10.1175/1520-0493(1971)099<0767:TROATC>2.3.CO;2.

Rozoff, C. M., D. S. Nolan, J. P. Kossin, F. Zhang, and J. Fang, 2012: The roles of an expanding wind field and inertial stability in tropical cyclone secondary eyewall formation. *J. Atmos. Sci.*, **69**, 2621–2643, doi: 10.1175/JAS-D-11-0326.1.

Salmon, R., 1983: Practical use of Hamilton's principle. *J. Fluid Mech.*, **132**, 431–444, doi: 10.1017/S0022112083001706.

Salmon, R., 1988: Hamiltonian fluid mechanics. *Annu. Rev. Fluid Mech.*, **20**, 225–256, doi: 10.1146/annurev.fl.20.010188.001301.

Salmon, R., 1998: *Lectures on geophysical fluid dynamics*. Oxford Univ. Press, 378 pp.

Salmon, R., 2014: Analogous formulation of electrodynamics and two-dimensional fluid dynamics. *J. Fluid Mech.*, **761**, R2, doi: 10.1017/jfm.2014.642.

Schubert, W. H. and J. J. Hack, 1982: Inertial stability and tropical cyclone development. *J. Atmos. Sci.*, **39**, 1687–1697, doi: 10.1175/1520-0469(1982)039<1687:ISATCD>2.0.CO;2.

Schubert, W. H. and J. J. Hack, 1983: Transformed Eliassen balanced vortex model. *J. Atmos. Sci.*, **40**, 1571–1583, doi: 10.1175/1520-0469(1983)040<1571:TEBVM>2.0.CO;2.

Schubert, W. H., J. J. Hack, P. L. Silva Dias, and S. R. Fulton, 1980: Geostrophic adjustment in an axisymmetric vortex. *J. Atmos. Sci.*, **37**, 1464–1484, doi: 10.1175/1520-0469(1980)037<1464:GAIAAV>2.0.CO;2.

Schubert, W. H. and B. D. McNoldy, 2010: Application of the concepts of Rossby length and Rossby depth to tropical cyclone dynamics. *J. Adv. Model. Earth Syst.*, **2**, 13 pp, doi: 10.3894/JAMES.2010.2.7.

Schubert, W. H., M. T. Montgomery, R. K. Taft, T. A. Guinn, S. R. Fulton, J. P. Kossin, and J. P. Edwards, 1999: Polygonal eyewalls, asymmetric eye contraction, and potential vorticity mixing in hurricanes. *J. Atmos. Sci.*, **56**, 1197–1223, doi: 10.1175/1520-0469(1999)056<1197:PEAECA>2.0.CO;2.

Schubert, W. H., C. M. Rozoff, J. L. Vigh, B. D. McNoldy, and J. P. Kossin, 2007: On the distribution of subsidence in the hurricane eye. *Quart. J. Roy. Meteor. Soc.*, **133**, 595–605, doi: 10.1002/qj.49.

Schubert, W. H., C. J. Slocum, and R. K. Taft, 2016: Forced, balanced model of tropical cyclone intensification. *J. Meteor. Soc. Japan*, **94**, 119–135, doi: 10.2151/jmsj.2016-007.

Schubert, W. H., C. J. Slocum, and R. K. Taft, 2017: Basic concepts involved in tropical cyclone boundary layer shocks. [Available online at http://arxiv.org/abs/1709.00101.], 29 pp.

Shapiro, L. J., 1983: The asymmetric boundary layer flow under a translating hurricane. *J. Atmos. Sci.*, **40**, 1984–1998, doi: 10.1175/1520-0469(1983)040<1984:TABLFU>2.0.CO;2.

Shapiro, L. J. and H. E. Willoughby, 1982: The response of balanced hurricanes to local sources of heat and momentum. *J. Atmos. Sci.*, **39**, 378–394, doi: 10.1175/1520-0469(1982)039<0378:TROBHT>2.0.CO;2.

Shepard, T. G., 1990: Symmetries, conservation laws, and Hamiltonian structure in geophysical fluid dynamics. *Adv. Geophys.*, **32**, 287–338, doi: 10.1016/S0065-2687(08)60429-X.

Sitkowski, M., J. P. Kossin, and C. M. Rozoff, 2011: Intensity and structure changes during hurricane eyewall replacement cycles. *Mon. Wea. Rev.*, **139**, 3829–3847, doi: 10.1175/MWR-D-11-00034.1.

Sitkowski, M., J. P. Kossin, C. M. Rozoff, and J. A. Knaff, 2012: Hurricane eyewall replacement cycle thermodynamics and the relict inner eyewall circulation. *Mon. Wea. Rev.*, **140**, 4035–4045, doi: 10.1175/MWR-D-11-00349.1.

Slocum, C. J., 2013: Diabatic and frictional forcing effects on the structure and intensity of tropical cyclones. M.S. thesis, Dept. of Atmos. Sci., Colorado State University, 77 pp.

Slocum, C. J., G. J. Williams, R. K. Taft, and W. H. Schubert, 2014: Tropical cyclone boundary layer shocks. [Available online at http://arxiv.org/abs/1405.7939.], 19 pp.

Smith, R. K., 1968: The surface boundary layer of a hurricane. *Tellus*, **20**, 473–483, doi: 10.324/tellusa.v20i3.10026.

Smith, R. K., 2003: A simple model of the hurricane boundary layer. *Quart. J. Roy. Meteor. Soc.*, **129**, 1007–1027, doi: 10.1256/qj.01.197.

Smith, R. K. and M. T. Montgomery, 2015: Towards clarity on understanding tropical cyclone intensification. *J. Atmos. Sci.*, **72**, 3020–3031, doi: 10.1175/JAS-D-15-0017.1.

Smith, R. K. and S. Vogl, 2008: A simple model of the hurricane boundary layer revisited. *Quart. J. Roy. Meteor. Soc.*, **134**, 337–351, doi: 10.1002/qj.216.

Stern, D. P. and D. S. Nolan, 2012: On the height of the warm core in tropical cyclones. *J. Atmos. Sci.*, **69**, 1657–1680, doi: 10.1175/JAS-D-11-010.1.

Stern, D. P., J. L. Vigh, D. S. Nolan, and F. Zhang, 2015: Revisiting the relationship between eyewall contraction and intensification. *J. Atmos. Sci.*, **72**, 1283–1306, doi: 10.1175/JAS-D-14-0261.1.

Stern, D. P. and F. Zhang, 2013: How does the eye warm? Part I: A potential temperature budget analysis of an idealized tropical cyclone. *J. Atmos. Sci.*, **70**, 73–90, doi: 10.1175/JAS-D-11-0329.1.

Vigh, J. P. and W. H. Schubert, 2009: Rapid development of the tropical cyclone warm core. *J. Atmos. Sci.*, **66**, 3335–3350, doi: 10.1175/2009JAS3092.1.

Vogl, S. and R. K. Smith, 2009: Limitations of a linear model for the hurricane boundary layer. *Quart. J. Roy. Meteor. Soc.*, **135**, 839–850, doi: 10.1002/qj.390.

Von Neumann, J. and R. D. Richtmyer, 1950: A method for the numerical calculation of hydrodynamic shocks. *J. Appl. Phys.*, **21**, 232–237, doi: 10.1063/1.1699639.

Wang, Y., 2009: How do outer spiral rainbands affect tropical cyclone structure and intensity? *J. Atmos. Sci.*, **66**, 1250–1273, doi: 10.1175/2008JAS2737.1.

Whitham, G. B., 1974: *Linear and nonlinear wave*. Wiley, 636 pp.

Williams, G. J., R. K. Taft, B. D. McNoldy, and W. H. Schubert, 2013: Shock-like structures in the tropical cyclone boundary layer. *J. Adv. Model. Earth Syst.*, **5**, 338–353, doi: 10.1002/jame.20028.

Willoughby, H. E., 1990: Gradient balance in tropical cyclones. *J. Atmos. Sci.*, **47**, 265–274, doi: 10.1175/1520-0469(1990)047<0265:GBITC>2.0.CO;2.

Wing, A. A., S. J. Camargo, and A. H. Sobel, 2016: Role of radiative–convective feedbacks in spontaneous tropical cyclogenesis in idealized numerical simulations. *J. Atmos. Sci.*, **73**, 2633–2642, doi: 10.1175/JAS-D-15-0380.1.

Yamasaki, M., 1977: The role of surface friction in tropical cyclones. *J. Meteor. Soc. Japan*, **55**, 559–572, doi: 10.2151/jmsj1965.55.6_559.

Yamasaki, M., 1983: A further study of tropical cyclones without parameterizing the effects of cumulus convection. *Pap. Meteor. Geophys.*, **34**, 221–260, doi: 10.2467/mripapers.34.221.

APPENDIX

HAMILTONIAN FORM OF THE SHALLOW WATER DYNAMICS[5]

In the following appendix, we will derive the wave–vortex approximation to the axisymmetric, shallow water dynamics in the Hamiltonian form by following the procedure outlined by Salmon (2014) and Schubert et al. (2016). Hamiltonian fluid mechanics is succinct and preserves conservation laws allowing for analytical approximations to the equations of motion. For a review, Salmon (1983), Salmon (1988), Shepard (1990), and Salmon (1998) discuss Hamiltonian mechanics (i.e., classical mechanics) and its uses in fluid dynamics in greater detail.

Consider the axisymmetric, shallow water dynamics expressed in the Hamiltonian form

$$\frac{dF}{dt} = \{F, H\}, \tag{A1}$$

where $F[u, v, h]$ is an arbitrary functional of $u(r,t)$, $v(r,t)$, and $h(r,t)$ and the Poisson bracket of any two functionals $A[u, v, h]$ and $B[u, v, h]$ is defined by

$$\{A, B\} = \int_0^\infty \left[\left(\frac{f+\zeta}{h}\right)\left(\frac{\delta A}{\delta u}\frac{\delta B}{\delta v} - \frac{\delta B}{\delta u}\frac{\delta A}{\delta v}\right) - \frac{\delta A}{\delta u}\frac{\partial}{\partial r}\left(\frac{\delta B}{\delta h}\right) + \frac{\delta B}{\delta u}\frac{\partial}{\partial r}\left(\frac{\delta A}{\delta h}\right)\right] r\, dr. \tag{A2}$$

The Hamiltonian functional $H[u, v, h]$ for the axisymmetric, shallow water primitive equations is

$$H = \int_0^\infty \left[\frac{1}{2}(u^2 + v^2)h + \frac{1}{2}g(h - \bar{h})^2\right] r\, dr, \tag{A3}$$

and the functional derivatives of this Hamiltonian are

$$\frac{\delta H}{\delta u} = h\, u, \tag{A4}$$

$$\frac{\delta H}{\delta v} = h\, v, \tag{A5}$$

$$\frac{\delta H}{\delta h} = g(h - \bar{h}) + \frac{1}{2}(u^2 + v^2). \tag{A6}$$

[5]This appendix is reproduced from Schubert et al. (2016) to show how wave–vortex theory is derived using Hamilton's principle.

Using (A1), (A2), and (A4)–(A6), we express the axisymmetric, shallow water dynamics as

$$\frac{dF}{dt} = \int_0^\infty \left[\frac{\delta F}{\delta u} \left((f+\zeta)v - \frac{\partial \left[gh + \frac{1}{2}(u^2+v^2) \right]}{\partial r} \right) - \frac{\delta F}{\delta v}(f+\zeta)u - \frac{\delta F}{\delta h} \frac{\partial (ruh)}{r\,\partial r} \right] r\,dr, \tag{A7}$$

where we have performed an integration by parts to obtain the last term in the integrand.

A1 Radial momentum equation

For the radial momentum equation, we choose the arbitrary functional F to be

$$F[u] = \int_0^\infty \delta(r-\hat{r})\,u(r,t) r\,dt = u(\hat{r},t), \tag{A8}$$

where the Dirac delta function $\delta(r-\hat{r})$ vanishes for $r \neq \hat{r}$ and satisfies $\int \delta(r-\hat{r}) r\,dr = 1$. Then,

$$\frac{\delta F}{\delta u} = \delta(r-\hat{r}), \tag{A9}$$

$$\frac{\delta F}{\delta v} = 0, \text{ and} \tag{A10}$$

$$\frac{\delta F}{\delta h} = 0, \tag{A11}$$

so that (A7) yields

$$\frac{du(\hat{r},t)}{dt} = \left((f+\zeta)v - \frac{\partial \left[gh + \frac{1}{2}(u^2+v^2) \right]}{\partial r} \right)_{r=\hat{r}}, \tag{A12}$$

which can be expressed in the advective form of the radial momentum equation (2.1).

A2 Tangential momentum equation

For the tangential momentum equation, we choose the arbitrary function F to be

$$F[v] = \int_0^\infty \delta(r-\hat{r})\,v(r,t) r\,dr = v(\hat{r},t), \tag{A13}$$

so that

$$\frac{\delta F}{\delta u} = 0, \tag{A14}$$

$$\frac{\delta F}{\delta v} = \delta(r-\hat{r}), \text{ and} \tag{A15}$$

$$\frac{\delta F}{\delta h} = 0. \tag{A16}$$

Then, (A1) and (A7) yield

$$\frac{d\,v(\hat{r},t)}{d\,t} = -\big((f+\zeta)u\big)_{r=\hat{r}}\,, \tag{A17}$$

which can also be expressed in the advective form of the tangential momentum equation (2.2).

A3 Continuity equation

For the mass continuity equation, we choose the arbitrary functional F to be

$$F[h] = \int_0^\infty \delta(r-\hat{r})\,h(r,t)r\,d\,r = h(\hat{r},t), \tag{A18}$$

so that

$$\frac{\delta F}{\delta u} = 0, \tag{A19}$$

$$\frac{\delta F}{\delta v} = 0, \text{ and} \tag{A20}$$

$$\frac{\delta F}{\delta h} = \delta(r-\hat{r}). \tag{A21}$$

Then, (A1) and (A7) yield

$$\frac{d\,h(\hat{r},t)}{d\,t} = -\left(\frac{\partial(r\,u\,h)}{r\,\partial\,r}\right)_{r=\hat{r}}, \tag{A22}$$

which can also be expressed in the advective form of the continuity equation (2.3).

A4 Total energy conservation relation

We note that the choice $F[u,v,h] = H[u,v,h]$ leads to $\{F,H\} = \{H,H\} = 0$ through use of the Poisson bracket (A2), so that (A1) becomes the total energy conservation relation

$$\frac{d\,H}{d\,t} = 0. \tag{A23}$$

A5 The wave–vortex approximation

For the balanced relation proposed by Salmon (2014), the Hamiltonian form of the dynamics is expressed as

$$\frac{d\,F}{d\,t} = \{F, H_{\rm wv}\}\,, \tag{A24}$$

where the definition of the Poisson bracket is unchanged, but the Hamiltonian function (A3) is approximated by

$$H_{\rm wv} = \int_0^\infty \left[\frac{1}{2}(u^2+v^2)\bar{h} + \frac{1}{2}g(h-\bar{h})^2\right] r\,d\,r. \tag{A25}$$

The functional derivatives of the Hamiltonian for the wave–vortex model are

$$\frac{\delta H_{\rm wv}}{\delta u} = \bar{h}\, u, \tag{A26}$$

$$\frac{\delta H_{\rm wv}}{\delta \upsilon} = \bar{h}\, \upsilon, \tag{A27}$$

$$\frac{\delta H_{\rm wv}}{\delta h} = g(h-\bar{h}). \tag{A28}$$

Comparing (A4)–(A6) to (A26)–(A28) indicates that the influence of the replacement of h by $\bar{h}$ in the kinetic energy part of (A25) has spread into all three functional derivatives. Using (A24), (A2), and (A26)–(A28), we can express the axisymmetric, wave–vortex dynamics as

$$\frac{dF}{dt} = \int_0^\infty \left[\frac{\delta F}{\delta u}\left(P\upsilon - g\frac{\partial h}{\partial r}\right) - \frac{\delta F}{\delta \upsilon} P u - \frac{\delta F}{\delta h}\frac{\partial (r u \bar{h})}{r\,\partial r}\right] r\, dr, \tag{A29}$$

where

$$P = \frac{\bar{h}}{h}\left(f + \frac{\partial (r\upsilon)}{r\,\partial r}\right).$$

A6 Equations from the wave–vortex approximation

To obtain the wave–vortex balance relation approximation of the radial momentum equation, the tangential momentum equation, and the continuity equation, we sequentially choose the arbitrary functional F to be that given in (A8), (A13), and (A18). Then, following the previous arguments, we find that (A29) yields

$$\frac{du(\hat{r},t)}{dt} = \left(P\upsilon - g\frac{\partial h}{\partial r}\right)_{r=\hat{r}}, \tag{A30}$$

$$\frac{d\upsilon(\hat{r},t)}{dt} = -(Pu)_{r=\hat{r}}, \tag{A31}$$

$$\frac{dh(\hat{r},t)}{dt} = -\left(\frac{\partial (r u \bar{h})}{r\,\partial r}\right)_{r=\hat{r}}. \tag{A32}$$

These last three equations can also be expressed in advective form (2.10)–(2.12). Finally, to obtain the total energy conservation relation for wave–vortex theory, note that the choice $F[u,\upsilon,h] = H_{\rm wv}[u,\upsilon,h]$ leads to $\{F, H_{\rm wv}\} = \{H_{\rm wv}, H_{\rm wv}\} = 0$ through use of the Poisson bracket (A2), so that (A24) becomes

$$\frac{dH_{\rm wv}}{dt} = 0. \tag{A33}$$